2010-11-10T14:16:10Z

Investigation of bubble dynamics and heating during focused ultrasound insonation in tissue-mimicking materials

https://hdl.handle.net/2144/1368

Boston University

BOSTON UNIVERSITY

COLLEGE OF ENGINEERING

Dissertation

INVESTIGATION OF BUBBLE DYNAMICS AND

HEATING DURING FOCUSED ULTRASOUND

INSONATION IN TISSUE-MIMICKING MATERIALS

by

XINMAI YANG

B.S., Xi'an Jiaotong University, China, 1997
M.S., Xi'an Jiaotong University, China, 2000

Submitted in partial fulfillment of the

requirements for the degree of

Doctor of Philosophy

2003

Acknowledgements

I owe a debt of gratitude to my mentors, fellow graduate students and friends. I cannot imagine how I could earn this degree without their help. I take this opportunity to thank my major advisor, Professor R. Glynn Holt, for his guidance and support all these years. He has constantly inspired me with his knowledge and love of bubbles. I also want to thank Professor Ronald A. Roy for his support throughout this project, as well as the insightful comments on my research. Great gratitude should also go to Professor Robin O Cleveland, with whom I worked in the first few months in Boston and keep getting help from him during this tenure. Special thanks should be given to Dr. Charlie Church, for his patience in reading my dissertation and making detailed comments, including all the grammar mistakes I made. Professor Hynynen is also to be thanked for his kindness and valuable comments on my dissertation.

I also would like to thank Professor Bill Carey for all his help, including helping me on my research and teaching me about real American life. Dr. Jinlan Huang is acknowledged for her kind help on this project. Dr. Preston Wilson is always to be found as a reliable source of help in the lab and should be given special thanks. I also want to thank Dr. Constantin Coussios for his support on my trip to the 145th ASA meeting.

I would like to thank my fellow graduate students for their help and support: Charles Thomas, Eun-Joo Park, Yuan Jing, Lei Sui, Li Liu, Yan Zhang, Parag Chitnis, Paolo Zanetti, Caleb Farny, Javier Van Cauwelaert, Jed Wilbur and everyone I've unintentionally left out, for illuminating talks and being my friends in the past years. Special thanks to Charles Thomas, for

INVESTIGATION OF BUBBLE DYNAMICS AND HEATING DURING FOCUSED ULTRASOUND INSONATION IN TISSUE- MIMICKING MATERIALS

(Order No.   )

XINMAI YANG

Boston University, College of Engineering, 2003
Major Professor: R. Glynn Holt, Assistant Professor of AME

Abstract

The deposition of ultrasonic energy in tissue can cause tissue damage due to local heating. For pressures above a critical threshold, cavitation will occur in tissue and bubbles will be created. These oscillating bubbles can induce a much larger thermal energy deposition in the local region. Traditionally, clinicians and researchers have not exploited this bubble-enhanced heating since cavitation behavior is erratic and very difficult to control.

The present work is an attempt to control and utilize this bubble-enhanced heating. First, by applying appropriate bubble dynamic models, limits on the asymptotic bubble size distribution are obtained for different driving pressures at 1 MHz. The size distributions are bounded by two thresholds: the bubble shape instability threshold and the rectified diffusion threshold. The growth rate of bubbles in this region is also given, and the resulting time evolution of the heating in a given insonation scenario is modeled. In addition, some experimental results have been obtained to investigate the bubble-enhanced heating in an agar and graphite based tissue-mimicking material. Heating as a function of dissolved gas concentrations in the tissue phantom is investigated. Bubble-based contrast agents are introduced to investigate the effect on the bubble-enhanced heating, and to control the initial bubble size distribution.

The mechanisms of cavitation-related bubble heating are investigated, and a heating model is established using our understanding of the bubble dynamics. By fitting appropriate bubble densities in the ultrasound field, the peak temperature changes are simulated. The results for required bubble density are given. Finally, a simple bubbly liquid model is presented to estimate the shielding effects which may be important even for low void fraction during high intensity focused ultrasound (HIFU) treatment.

Contents

List of Tables

List of Figures

Chapter 1

Introduction

1.1 Background and motivation

Sound is a wave phenomenon. In the present usage, the term "sound" implies not only the phenomena in air responsible for the sensation of hearing, but also whatever else is governed by analogous physical principles [1]. Sound which can be heard by the human ear has a frequency of about 5-20000 Hz. Neither higher nor lower frequency sound can be heard by our ears. Propagating pressure vibrations are called infrasound when the sound frequency is lower than 5 Hz and ultrasound when the frequency is higher than 20000 Hz. Ultrasound has several unique advantages in modern medicine, such as low cost, noninvasive, etc. Ultrasound diagnosis and therapy are two of the critical applications for scientists in this area. Ultrasound diagnosis involves imaging techniques, including traditional fundamental frequency imaging and Doppler imaging, as well as novel imaging techniques in development, such as subharmonic and higher harmonic imaging. In some complex situations, micro-bubble based contrast agents may be used to get clear images [2]. Compared to the routinely used ultrasound imaging techniques, ultrasound therapy is still in development [3][4][5][6]. Unlike ultrasound diagnosis, which usually has no effect on tissue, ultrasound therapy is a technique that utilities the high intensity energy carried by ultrasound to damage the tissue in a certain region. Compared to traditional therapy methods, ultrasound therapy has a big advantage: it is noninvasive. Also compared to other noninvasive methods, ultrasound therapy is free of ionizing radiation, low cost and easy to operate. All of these make ultrasound therapy very attractive to clinicians.

1

In general, ultrasound absorption is the basic heating mechanism for ultrasound. Human tissue is a dissipative material, and energy carried by ultrasound will be dissipated in human tissue when ultrasound propagates through the tissue. A temperature rise in the local area will be induced [7][8][9]. This local temperature rise can be used to achieve therapeutic purposes. To induce the desired temperature rise, high intensity ultrasound is required. To achieve high intensity while maintaining the noninvasive character, a focused ultrasound source is used, which was first introduced by Lynn *et al.* [10][11] Low intensity ultrasound is generated at the surface of the transducer, and the rays of sound are focused either mechanically or electronically at the focal region. The whole mechanism is similar to using a magnifying glass to produce a hot spot of sunlight. Therefore, out of the focal region, the sound intensity is low and not harmful to the tissue. High intensity is obtained only in the focal region.

When High Intensity Focused Ultrasound (HIFU) is applied to tissue, the temperature rise caused by ultrasound can be predicted by the Bioheat Transfer Equation (BHTE) [12] which is presented below in axially symmetric form:

$$\frac{\partial^2 T}{\partial r^2} + \frac{1}{r}\frac{\partial T}{\partial r} + \frac{\partial^2 T}{\partial z^2} - \frac{\rho C}{\kappa}\frac{\partial T}{\partial t} + Q = 0 \qquad (1.1)$$

where T is the temperature, ρ the density of tissue, C the heat capacity of tissue, κ the thermal conductivity of tissue, r and z are the radial and axial location respectively, and Q is the power deposition per unit volume and a function of time and location, which can be related to the sound field with [1]

$$Q = \frac{2\alpha}{\rho c \omega^2}\left(\frac{\partial p}{\partial t}\right)^2 \qquad (1.2)$$

for a plane wave of constant angular frequency, where α is the absorption coefficient, c is the sound speed, ω is the driving frequency and p is the sound pressure. This model yields good

predictions at low intensity ultrasound if the sound properties of tissues can be measured precisely [13]. In reality, tissues are complex mixtures of many proteins and living cells, so the determination of the sound properties may become very complicated.

Another problem related to ultrasound therapy is cavitation, which may happen when high intensity ultrasound is used. Cavitation is usually induced by the negative pressure swing of the ultrasound field. A mechanical index is usually used to indicate the relative likelihood of adverse bioeffects during exposure to ultrasound [14]. During the tension phase of the ultrasound field, the existing cavitation nuclei (usually stabilized gas pockets [15]) grow and become oscillating micro-bubbles, which will change the local sound properties and cause the redistribution of the sound field. The occurrence of cavitation has a threshold value and this is one of the main features of cavitation heating in ultrasound therapy. The temperature field is going to change as well due to the redistribution of the sound field. Figure 1.1 is an example of the measured peak temperature in a tissue phantom with an ultrasound frequency of 1 MHz. For the temperature measurement, one can find the details in Chapter 4. The x-axis is the peak negative focal pressure amplitude. (Throughout this dissertation, unless otherwise indicated, all the pressures we will refer to are negative pressures). In Figure 1.1, at low driving pressures, the peak temperature rises are very smooth and has relatively small error-bars. When the driving pressure increases to around 2.3 MPa, erratic temperature jump is observed, and the temperature measurement becomes less repeatable. As the driving pressure further increases, a large peak temperature jump is observed with corresponding large error-bars. Finally, the peak temperatures drop again at even higher pressures. In this measurement, the temperature jump corresponds to the inertial cavitation threshold. One observes a significant peak temperature rise after cavitation occurs. The eventual peak temperature drop is due to the shielding effect of cavitation, which will

be discussed in Chapter 5. From this example, the features of heating behavior when cavitation is present can be summarized as:

1. Threshold dependent;

2. Erratic heating (large error bars);

3. High peak temperature rise;

4. Shielding effect at high driving pressures.

None of these features can be easily explained just by equation 1.1 and 1.2. Some researchers tried to explain this behavior by using nonlinear sound propagation models [16][17][18] or taking account the change of the sound properties in tissue at different temperatures [19]. They can not, however, explain all the features we mentioned above. Cavitation becomes the only possible mechanism to explain this phenomenon. New models are needed to understand and predict this phenomenon as ultrasound becomes a more and more powerful and widely used therapeutic tool all over the world.

Most often, ultrasonic cavitation is considered dangerous and should be avoided [20] in clinical use due to the erratic behavior of cavitation, with a few exceptions [21][22]. However, this physical phenomenon has the potential to improve ultrasound therapy. The presence of micro-bubbles in the target region can improve the efficiency of ultrasound therapy as well as aiding imaging. All of these considerations motivated the current work as an effort towards understanding bubble-enhanced heating and improving ultrasound therapy.

1.2 Review of literature

Scientists have been researching ultrasound therapy for over 70 years. The initial work on the application of high intensity ultrasound to problems in medicine dates back to the 1920s and 30s. Biological, physical and chemical effects due to high intensity ultrasound were reported in

4

the early days [23][24][25][26][27]. Since then, many experiments have shown that cavitation plays a big role during lesion formation above a threshold pressure. Most of the early work was carried out by Fry *et al.* at the University of Illinois [28][29][30][31][32]. They reported cavitation activity in frog and cat brain. Lele and co-workers [33] observed bubble-enhanced heating and boiling when cavitation was present. Their results also included the measurement of the acoustic emission from the samples. From the subharmonic and broadband noise emission detected, they concluded that of the boiling or screening is due to the presence of cavitation. Hynynen [34] implemented an *in vivo* experiment in dog thigh muscle. 1-s CW tone bursts were used at frequencies ranging from 0.246 MHz to 1.68 MHz and a range of pressures. The temperature was measured by a single thermocouple and cavitation was monitored by a focused ultrasound transducer hydrophone with a resonant frequency 0.5 MHz. He found a threshold for thermally significant cavitation, which is indicated by a significant increase in temperature, a loss of smooth temperature rise during the insonation and a significant reduction in the acoustic power transmitted through the tissue. He concluded, however, it was unlikely that the present diagnostic ultrasound units which operated at high frequency and in pulsed mode could cause cavitation in tissues. Clark and ter Haar [35] observed an enhanced heating and sometimes suppressed heating *ex vivo* in liver and dog prostate. They found at high power level, the temperature rise can cause a local change in tissue properties. This change acts like a barrier to ultrasound energy and may induce a significant temperature rise. They claimed that the barrier could be due simply to an increase in attenuation resulting from denaturization (Bush *et al.*[19]) or it could be a result of bubbles forming near the focus. They also reported a few bubbles were seen sometimes in the lesions on dissection. Miller and Gies [36] observed indirect evidence for bubble-enhanced heating on mouse intestine. They saw evidence for a high temperature rise and the presence of

bubbles, but they concluded that heating and cavitation appeared to have largely independent roles in vascular bioeffects on mouse intestine.

A hyperechoic region which was speculated to be bubbles has been seen at the HIFU treatment site immediately after HIFU [29][37][38]. Several groups detected subharmonic signals from which they deduced bubbles existed in the hyperechoic region. Vykhodtseva *et al.* [39] also suggested a potential for cavitation-based ultrasound therapy. Watmough *et al.* [40] observed enhanced heating in the presence of bubbles artificially introduced via a porous solid inclusion in a gel. Evidence for ultrasonically induced cavitation related heating was also reported by Sanghvi *et al.*[41] and ter Haar *et al.* [42].

More recently Bailey *et al.* [43] studied the effect of overpressure on focused ultrasound lesion shapes *in vitro*. They found at high intensity levels, lesions formed with no overpressure were tadpole-shaped, but lesions formed with high overpressure remained cigar-shaped. They concluded this result supported the hypothesis that bubbles contributed to the tadpole-shaped lesion distribution.

Holt and Roy [44] observed bubble-enhanced heating in an agar-based tissue-mimicking phantom from focused, MHz-frequency ultrasound. Their findings were characterized by a threshold dependence and erratic heating above the threshold. They concluded the presence of bubbles was the only possible explanation. They also discussed mechanisms for bubble-enhanced heating, including viscous dissipation from bubble oscillations and absorption of the sound emitted by oscillating bubbles. Quantitative estimates for single bubble thermal powers were on the order of 10 mW, compared with ~ 1W from the primary absorption.

Hilgenfeldt *et al.* [45][46] modeled the energy deposited from bubbles of μm-size and driven by diagnostic ultrasound pulses. They considered the effect of viscous dissipation and acoustic emissions from bubbles. They reported that the strong absorption of the radiation results

6

in a temperature rise as high as 100 K for driving pressure around 3 MPa at a distance of 1 μm from the bubble surface. Chavrier *et al.* [47] investigated the emissions from bubbles and the resulting absorption of the sound; a "global attenuation coefficient" is used in their energy equation to account for the presence of the bubble-enhanced heating.

Edson [48] extended the work of Holt and Roy [44] in his Ph. D dissertation. He also used an agar-based phantom, and he used a passive cavitation detector (PCD) to monitor the presence of bubbles. His experimental results showed that the PCD detected (primarily inertial) cavitation and coincided with enhanced heating. In addition, he calculated the bubble-related power deposition in a reasonable parameter space, and, by estimating the bubble numbers in the gel to be on the order of 10-100, he could predict the observed temperature rise in a tissue-mimicking phantom.

Micro-bubble based contrast agents are often used in medicine. Although in most cases the use of contrast agents is for imaging purposes, the bioeffects induced by these micro-bubble sometimes can not be ignored [49][50][51][52]. Wu studied the heating due to a kind of contrast agent using a disk model [53]. Fujishiro *et al.* [54] investigated the enhanced tissue damage due to micro-bubble based contrast agents in a beef liver. They reported an increase in the measured temperature rise by a factor of 1.7 in the presence of a micro-bubble based contrast agents, as compared to control samples. The authors concluded that contrast agents could be used to enhance the thermal effect of ultrasound.

Acoustically induced cavitation also plays a role in hemostasis [55]. Poliachik *et al.* [56] investigated the effect of HIFU on platelet activation, aggregation and adhesion to a collagen-coated surface. They found a substantial correlation (r^2=0.76) between aggregation and cavitation occurrence. Noble *et al.* [57] drew the same conclusion in a study of spleen hemostasis using HIFU.

7

The study of micro-bubbles has become an "old subject", and one may refer to *The Acoustic Bubble* [15] for a review of the early and linear theories. Lord Rayleigh [58] derived the first equation to explain the collapse of a steam cavity, which is now modified to account for surface tension, viscosity and compressibility of the surrounding medium and known as the Rayleigh-Plesset equation [15][59]. The Keller-Miksis equation [60][61] is another suitable radial equation which can better account for large amplitude oscillation of bubbles. All these bubble models assume a spherical shape bubble. Bubbles oscillating with sufficient amplitude may loss their spherical stability, and their surface evolution is governed by shape oscillation equations [62][63][64][65][66], which may result in break-up of the bubbles. The bubble equilibrium radius is determined by rectified diffusion [67][68] in the sound field. Growth through rectified diffusion has an important effect on bubble dynamics. Eller and Flynn [67]derived an expression for the rectified diffusion threshold; their grow rate results are valid when bubbles are at threshold conditions. Fyrllas and Szeri [69] developed another theory, and they get similar results as Eller and Flynn for the threshold conditions. Their results provide a better prediction for growth rates when bubbles are forced away from the threshold conditions. Shape stability and rectified diffusion will govern the evolution of possible bubble size distributions in HIFU treatment.

The tissue damage caused by cavitation may include mechanical damage and thermal damage [70]. Mechanical damage is caused by cavitation mechanical movement; especially when bubbles break up, the surrounding medium can be torn apart. Thermal damage is due to excess energy deposition when bubbles are present. The thermal energy deposition due to bubbles can be ascribed to three mechanisms: the heat from viscous losses, the bubble's acoustic radiation which is then absorbed and heat conduction. Using a numerical model, we can calculate the heat from those three mechanisms. For μm size bubbles at MHz frequencies, and MPa driving pressures, most of the heat comes from radiation and viscosity [44][48]. Under the influence of external

acoustic pressure, bubbles will oscillate and as a result, generate heat due to the viscosity of the host medium. In addition, the oscillating bubble acts like a radiation sound source whose energy is absorbed by the medium. Which mechanism is dominant is related to the bubble motion, which in turn is dependent upon bubble size, acoustic and material parameters.

The nature of bubble motion gives rise to two broad classifications [71]: noninertial (or stable) and inertial cavitation activity. Noninertial bubbles can be identified by a relatively repetitive radial motion of the bubble wall, and the motion may last many cycles. For a liquid with the viscosity of water, Prosperetti's results [72][73] indicated that the damping due to viscous dissipation is smaller than that of acoustic radiation for a superresonant bubble on the order of 10 microns at 1 MHz. (Superresonant bubbles are those bubbles which are larger than the size whose linear resonance frequency is 1 MHz, and we will refer to bubbles which are smaller than the resonant size as subresonant bubbles.) But in the parameter range of importance in the present study, the contribution of viscous dissipation may become more important due to the large viscosity value in the phantom (Edson [48]). Inertial cavitation is marked by an explosive bubble growth followed by a violent collapse. The motion is nonlinear and will not last many cycles or even one cycle. Inertial cavitation occurs at higher acoustic pressures than noninertial cavitation for a given equilibrium radius and liquid properties. At 1 MHz, for subresonant bubbles behaving inertially, radiation becomes more important than viscous dissipation as a means of thermal power deposition. This can be attributed to the broadband emission of sound at the collapse, and the fact that higher frequencies are more efficiently absorbed in tissue or tissue-mimicking materials.

However, to more accurately predict this temperature rise, one needs to know the threshold pressure for bubble oscillations and the time evolution of the bubble size distribution. The threshold tells us where the BHTE equation needs to be modified and the bubble size

distribution allows us to evaluate the heat contribution from bubbles. All the models discussed so far to account for bubble-enhanced heating (Chavrier *et al.* [47], Holt and Roy [44], Edson [48]) need to estimate the exact number and size of bubbles at the focal region to predict the temperature rise. Chavrier *et al.* assume different bubble densities to calculate the heating and use the viscosity of water. Edson set a range of 0.5μm to 50 μm for bubble size and 0.0005 kg/m·sec to 0.5 kg/m·sec for viscosity in order to capture all likely bubble behaviour. However, the actual bubble size parameter space may be much smaller than the one he used in his simulations since a much conserved estimate about the parameter space was used.

1.3 The goal of this research

The goal of this study is to investigate bubble dynamics in the HIFU regime, in order to understand the bubble-enhanced heating in a tissue-mimicking material. To begin, we will use a nonlinear bubble dynamics model to investigate the bubble oscillations in the HIFU regime. The goal for this theoretical effort is to place boundaries on the time-dependent bubble size distribution, which is determined by two threshold-dependent phenomena occurring for nonlinearly oscillating bubbles: shape instability and growth by rectified diffusion. The two thresholds will be calculated in this study, and the growth rate of bubbles is also calculated. Before we start to describe the theoretical model, we need to determine the viscosity of the tissue phantom we use. The viscosity has an important effect on the cavitation (Allen, Roy and Church, [74]). The tissue phantom we use exhibits viscoelastic properties, and the viscosity will be strain-rate dependent [44]. Here we will consider a range of viscosities and solve the bubble motion by assuming a Newtonian fluid. We chose the value of viscosity from 0.0005-0.5 kg/(m sec) and the bubble equilibrium radii we investigate are from 0.5-50 microns. From Edson's experiment, we know the pressure threshold for the onset of bubbles in our tissue-mimicking phantom is about

1.8 MPa under 1 second insonation time. With this in mind, we will choose the acoustic amplitude to be 1 MPa, 1.5 MPa, 2.0 MPa, 2.5 MPa, and 3.0 MPa. This covers the entire range of acoustic amplitude used in Edson's and Holt & Roy's experiments. In this study, we will predict the possible bubble size distributions which will in turn bound predictions for bubble-enhanced heating. Also, the thermal energy deposition for these bubbles will be calculated. By assuming appropriate bubble densities and assuming no interaction between bubbles, we can match our simulation to the measurements.

The second part of this study consists of experimental investigations. Bubble-enhanced heating is a very complicated problem. Theoretical investigation alone is not enough to understand this complex problem since it is not quite clear what is really going on. The experimental evidence can serve as verification for the theories or instruct theorists to build a correct model. The experiments are conducted in a tissue-mimicking phantom. Tissue phantoms possess homogenous sound properties. A uniform tissue phantom can allow us to predict the primary sound field and focus on the effect of cavitation. In addition, the use of tissue phantoms is less expensive than *in vivo* experiments. We will present the bubble-enhanced heating results for different dissolved gas concentrations, and will include acoustic emission measurements. For some experiments, we used contrast agents to control the initial bubble size distribution in the tissue phantom. The peak temperature results are presented with and without contrast agents. Passive cavitation detector (PCD) experiments help us to distinguish inertial cavitation from noninertial cavitation. By matching the peak temperature rise in the measurements to our theoretical model, we can infer the bubble densities in the tissue phantoms.
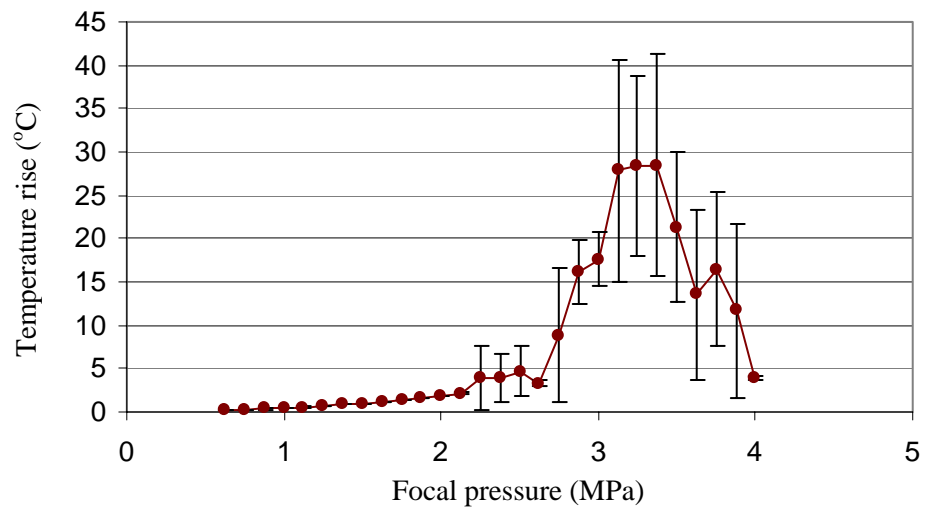
Figure 1.1 An example of measured temperature rise by a thermocouple in a tissue phantom at frequency of 1 MHz for a 1-s CW tone burst insonation.

Chapter 2

Bubble Dynamics

Before we begin to discuss the problem of enhanced heating due to cavitation, it is important to understand the cavitation behavior in the regime where we are going to work. Bubble oscillations involve the interaction of two-phase fluids in which the bubble itself is a nonlinear oscillator. In the region of HIFU, the strong driving pressure applied to the bubble will result in strong nonlinearity, yielding at times period doubling and chaos. This chapter is devoted to bubble dynamics encountered in HIFU applications. Numerous pioneers have made significant contributions to bubble dynamics in general, and a whole set of theories about bubbles has been developed. No new theory is going to be developed in this chapter. An existing bubble dynamic theory is going to be chosen to investigate the strong nonlinear oscillations of bubbles in our current working regime. The frequency we are going to use is 1 MHz, which is the same as we are going to use in our experiments. A Newtonian fluid bubble dynamic model is assumed. The tissue phantom actually is a viscoelastic material, which has a shear strain rate dependent viscosity. However, the Newtonian fluid assumption simplifies the problem greatly. We integrate the Newtonian model over a large viscosity range, from 0.001 kg/m/s to 0.5 kg/m/s. The choice of a large range of viscosity is to supplement this Newtonian fluid assumption since in reality the real viscosity is covered by this range. Only spherical oscillation is considered for stable oscillating bubbles in our simulation. Nonspherical shape oscillations will either cause the bubble to break up or be suppressed and finally decay away. Two important thresholds are going to be presented in this chapter: one is the bubble shape instability threshold, which determines whether

the oscillation of a spherical bubble is going to be stable; the other is the rectified diffusion threshold, which determines the bubble equilibrium radius and whether bubbles are going to grow or dissolve. Taken together, these two thresholds together will define an allowed bubble size distribution region. The bubble growth rate also will be calculated in this region, and will be important to the cavitation-related heating in later chapters.

2.1. Radial Motion equation

For a spherical bubble, the dimension of a bubble depends on the bubble radius. The task of bubble dynamics is to determine how the radius changes in response to the applied pressure. Several bubble models with spherical symmetry have been developed since 1917 which Lord Rayleigh [58] published the first theory to deal with cavitation in an inviscid, incompressible liquid. After that, models which could account for viscosity and the compressibility of a Newtonian liquid were developed. A discussion of the effect of different models on our results is presented in Appendix A.

Throughout this work, the radial equation of motion we use is the so-called Keller-Miksis equation which was first derived by Keller and Miksis in 1980 [60][61], and has the form,

$$
\left(1 - \frac{\dot{R}}{c_L}\right) R\ddot{R} + \frac{3}{2}\left(1 - \frac{1}{3}\frac{\dot{R}}{c_L}\right)\dot{R}^2 = \frac{1}{\rho}\left(1 + \frac{\dot{R}}{c_L} + \frac{R}{c_L}\frac{d}{dt}\right) p_B
$$
$$
- \frac{1}{\rho}\left(1 + \frac{\dot{R}}{c_L}\right)\left(p_\infty - p_s\left(t + \frac{R}{c_L}\right)\right)
$$

(2.1)

where dots denote time derivatives, R is the bubble radius, c_L is the speed in the surrounding medium, ρ is the density of surrounding medium, p_∞ is the ambient pressure, $p_s(t)$ is the applied acoustic field pressure and p_B is the pressure on the surrounding medium side of the interface between the medium and the bubble. p_B is related to the internal pressure p of bubble by the following formula:

14

$$p = p_B + \frac{2\sigma}{R} + 4\mu\frac{\dot{R}}{R} \tag{2.2}$$

where σ is the surface tension coefficient, and μ the shear dynamic viscosity. The sound field we chose in this study is sinusoidal:

$$p_s(t) = p_a \cos \omega t \tag{2.3}$$

with p_a the acoustic amplitude and ω the driving angular frequency. Our model is not limited to sinusoidal forcing, but experimental [44] and numerical [48] results show that with our experimental material parameters, all sound fields are very weakly nonlinear at most, therefore the harmonics of ω are unimportant.

Internal pressure

To solve the above radial equation, the internal pressure of bubble is needed. An ideal gas law is often assumed for the behavior of the internal gas of bubble and then a polytropic relation between the internal pressure and the radius of bubble is used in many studies. This has the following form,

$$\frac{p}{p_0} = \left(\frac{R_0}{R}\right)^{\eta}, \tag{2.4}$$

where η is the polytropic index and p_0 is the pressure inside the bubble at equilibrium. The use of the polytropic relation requires knowledge of the polytropic index η, for air which is 1 if the oscillations are isothermal and 1.4 if they are adiabatic, and otherwise some value in between. The temperature and the pressure inside the bubble are assumed to be uniform. The limiting cases of isothermal or adiabatic oscillations are seldom true for a real oscillating bubble. Prosperetti *et al.* [75] suggested a new model to better account for the thermal damping. They solved for a nonuniform temperature distribution inside the bubble with the temperature at the bubble wall the

ambient temperature. The results from this model showed good agreement with experimental results in a single bubble sonoluminescence study [65][76][77][78].

Prosperetti's internal pressure model

A model for the internal pressure of the bubble is described in detail in Prosperetti *et al.*[75], Kamath *et al.* [79]. This model accounts for heat transport by convection and conduction to and from the surrounding medium. The model was derived by assuming an ideal gas and spatial uniformity of the gas pressure inside the bubble. The internal pressure p can be found by integrating:

$$\dot{p} = \frac{3}{R}\left[(\gamma-1)K\frac{\partial T}{\partial r}\bigg|_R - \gamma p\dot{R}\right]$$

(2.5)

where γ is the ratio of the specific heats of the gas and K is the gas thermal conductivity. The gas temperature field $T(r,t)$ is obtained from

$$\frac{\gamma}{\gamma-1}\frac{p}{T}\left(\frac{\partial T}{\partial t} + \upsilon\frac{\partial T}{\partial r}\right) = \dot{p} + \frac{1}{r^2}\frac{\partial}{\partial r}\left(\kappa r^2\frac{\partial T}{\partial r}\right)$$

(2.6)

with

$$\upsilon = \frac{1}{\gamma p}\left[(\gamma-1)K\frac{\partial T}{\partial r} - \frac{1}{3}r\dot{p}\right]$$

(2.7)

where υ is the radial velocity of the gas inside of the bubble. The temperature boundary condition for a relatively cold liquid, such as water at normal ambient temperature, is,

$$T[r = R(t), t] = T_\infty,$$

(2.8)

where T_∞ is the undisturbed liquid temperature.

Numerical method developed by Kamath and Prosperetti

The solution of this set of equations of motion (2.5)-(2.8) requires numerical integration. Kamath and Prosperetti developed a Galerkin spectral method [79] which we are going to use in

this work and be described following. For numerical work, it is convenient to use the following transformation.

$$y = r/R(t) \tag{2.9}$$

$$\tau = \int_{T_\infty}^{T} K(\theta)d\theta . \tag{2.10}$$

For the thermal conductivity, a linear relation $K(T)=AT+B$ is used, with numerical values $A=5.528*10^{-5}$ W/m K^2 and $B=0.01165$ W/m K^2 for air in the range 200K-3000K and $A=3.2*10^{-5}$ W/mK^2 and $B=0.009$ W/mK^2 for argon (Hao *et al.* [65]).The following nondimensional variables are defined,

$$R = R_0 R_* , \ t = t_* / \omega, \ p = p_0 p_* , \ T = T_\infty T_* , \ \tau = D_0 p_0 \tau_* , \ D = D_0 D_* \tag{2.11}$$

R_0 and p_0 are the values of radius and internal pressure at equilibrium,

$$p_0 = 2\sigma / R_0 + p_\infty , \tag{2.12}$$

p_∞ is the ambient pressure, ω is the frequency and D_0 is the equilibrium value of thermal diffusivity which for a perfect gas, is given by,

$$D_0 = [(\gamma - 1)/\gamma][K(T)T / p]. \tag{2.13}$$

With these new variables, the pressure and temperature equations have the following form, where asterisks are omitted for clarity:

$$p' = \frac{3}{R}\left(\frac{\gamma-1}{R}\chi\frac{\partial\tau}{\partial y}\bigg|_{y=1} - \gamma p\overline{U}\right)$$

$$\frac{\partial\tau}{\partial t} + \frac{\gamma-1}{\gamma}\frac{\chi}{pR^2}\left(\frac{\partial\tau}{\partial y} - \frac{\partial\tau}{\partial y}\bigg|_{y=1} y\right)\frac{\partial\tau}{\partial y} - Dp' = \frac{\chi D}{R^2}\nabla^2\tau \tag{2.14}$$

where "'" means derivative with respect to dimensionless time and,

$$\overline{U} = R' \tag{2.15}$$

The parameter χ is defined by

$$\chi = D_0 \big/ \omega R_0^2 \qquad\qquad (2.16)$$

which is the square if the ratio of the thermal diffusion length to the bubble radius. Small values

of χ correspond to a nearly adiabatic bubble, while large values of χ indicate a nearly isothermal

behavior of the gas.

In terms of τ, the boundary condition (9) becomes,

$$\tau(1, t) = 0 \qquad\qquad (2.17)$$

With the linear relation used for the thermal conductivity, the dimensionless temperature T is,

$$T = (1/\alpha)\left(\{1 + 2[(\gamma - 1)/\gamma]\alpha\tau\}^{\frac{1}{2}} + \alpha - 1 \right) \qquad\qquad (2.18)$$

and

$$D = (1/p)\left[\alpha T^2 + (1 - \alpha)T\right] \qquad\qquad (2.19)$$

where $\alpha = AT_\infty / K(T_\infty)$.

With these new variables and omitting asterisks, the radial equation becomes,

$$\left(1 - \frac{\overline{U}}{c_*} + \frac{ZM}{Rc_*}\right)RU' + \frac{3}{2}\left(1 - \frac{\overline{U}}{3c_*} - \frac{2ZM}{3Rc_*}\right)\overline{U}^2 = Z\left\{\left(1 + \frac{\overline{U}}{c_*}\right)\left[p - p_s\left(t + \frac{R}{c_*}\right) - \frac{W + M\overline{U}}{R}\right]\right.$$
$$\left. + \frac{R}{c_*}\left(p' + \frac{W\overline{U}}{R^2}\right)\right\}$$

$$(2.20)$$

where,

$$Z = \frac{p_0}{\rho\omega^2 R^2}, \quad W = \frac{2\sigma}{R_0 P_0}, \quad M = \frac{4\mu\omega}{p_0}, \quad c_* = \frac{c_L}{\omega R_0} \qquad\qquad (2.21)$$

Kamath *et al.* [79] used the Galerkin spectral method to solve this problem. To apply the

Galerkin spectral method, the temperature terms are expanded in terms of Chebyshev

polynomials,

$$\tau_N = \sum_{k=1}^{N} a_k(t)\phi_k(y)$$

(2.22)

where a_k are the coefficients of the expansion, ϕ_k are the shifted Chebyshev polynomials [80],

$$\phi_n = \overline{T}_{2n} - \overline{T}_0,$$

(2.23)

and $\overline{T}_n$ are the Chebyshev polynomials. With these basis functions, the temperature equation reduces to,

$$\sum_{n=1}^{N}(\phi_k,\phi_n)\frac{da_n}{dt} = (\phi_k, N(\tau_N)) + \frac{\gamma-1}{\gamma}\frac{\chi}{pR^2}\frac{\partial\tau}{\partial y}\bigg|_{y=1}(\phi_k, L\tau_N),$$

(2.24)

for $k=1,2,...N$, where (,) indicates the scalar product and

$$L\tau_N = y\frac{\partial\tau_N}{\partial y},$$

(2.25)

Furthermore,

$$(\phi_k, N(\tau_N)) = 2\sum_{j=1}^{N}\omega_j\phi_k(y_j)$$

$$\times\left\{\frac{\chi}{R^2}\left[D[\tau_N(y_j)](\nabla^2\tau_N)\bigg|_{y_j} - \frac{\gamma-1}{\gamma p}\left(\frac{\partial\tau_N}{\partial y}\right)^2\bigg|_{y_j}\right] + D[\tau_N(y_j)]p'\right\},$$

(2.26)

with

$$\nabla^2\tau_N = \sum_{n=0}^{N}d_n T_{2n}, \quad \frac{\partial\tau_N}{\partial y} = \sum_{n=1}^{N}e_n T_{2n-1}$$

(2.27)

and

$$(\phi_n,\phi_m) = \int_{-1}^{1}\phi_n(y)\phi_m(y)\frac{1}{\sqrt{1-y^2}}dy = \frac{\pi}{2}\delta_{nm} + \pi$$

(2.28)

where e_n and d_n are given in the Appendix in the paper of Kamath *et al.* [79]

19

$$e_n = 4 \sum_{k=n}^{N} k a_k \tag{2.29}$$

and

$$d_n = b_n + 2g_n \tag{2.30}$$

where

$$\nabla^2 \tau = \frac{\partial^2 \tau}{\partial y^2} + \frac{2}{y} \frac{\partial \tau}{\partial y} = \sum_{n=0}^{N} b_n T_{2n} + 2 \sum_{n=0}^{N} g_n T_{2n} \tag{2.31}$$

and

$$f_n g_n = 8 \sum_{\substack{k=n+1 \\ k+n=odd}}^{N} k a_k, \tag{2.32}$$

$$f_n b_n - b_{n+1} = 2(2n+1)e_{n+1}, \tag{2.33}$$

and $b_N=0$. Here,

$$f_n = \begin{cases} 0 & if \ n < 0, \\ 2 & if \ n = 0, \\ 1 & if \ n \geq 1. \end{cases}$$

If we set

$$y \frac{\partial \tau_N}{\partial y} = \sum_{n=0}^{N} c_n T_{2n}, \tag{2.34}$$

then,

$$(\phi_k, L\tau_N) = (\pi/2)(c_k - 2c_0), \tag{2.35}$$

where

$$c_k = \frac{1}{2}(f_k e_k + e_{k+1}).$$

In the numerical integral, the Gauss points y_j and weights ω_j can be chosen as

$$y_j = \cos[\pi(2j-1)/4N], \quad \omega_j = \pi/2N \tag{2.36}$$

for j=1,2,…, N.

All derivatives have been described in detail by Prosperetti *et al.* [75] and Kamath *et al.* [79]. With the above transformation, the original partial differential equation (PDE) will be reduced to a set of ordinary differential equations (ODEs). The ODE solver ODE15s in MATLAB was used to solve the resulting set of ODEs. A relative error tolerance of 1e-6 and an absolute error tolerance of 1e-7 are used in the simulation to assure the convergence of the solution. The results for different tolerances are shown in Figure 2.1.

2.2 Stability of the spherical bubble

An oscillating spherical bubble can also develop shape oscillations. An instability to wavy surface perturbations will cause shape oscillations of a spherical bubble. Plesset [62], Eller *et al.*[81] Prosperetti [64], Hilgenfeldt *et al.* [66] and Hao *et al.* [65] have modeled the stability of a spherical surface using spherical harmonics to describe the perturbations. Consider a small axisymmetric distortion of the spherical interface *R(t),*

$$r = R(t) + a_n(t)P_n(\theta) \tag{2.37}$$

where P_n is the Legendre polynomial of degree *n*, $a_n(t)$ is the amplitude. The shape distortion consists of a superposition of surface oscillations whose amplitudes are given by $a_n(t)$. The problem is to determine how the $a_n(t)$ behave.

Holt and Gaitan [82] and Gaitan and Holt [83] have reported experimental observations of the onset of shape instability for a bubble in water. A comparison of those experimental results with predictions (Hao and Prosperetti [65]; Prosperetti and Hao [78]) shows quantitative agreement regarding mode n observed and dependence on bubble size for all models of bubble oscillation. The degree of quantitative agreement increases with increasing model accuracy in both the radial equation and the shape-mode coefficient equations (By using a lower tolerance,

we actually got better agreement than Hao and Prosperetti). For the radial mode used in the present dissertation, and with the following approximation, Hao & Prosperetti document that good quantitative agreement can be expected in the single bubble sonoluminescence range, where the driving frequency is around 20 kHz and driving pressure is 0.8-1.4 atm. The equation governing the time evolution of the $a_n(t)$ is;

$$\ddot{a}_n + B_n(t)\dot{a}_n - A_n(t)a_n = 0 \tag{2.38}$$

with

$$A_n(t) = (n-1)\frac{\ddot{R}}{R} - \frac{\beta_n \sigma}{\rho R^3} + \frac{2\nu\dot{R}}{R^3}\left[-\beta_n + n(n+2)(n-1)\frac{1}{1+2\,\delta/R}\right] \tag{2.39}$$

$$B_n(t) = \frac{3\dot{R}}{R} + \frac{2\nu}{R^2}\left[-\beta_n + \frac{n(n+2)^2}{1+2\,\delta/R}\right] \tag{2.40}$$

where $\beta_n = (n-1)(n+1)(n+2)$, ν is the kinematic viscosity, a_n is the amplitude of the n-th surface mode, and the boundary layer thickness δ is approximated by (Prosperetti, [63], Brenner *et. al.* [84],Hilgenfeldt *et al* [66])

$$\delta = \min\left(\sqrt{\frac{\nu}{\omega}}, \frac{R}{2n}\right) \tag{2.41}$$

$R(t)$ is obtained from the numerical solution of the equation of motion (2.1). The ordinary differential equation (2.38) can then be solved numerically using numerical values of R, $\dot{R}, and\ \ddot{R}$ from (2.1).

A suitable method for investigating parametric instability for periodic solutions is Floquet analysis (Nayfeh and Mook, [85]). Parametric instability occurs whenever the magnitude of the maximal eigenvalue of the Floquet transition matrix $F_n(t)$ of Equation (2.38) is larger than one. The Floquet transition matrix is defined by

$$
\begin{pmatrix} a_n(T_p) \\ \dot{a}_n(T_p) \end{pmatrix} = F_n(T_p) \begin{pmatrix} a_n(0) \\ \dot{a}_n(0) \end{pmatrix}
\qquad (2.42)
$$

where T_p is the period. In our study, unfortunately, we found for some of the parameter regions that Floquet analysis cannot be applied because of chaotic oscillations of the bubble radial motion [86][87].

The chaotic range is from about 2 μm to more than 20 μm for our working space at 1 MHz, at the pressure range of 1 MPa-3 MPa. All the results presented here for bubble shape instability come from observing the $R(t)$ curve and $a_n(t)$ curves as they were calculated combined with Floquet analysis. In the chaotic region, a small fluctuation (<1 nm) is given as the initial distortion, and the following approximation criterion is used for instability:

$$
\max\left(\frac{|a_2(t)|}{R(t)} \right) \geq 1 ,
\qquad (2.43)
$$

We solve the $R(t)$ curves for as many cycles as it takes to reach steady state, and observe the $a_n(t)$ curves. For periodic bubble oscillation, we still use Floquet analysis as well as observe the $R(t)$ and $a_n(t)$ curves to monitor the Rayleigh-Taylor instability. Thus our results actually can account for both Rayleigh-Taylor instability (governed by the $\ddot{R}$ term in A_n (2.39)) and parametric instability (governed by the $\dot{R}$ term in B_n in (2.40)). We integrate the equation for a sufficient number of bubble oscillation cycles, e.g., 300 cycles for a 20-μm bubble, to see if the oscillation of the bubble is stable or unstable. The above method worked well for subresonant bubbles, which is bubbles whose sizes are less than the size R_{res}, which would be resonant at the driving frequency (Linear R_{res} is about 3.3 μm for 1 MHz). For bubbles above the resonant size, the radial response becomes small and nearly linear. For this case, the mode which resonantly couples ($\omega_n = \omega_0/2$, i.e. 500 kHz) to the spherical oscillation will be the most unstable.

2.3 Rectified diffusion

The shape instability threshold is not enough to give us the bubble size. For a shape-stable bubble, its equilibrium radius may change because of rectified diffusion (Eller and Flynn [67]). In an acoustic field, bubbles may grow or shrink and give a larger or smaller contribution to bubble-enhanced heating, depending on the relative importance of the bubble damping mechanisms. The rectified diffusion threshold, at which the cycle-average diffusion of gas into bubbles is zero, may arrest the growth of some bubbles. Other bubbles may have a lower threshold, and so may grow until they reach the shape instability threshold and then break up into smaller bubbles; such bubbles may repeat the process of growth and subsequent break up.

A gas bubble will gradually dissolve (Epstein and Plesset [68]) and disappear as gas diffuses from the bubble into the surrounding liquid in the absence of a sound field due to the excess internal gas pressure required to balance the surface tension pressure of $2\sigma/R$. However, oscillations of the bubble caused by a sound field may cause "rectified diffusion", that is, gas may enter the bubble during a cycle and cause the bubble to grow. There are two elements that contribute to the so-called rectified diffusion: an 'area effect' and a 'shell effect'. While the bubble radius is less than the equilibrium radius, the gas pressure inside the bubble is greater than the equilibrium value and thus the gas will diffuse out of the bubble. Conversely, when the bubble radius is greater than the equilibrium radius, the gas inside is at a lower pressure than the equilibrium value and thus the gas diffuses from the liquid into the bubble interior. The net flow rate of gas, however, is not zero since the area of the bubble wall is different during the expansion and compression of the bubble. There will be a net influx of gas because the area of the bubble wall is larger during expansion. This is known as the area effect. The shell effect occurs because the rate of diffusion of gas in the liquid is proportional to the gradient of the concentration of the dissolved gas. As the bubble oscillates, a spherical shell of liquid surrounding the bubble will

change volume and so the gas concentration in that volume will also change. While the bubble expands, this shell becomes thinner and thus the gradient of the gas concentration will become higher. The rate of diffusion of gas into the bubble becomes higher. When the bubble contracts, the liquid shell becomes thicker and the gradient of gas concentration becomes smaller, and this will slow down the rate of diffusion of gas into the liquid from the bubble interior. These two effects combine to favor growth over dissolution for oscillating bubbles and give rise to the term "rectified diffusion" To give a complete description of the general diffusion problem for a gas bubble, we need an equation of motion, a diffusion equation and a heat-conduction equation in the bubble and the liquid.

2.3.1 Eller-Flynn's solution

Eller and Flynn [67] developed a solution to the rectified diffusion problem. They started from Rayleigh-Plesset equation and the diffusion equation they used was Fick's law of mass transfer,

$$\frac{dc}{dt} = \frac{\partial c}{\partial t} + \upsilon \cdot \nabla^2 c = D_g \nabla^2 c \ , \tag{2.44}$$

where c is the concentration of gas in the liquid, υ is the velocity of the liquid at a point, and D_g is the diffusion constant. By assuming the temperature to be constant in time and uniform in space, they were able to eliminate the heat transfer equation. Under the assumption of a high-frequency limit, to first order, they obtained a solution to the equation (2.44):

$$\frac{dn}{dt} = 4\pi R_0 D_g \left[A + R_0 \left(\frac{B}{\pi D_g t} \right)^{\frac{1}{2}} \right] c_s \left(\frac{c_i}{c_s} - \frac{A}{B} \right) , \tag{2.45}$$

with $c_s = c_0 \left[1 + \left(2\sigma / R_0 P_\infty \right) \right]$ and $A = \frac{1}{T_b} \int_0^{T_b} \frac{R}{R_0} dt \quad B = \frac{1}{T_b} \int_0^{T_b} \left(\frac{R}{R_0} \right)^4 dt$,

where n is the number of moles of the gas inside the bubble, R is the bubble radius, R_0 is the equilibrium bubble radius, p_∞ is the ambient pressure in liquid, T_b is the bubble period, σ is the surface tension, c_0 is the saturation gas concentration, and c_i is the gas concentration in the liquid.

As mentioned previously, the rectified diffusion threshold pressure is the point at which the average diffusion is zero. If the driving frequency is high enough so that the dimensionless quantity $(D_g/\omega)^{1/2}/R_0$ is much less than unity (Eller and Flynn [67]), for a given gas concentration c_i in the liquid, the threshold is given by

$$\frac{c_i}{c_0} = \left[1 + \frac{2\sigma}{R_0 p_0} \right] \frac{A}{B} \tag{2.46}$$

The bubble radius, $R(t)$ in (2.1) comes from the numerical solution of the equation of motion. $R(t)$ is solved numerically and substitutes into the above formula to get the threshold pressure. This allows the treatment of fully nonlinear motion.

2.3.2 Fyrillas-Szeri's solution

Our results so far suggest that bubble activity in our parameter space may be characterized as a process in which bubbles grow, break up, and then grow and break up again, or stay at a constant R_0. To investigate time-dependent bubble activity, we need to know how fast (or how slowly) bubbles grow. We can then predict the time evolution of an initial bubble size distribution, and then predict the temporal evolution of the bubble enhanced heating.

The well known theory by Eller and Flynn [67] has been investigated by many researchers. Crum [88] reports an extension to the threshold theory of Eller & Flynn, and experimental results of bubble growth rates away from threshold that far exceed the theoretical predictions. Numerical solutions of the convection-diffusion equation for the dissolved gas in the liquid are reported by Kamath and Prosperetti [89]. They claimed that away from saturation

condition, the theory of Eller and Flynn tends to over-predict the threshold driving pressure and under-predict the growth rate. In a 1994 paper, Fyrillas and Szeri [69] developed a new theory by the method of perturbation. Their method is described below.

Again, we start from the convection-diffusion equation. In spherical polar coordinates, the convection-diffusion equation is written as,

$$\frac{\partial c}{\partial t} + \frac{R^2(t)\dot{R}(t)}{r^2}\frac{\partial c}{\partial r} = \frac{D_g}{r^2}\frac{\partial}{\partial r}\left(r^2\frac{\partial c}{\partial r}\right)$$

(2.47)

where c is the mass fraction of the gas dissolved in the liquid, t is time, $R(t)$ is the time-dependent bubble radius, $\dot{R}$ is the bubble wall velocity, and D_g is the diffusivity of the gas in the liquid.

The boundary condition at the bubble surface is developed by Henry's law,

$$c(r = R(t), t) = \frac{p_g}{k},$$

(2.48)

where p_g is the partial pressure of the gas and k is the Henry's law constant. The initial condition and the far field conditions are

$$c(r, t = 0) = c(r \rightarrow \infty, t) = c_i$$

(2.49)

c_i is the gas concentration in the undisturbed liquid.

The rate of transport of gas across the bubble interface is

$$\frac{dm_G}{dt} = 4\pi R^2 D_g \frac{\partial c(r = R(t), t)}{\partial R}$$

(2.50)

where m_G is the mass of the gas in the bubble.

Fyrillas and Szeri used a perturbation method and split the concentration field into two time scales: Fast time, which stands for the oscillation of the concentration field and has a zero time average value; Slow time, which stands for a smooth part of concentration changing slowly with the slow diffusion process. We adopt their work in the following. To start the splitting, following others (Eller and Flynn [67]), first, a convenient new nonlinear time $\hat{\tau}$ is defined as,

27

$$\hat{\tau}(\tau) \equiv \int_0^\tau x^4(\theta)d\theta \, ; \tag{2.51}$$

the average of any quantities $f(U, \tau)$ is,

$$\left\langle f(U,\tau) \right\rangle_{\hat{\tau}} \equiv \frac{1}{\hat{\tau}(T)} \int_0^{\hat{\tau}(T)} f(U,\hat{\tau})d\hat{\tau} = \frac{1}{\int_0^T x^4(\tau)d\tau} \int_0^T f(U,\tau)x^4(\tau)d\tau \, , \tag{2.52}$$

where T is the dimensionless period of bubble oscillation, τ is the dimensionless time defined as $t=\tau/\omega_0$, ω_0 is the natural frequency of the bubble, x is the dimensionless bubble radius defined as $R=xR_0$ and U is the dimensionless coordinate defined as $U = \frac{1}{3}\left(\frac{r^3}{R_0^3} - x^3 \right)$,

Using this average, they split the boundary condition at the surface of the bubble as:

$$c(U = 0,\tau) = c_s p_G^*(\tau) - c_\infty = c_s \left\langle p_G^*(\tau) \right\rangle_{\hat{\tau}} - c_\infty + c_s \left[p_G^*(\tau) - \left\langle p_G^*(\tau) \right\rangle_{\hat{\tau}} \right], \tag{2.53}$$

where c_s is the saturation concentration in the liquid separated from gas within a spherical bubble, p_G^* is dimensionless pressure inside the bubble and is defined by $p_G^* = p_G / \frac{1}{2}\rho R_0^2 \omega_0^2$, and c is the concentration and has been normalized by dividing it by liquid density and then subtracting the concentration at infinity from the concentration field. Then the whole problem can be split into two parts: the oscillatory problem and the smooth problem. The oscillatory problem is therefore

$$\frac{\partial c_{os}}{\partial \tau} = \frac{1}{Pe} \frac{\partial}{\partial \sigma} \left(\left(3U + x^3(\tau) \right)^{4/3} \frac{\partial c_{os}}{\partial U} \right), \tag{2.54}$$

where *Péclet* $P_e = R_0^2 \omega_0 / D$, with the boundary and initial conditions

$$c_{os}(U = 0,\tau) = c_s \left[p_G^*(\tau) - \left\langle p_G^*(\tau) \right\rangle_{\hat{\tau}} \right]$$
$$c_{os}(U,\tau = 0) = c_{os}(U \to \infty,\tau) = 0 \tag{2.55}$$

The smooth problem is defined by

$$\frac{\partial c_{sm}}{\partial \tau} = \frac{1}{Pe} \frac{\partial}{\partial \sigma} \left(\left(3U + x^3(\tau) \right)^{4/3} \frac{\partial c_{sm}}{\partial U} \right) \tag{2.56}$$

28

with the boundary and initial conditions

$$c_{sm}(U = 0, \tau) = c_s \left\langle p_G^*(\tau) \right\rangle_{\hat{\tau}} - c_\infty$$

$$c_{sm}(U, \tau = 0) = c_{os}(U \to \infty, \tau) = 0$$

(2.57)

The sum of the solution to the oscillatory and smooth problems is the solution to the full

problem, i.e. $c(U, \tau) = c_{os}(U, \tau) + c_{sm}(U, \tau)$.

(2.58)

To solve these two problems, Fyrillas and Szeri employed expansions of forms

$$c_{os}(U, \tau) = c_{os}^0(Pe^{1/2}U, \tau) + \frac{1}{Pe^{1/2}} c_{os}^0(Pe^{1/2}U, \tau) + \cdots$$

(2.59)

and

$$c_{sm}(U, \tau) = c_{sm}^0(U, \tau) + \frac{1}{Pe} c_{sm}^1(U, \tau) + \cdots$$

(2.60)

After solving the problem, they found the oscillatory problem hardly contributes to the

slow diffusion problem, and the dominant contribution comes from the smooth problem which is

reasonable and expected.

Their main result is the expression for the rate of growth of bubbles away from the

threshold condition, following Eller [90], which is given by

$$\frac{dR_0}{dt} = R_0 \omega_0 \frac{R_g T_\infty \rho}{M p_\infty} \frac{1}{Pe} \left(1 + \frac{4\sigma}{3 R_0 p_\infty} \right)^{-1} \frac{\left(c_i - c_0 \left\langle p_G^*(\tau) \right\rangle_{\hat{\tau}} \right)}{\int_0^\infty \frac{dU}{\left\langle \left(3U + x^3(\tau) \right)^{4/3} \right\rangle_{\hat{\tau}}}}$$

(2.61)

where R_g is the universal gas constant, R_0 is the equilibrium radius of bubble, T_∞ is the

temperature of the surrounding liquid, ρ the density of liquid, M the molecule weight of gas

inside the bubble, p_∞ the ambient pressure, P_e the *Péclet* number, σ the surface tension, and c_0 the

saturation concentration in the liquid. The validity of this method depends on the *Péclet* number

being large, which can be easily satisfied in most cases. The rectified diffusion threshold is given when the growth rate is zero,

$$c_i - c_0 \left\langle p_G^*(\tau) \right\rangle_{\hat{\tau}} = 0 \,, \tag{2.62}$$

which is identical to Eller and Flynn's result, equation (2.46).

2.4 Results

In the experiment, the viscosity is uncertain. Given this we choose the range of viscosity from 0.0005kg/m/s to 0.5 kg/m/s for simulations, which covers most of the possible viscosity coefficients encountered in human soft tissue. We investigate a bubble size range from 0.5 μm to 50μm. The driving frequency using in all the simulations is 1 MHz. Other parameters we used in the simulation are c_L=1600 m/s, σ=0.0725 N/m, T_∞=20°C, p_∞=1 atm. ρ=1100 kg/m³.

2.4.1 The bubble shape instability

The figures below show the onset of bubble shape instability under an acoustic pressure p_a=1.0 MPa, 1.5 MPa, 2.0 MPa, 2.5 MPa, 3.0 MPa at excitation frequency of 1 MHz. We first present the results for shape instability regions in this regime. There are three different unstable regimes in this parameter space which can be divided by bubble size at our working pressures. We begin with the region in which the bubble radius is bigger than about 20 μm. This bubble radius is much bigger than the linear resonant size of bubbles at 1 MHz, which is of around 3.3 μm. For these "superresonant" bubbles, we simply calculate a critical value for bubble shape instability for each bubble size, assuming the bubbles oscillating linearly. We assume the Faraday instability [91][92] dominates the shape instability for big bubbles. The most unstable mode can be chosen as follows: We calculate the inviscid mode frequency for each Legendre mode, which

is given by Lamb [93] as $\omega_n = (n-1)(n+1)(n+2)\dfrac{\sigma}{\rho R_0^3}$. The most unstable mode has a mode

frequency which is exactly one-half of the driving frequency, as required by the Faraday parametric instability, then we chose several modes which are next to this mode to check for critical value for a given R_0. We finally choose the largest critical value as the threshold point. The critical values of the most unstable modes for all R_0 comprise the boundary of bubble shape instability. These results are presented in Figure 2.2.

The superresonant bubbles investigated in this study respond linearly. The instability of such bubbles is decided by the parametric Farady instability only. We are able to employ a threshold value to distinguish the stable and unstable region. The region above the threshold is the stable regime, while increasing the pressure will enlarge the unstable region. The increase of viscosity suppresses the instability of bubbles. In Figure 2.3, we show an example of bubble oscillation time series in this regime and an unstable a_{15} curve for driving pressure p_a=1.5 MPa.

If the bubble is smaller, in this case, about 2-20 μm, the bubble oscillation is not linear any more and not even periodic. In this "resonant" size region, for relatively lower viscosity, the bubble oscillation is chaotic. This chaotic oscillation is induced by the strong nonlinearity of bubbles and is not unexpected from the Rayleigh-Plesset equation. But again when the viscosity becomes higher, the nonlinearity will be suppressed and the bubble oscillation becomes linear. In Figure 2.4, the $R(t)$ curve of a chaotically oscillating bubble is shown. The chaotic oscillation of the bubble does not allow parametric instability to develop, which requires a periodic accumulation over many cycles. Instead, the dominant mechanism for instability for resonant bubbles will be the Rayleigh-Taylor instability, which can happen every time the bubble collapses. A typical unstable $a_2(t)$ is shown in Figure 2.4. In general, the Rayleigh-Taylor instability has a lower threshold value than the parametric instability threshold.

The third region of shape instability is the region below 2 μm, the "subresonant" regime. In the low viscosity region, the whole region is bounded essentially by a quasi-static Blake threshold (Akhatov et. al.,[94]) which is given by $p_B = p_\infty + 0.77 \dfrac{\sigma}{R_0}$ and $p_L = p_\infty - p_B$, where p_L is the pressure in the liquid immediately beyond the bubble wall and is defined

as $p_L = \left(p_\infty + \dfrac{2\sigma}{R_0} - p_v \right) \left(\dfrac{R_0}{R} \right)^{3\eta} + p_v - 2\sigma/R$. This also can be used to define a critical radius

$$R_c(p_B) = \frac{0.77}{p_B - p_0}.$$

Compared with the whole parameter regime, this is only a small region. However, complex instability phenomena occur in this regime. This is a region just above the Blake critical radius for inertial cavitation, which is a dynamic analogue of the static Blake threshold. The resulting giant response has been dubbed the "Blake resonance" by some researchers. The large expansion is due to the force imbalance across the bubble wall during the negative acoustic half-cycle. Bubbles just larger than some critical radius may expand more than $10R_0$, and collapse inertially. For driving pressures near 1 MPa and 1.5 MPa, subresonant bubbles are strongly periodic and the instability is dominated by the coupling of Rayleigh-Taylor instability and parametric instability together. Figure 2.4 shows some typical cases. Rayleigh-Taylor instability happens every cycle, however, it is not initially strong enough to break up the bubble. The parametric instability increases the amplitude of Rayleigh-Taylor instability cycle by cycle and that eventually breaks up the bubble. As the viscosity increases, the instability is suppressed finally. We still can employ a threshold to distinguish the stable and unstable region.

The stable and unstable regions for higher pressures, i.e. 2 MPa, 2.5 MPa and 3 MPa, are no longer simply connected in this Blake resonant region. For low viscosities, the response of bubble is period doubled. During the negative swing, the bubble expands so large that it can not

collapse completely during the next positive swing, and thus expands again during next acoustic cycle and finally finishes one collapse in two acoustic cycles and then repeats this process again. This is a classic period-doubling[95], which is usually an onset of chaos. For this case Rayleigh-Taylor instability happens only once every two acoustic cycles which is actually one oscillating cycle for the oscillating bubble. Parametric instability drives the amplitude of the Rayleigh-Taylor instability larger and larger and finally the bubble will break up.

When the viscosity increases, the amplitude of the period doubling oscillation is suppressed and decreases. The oscillation finally becomes parametrically stable and the amplitude of the Rayleigh-Taylor instability is suppressed cycle by cycle and decays to zero. The bubble oscillation becomes stable. However, when the viscosity continues increasing, the bubble will start away from the period doubling region and could finish two collapses in two acoustic cycles (Still period doubled, see Figure 2.5c) and eventually complete one collapse in one acoustic cycle (Figure 2.5 d). During this transition, bubbles change from collapsing once to collapsing twice in two acoustic cycles, and the collapse becomes stronger and the parametric instability happens again. Then again, when the viscosity increases, every oscillation becomes stable. Clearly a single shape instability threshold line is not an appropriate way to distinguish the unstable and stable regions. A family of *R(t)* curves is shown in Figure 2.5, corresponding to the locations shown on Figure 2.7.

Figure 2.6 and Figure 2.7 give the mapping of bubble shape instability for acoustic amplitudes: 2.6a) 1.0 MPa, 2.6b) 1.5 MPa, 2.7a) 2.0 MPa, 2.7b) 2.5 MPa, 2.7c) 3.0 MPa. The dark area is the unstable area and otherwise stable area. As a general observation, for small bubbles, the second mode is the most unstable mode. As the bubble size increases, mode 3 becomes the most unstable mode, and for even larger bubbles, mode 4 is the most unstable mode, and so on and so forth. We calculate modes 2, 3, 4, 5, 6 for the whole parameter range.

The complete shape unstable region consists of all the critical values from all the modes. Comparing the results of the different acoustic pressures shows different trends for subresonant and supperresonant bubble sizes. In general, for subresonant bubbles, as the acoustic pressures increase, the shape instability boundary shifts to a smaller bubble size. This means bubbles are more stable under a smaller acoustic pressure for the same viscosity. The trend is opposite for superresonant bubbles. If one traces a single mode, e.g. mode 3 (Figure 2.8), it is interesting to note that in the present parameter space, the critical value for the viscosity increases slowly and then after a certain radius near the fundamental resonance, it drops down as the bubble equilibrium radius increases. For the higher modes, the threshold shifts to bigger radii. The threshold tells us that bubbles below the shape instability boundary are unstable during the excitation of HIFU, and if there were preexisting nuclei with that size, they will simply break up after a very short time. Thus, only bubbles above the threshold will contribute to the temperature rise.

The disconnected shape instability regions in Figure 2.7 are caused by the strong nonlinearity of the oscillating bubbles. In all the simulations, we use the same initial conditions: $R(0){=}R_0$ and $\dot{R}(0)=0$. For these strong nonlinear oscillating bubbles, different initial conditions may yield different radial motions, i.e., in this case, it is likely there is another coexisting steady state solution (or attractor [87]) if different initial conditions are used.

2.4.2 Threshold for rectified diffusion

We calculated the growth rate via rectified diffusion for gas concentrations $c_i/c_0 =$ 1(saturated), 0.75, 0.5, 0.2, 0.1, 0.01, and 0.001. The rectified diffusion thresholds are the lines where the bubble growth rate is zero. The results for rectified diffusion thresholds are presented in Figure 2.9 and Figure 2.10. All the bubbles above the rectified diffusion threshold (which

corresponds to *[1+2σ/(R₀P∞)]A/B<cᵢ/c₀* in Eller and Flynn's theory) will shrink and bubbles below the threshold will grow (which corresponds to *[1+2σ/(R₀P∞)]A/B>cᵢ/c₀*) until they hit either the rectified diffusion threshold again or the shape instability threshold. That means after some time, all the shape stable bubbles will be trapped on a threshold boundary; therefore, for a certain viscosity coefficient, the asymptotic bubble size will be decided by these rectified diffusion thresholds.

First, we compare the results for different driving pressures at c_i/c_0=1.0. Figure 2.9 shows the effects of different driving pressures on the rectified diffusion threshold with R_0 vs μ on a logarithmic scale. The shape in each case for each driving pressure is similar and they all have the shape of 'n'. As the driving pressure increases, this threshold shifts and the growth region becomes larger. There is a cutoff line at the negative slope part, and the rectified diffusion thresholds drop rapidly at this region. This cutoff line corresponds to the critical radius defined by the Blake threshold at each driving pressure. The shape of the rectified diffusion threshold is not unexpected. As we discussed previously, for an oscillating bubble, rectified diffusion in general favors the growth of the bubble. For a strongly nonlinear oscillating bubble, both area effect and shell effect will strongly favor growth. A static bubble, however, will dissolve due to the surface tension. The rectified diffusion threshold will be somewhere in between these two limits, and bubbles should oscillate linearly. This will explain the three parts of the rectified diffusion threshold in the current parameter space. The critical radius defined by the Blake threshold is a threshold for inertial cavitation and this produces the negative slope of the rectified diffusion threshold. As bubble size increases, the responses become linear and so the positive slope of the rectified diffusion threshold enters here. As viscosity increases, bubbles respond more and more linearly and then another part of the rectified diffusion threshold falls into the transition area.

The rectified thresholds actually can be divided into two kinds: the stable threshold and unstable threshold. In the μ-R_0 space, positive threshold slopes represent unstable equilibria and negative threshold slopes represent stable equilibria. If a bubble encounters an ascending portion of the threshold, then a small increase in bubble size will cause the bubble to continue growing. If a growing bubble encounters a descending part of the rectified threshold, any perturbation can not force the bubble to leave the threshold, and it will be trapped there.

Next, we discuss results for different gas concentrations at the same driving pressure. Figure 2.10 shows the threshold for different gas concentrations under a driving pressure of 1 MPa. The right part of the threshold shifts to the lower-left corner in the parameter space for smaller gas concentrations, while the negative slope, which is bounded by the Blake threshold, hardly moves. That means that the stable critical radius for the rectified diffusion threshold becomes smaller at a lower gas concentration. When the gas concentration decreases from 1.0 to 0.1, the threshold does not shift very much, but from 0.1 to 0.01, there is a big jump between the calculated thresholds. The lowest gas concentration we can get in a preparation of the phantom is 0.1. However, for violent enough collapse, sonoluminescence results (Holt and Gaitan [82], Hilgenfeldt *et al.* [66]) have shown that only the noble gas participates in diffusion, N_2 and O_2 are dissociated during collapse and chemically bonded in water. This would expand the potential range from 0.1 to 0.001 (which represents the fractional concentration of argon in a phantom prepared with air concentration 0.1).

2.4.3 Which bubbles will contribute?

The main purpose of this study was to investigate, and if possible, bound the bubble size distribution which contributes to the enhanced heating during the HIFU treatment. Finding the thresholds for bubble shape instability and rectified diffusion, we can formulate an answer to this

question. Figure 2.11 shows the two thresholds in the same parameter space for a driving pressure of p_a=2.0MPa and c_i/c_0=0.1. The light area is shape stable and the dark area represents shape unstable region. The rectified diffusion threshold is shown at the same plot. For a bubble to enhance heating, first of all it should be shape stable. Therefore, only the light region is possible parameter space for bubble-enhanced heating. The presence of the rectified diffusion threshold further narrows down the possible bubble region since a bubble cannot give much contribution to the heating if it will dissolve in the sound field. In our case, since the bubbles are created from small nuclei and grow up, the rectified diffusion threshold will be the stop points for these bubbles to grow, and we will not consider the dissolution of bubbles.

Bubbles which contribute to heat generation will thus be trapped between the two thresholds. The whole area of possible bubble sizes has a roughly triangular shape in the current parameter space which is in between the two thresholds. Bubbles which will contribute to the heating are in this triangular area. The whole triangular area can be divided into two parts: an upper area and a lower area. In the lower area, bubbles will grow first and then they will hit the shape instability threshold and break up. As a result of this breaking-up, small bubbles may be created and grow again to hit the instability threshold and repeat the cycle. Bubbles in this area will always grow and break up. The heat generated by the bubbles in this region will also be affected by the bubble growth rate. In the upper area, all the bubbles will be trapped on the rectified diffusion threshold after a short time, and these bubbles will stably oscillate at that size.

2.5 Growth Rate Result

Using Fyrillas-Szeri's solution, we calculate the growth rate of bubbles in our current parameter space. First we compare the growth rate under the same driving pressure but different

gas concentrations in the liquid. Clearly, as the gas concentration in liquid increases, the growth rates of bubbles increase.

The growth rate calculation result agrees very well with the Blake critical radius in the low viscosity region. For the case of driving pressure p_a=1MPa, when the bubble equilibrium radius is below the critical radius, the growth rates are negative. This means the surface tension dominates the bubble dynamics and the bubble cannot grow. Where the bubble equilibrium radius is bigger than the critical radius, the growth rate of bubbles increases explosively, and for small bubbles (on the order of 1e-8 m) in saturated liquid, the growth rate even reaches 100 m/s! These results can be seen in Figure 2.12a. Figure 2.12b shows the growth rate for c_i/c_0=0.1. The small plots below these plots show the small details of the growth rate. As the gas concentration in liquid decreases, the bubble growth rates decrease. But small bubbles which are just above the critical radius still have the largest growth rate. As the viscosity increases, this critical radius shifts to larger bubble sizes.

Next, we concentrate on the same gas concentration but different driving pressures. In saturated liquid, as the driving pressure increases from 1 MPa to 3 MPa (Figure 2.13), the growth rates increase and also, as we have seen in last chapter, the rectified diffusion threshold, where the bubble growth rate is equal to zero, shifts to large bubbles. The increase of growth rate is clearly observed at small bubble sizes because the absolute growth rate is very large in that region, which can even reach 1e4m/s when driving pressure is 3 MPa. Beyond the resonance region, the growth rate decreases rapidly to close to zero.

2.6 Bubble size evolution

The results for bubble size evolution are shown in Figure 2.14. An array of different initial size bubbles starts to grow by rectified diffusion during the insonation, and the equilibrium

radius is presented as a function of time in the plot. The driving pressure is 2 MPa, and the dissolved gas concentration is 20%. When the viscosity is 0.05 N.s/m^2, the result shows a big difference between the bubble sizes after 0.002 s. However, as the insonation continues, the difference becomes smaller and smaller. For a 0.01 second insonation, the initial difference between bubble sizes is smoothed out, yielding a negligible final difference between the bubble sizes. When viscosity is 0.005N.s/m^2, we actually cannot see any significant difference caused by the rectified diffusion, and the differences between bubble equilibrium radii are negligible after the 0.01 second insonation. The evolution of the ΔR_0 between two bubbles is shown in Figure 2.15 for these two cases. ΔR_0 is the size difference between bubbles and which is defined in the caption of Figure 2.15. When viscosity is 0.05 N.s/m^2, a large ΔR_0 is observed right after insonation but as insonation continues, ΔR_0 approaches to 0. When viscosity is 0.005 N.s/m^2, ΔR_0 approaches 0 from the beginning of the insonation.

2.7 Discussion

The preceding chapter's work allows us to narrow down the possibilities for the dominant heating mechanism for the bubble-enhanced heating in high intensity focused ultrasound discussed in Holt and Roy [44]. As high intensity ultrasound is applied to tissue, the strong negative phase of the ultrasound will initiate cavitation when the intensity of the ultrasound is beyond some threshold value. After cavitation occurs, bubbles interact with the sound field and may grow, continue oscillating at some equilibrium radius or break up due to shape instability and then grow again. During this period, bubbles absorb energy from the sound field, which can cause a local temperature rise and eventually cause tissue damage. Energy deposition due to a single bubble has been well established, so if we can determine the bubble activity during

ultrasound insonation, it is not difficult to determine the temperature rise caused by these bubbles, and then we can evaluate the potential for thermal tissue damage.

To model this problem, now the difficulty is how to get accurate bubble motions during the entire insonation. The nonlinear oscillation of a spherical bubble has been very well studied and for a certain R_0, Rayleigh-Plesset equation can give us very good results for the oscillation of the bubble. Eller and Flynn's theory can tell us the equilibrium size of a bubble for a given pressure. Fyrillas and Szeri's theory allows us to calculate the bubble growth rate when a bubble is away from its equilibrium size. The whole problem now looks straightforward. But we have to mention: a). The growth rate for small bubbles just above the Blake threshold is dramatically high, b). calculation of the growth rate has used the equilibrium value of bubble oscillation. These facts suggest that a steady-state, time-average, based growth rate cannot be applied to these small bubbles without increasing large errors, because the fast growth keeps that bubbles far away from steady state and such a bubble may not complete even one cycle before its equilibrium radius changes. It also suggests that the oscillatory problem may play a role here. However, for a 1 second insonation time, that means 10^6 cycles, the contribution from these small bubbles cannot be big since bubbles will grow and pass that region in a matter of a few cycles. Thus these calculations should be valid for pulsed insonation providing the ultrasound pulse width is at least 100 cycles or 100 μs at 1MHz.

a)
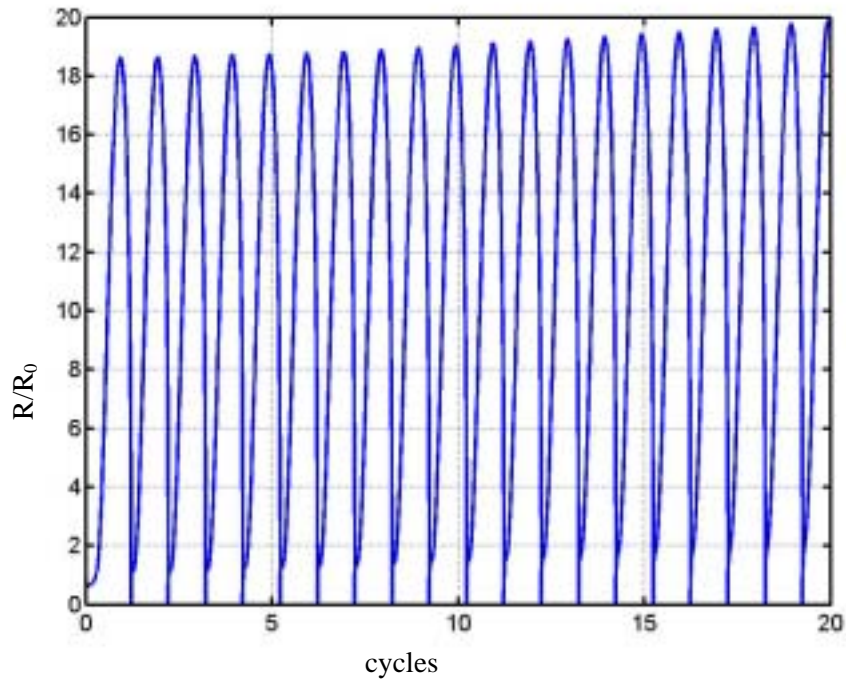
b)
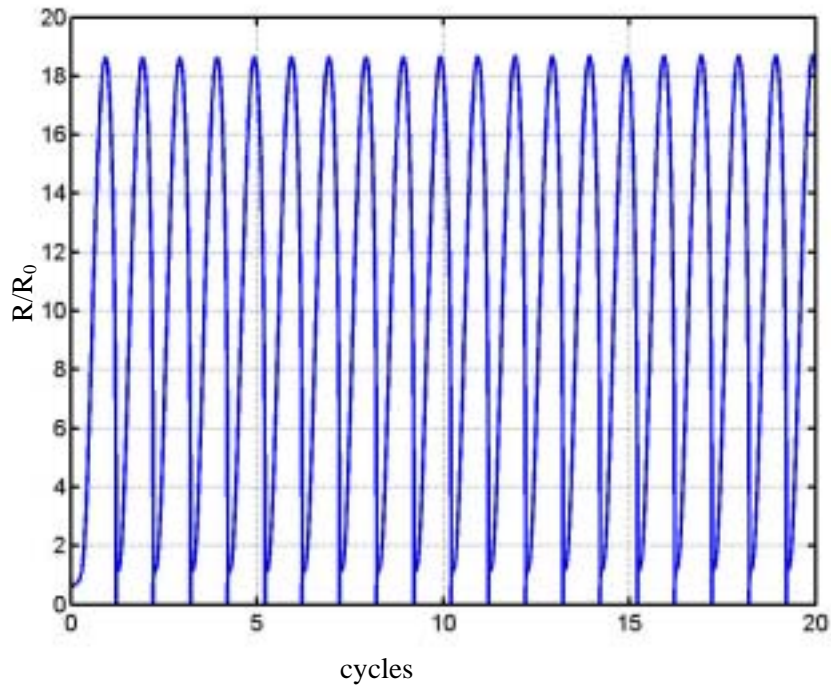
Figure 2.1 Examples of different tolerance results. a) Relative tolerance 1e-4 and absolute tolerance 1e-5; b) Relative tolerance 1e-6 and absolute tolerance 1e-7. Driving pressure 1 MPa, and R_0=0.5 μm at 1 MHz.
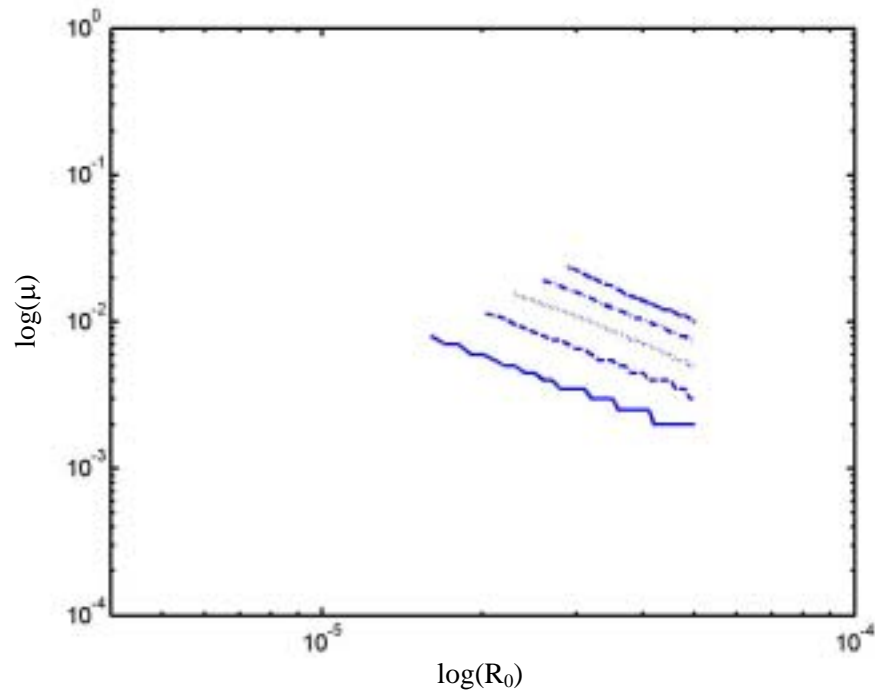
Figure 2.2 The bubble shape instability thresholds for big bubbles. Only the results of most unstable modes are shown here. These threshold lines are corresponding to 1.0 MPa, 1.5 MPa, 2.0 MPa, 2.5 MPa, and 3.0 MPa from top to bottom line respectively. The unit of μ is N.s/m^2 and the unit of R_0 is m.

a)

b)
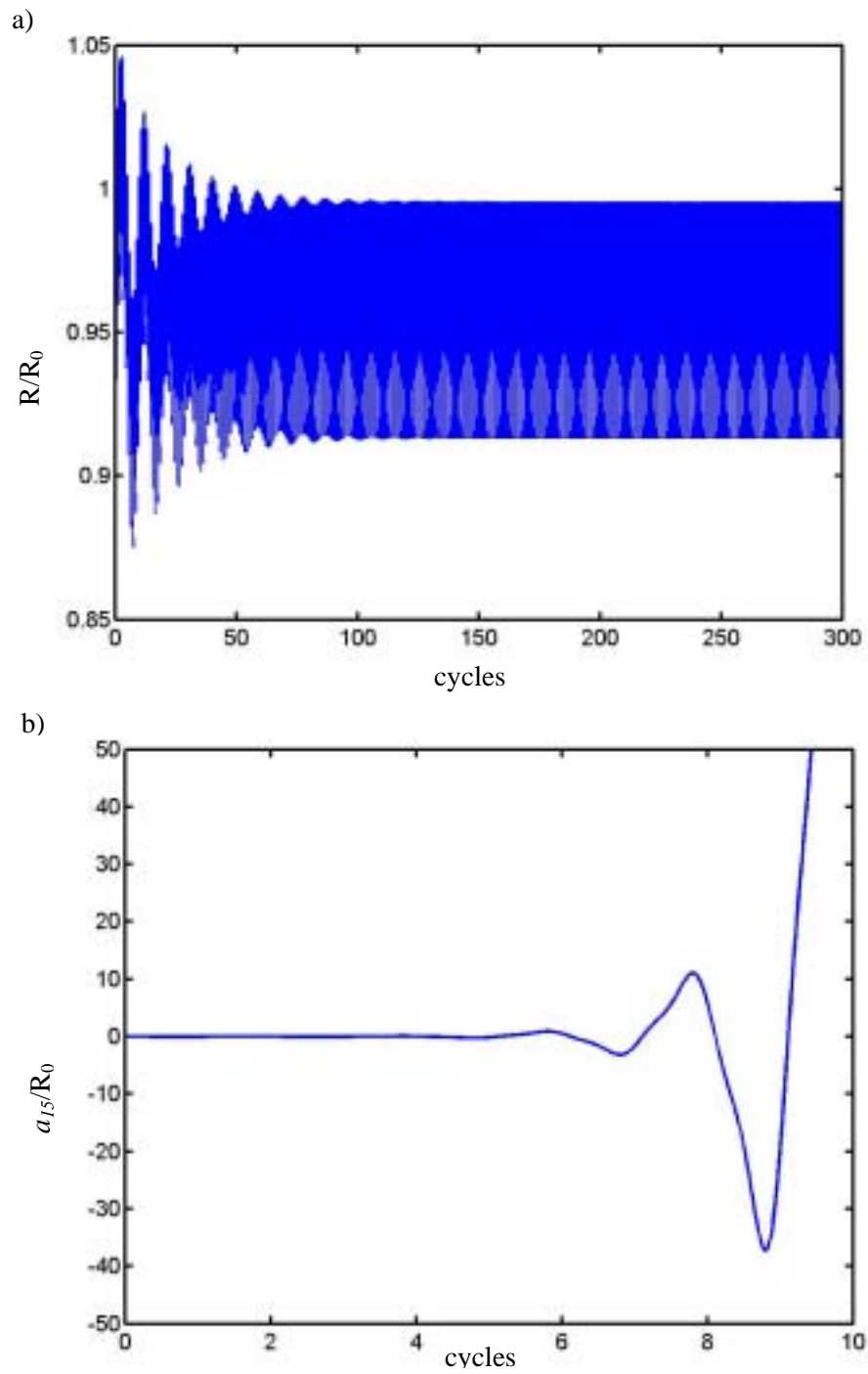
Figure 2.3 Typical *R(t)* and $a_{15}(t)$ curve for a big bubble. R_0=30 μm, μ=0.001 N.s/m^2 and p=1.5 MPa at 1 MHz
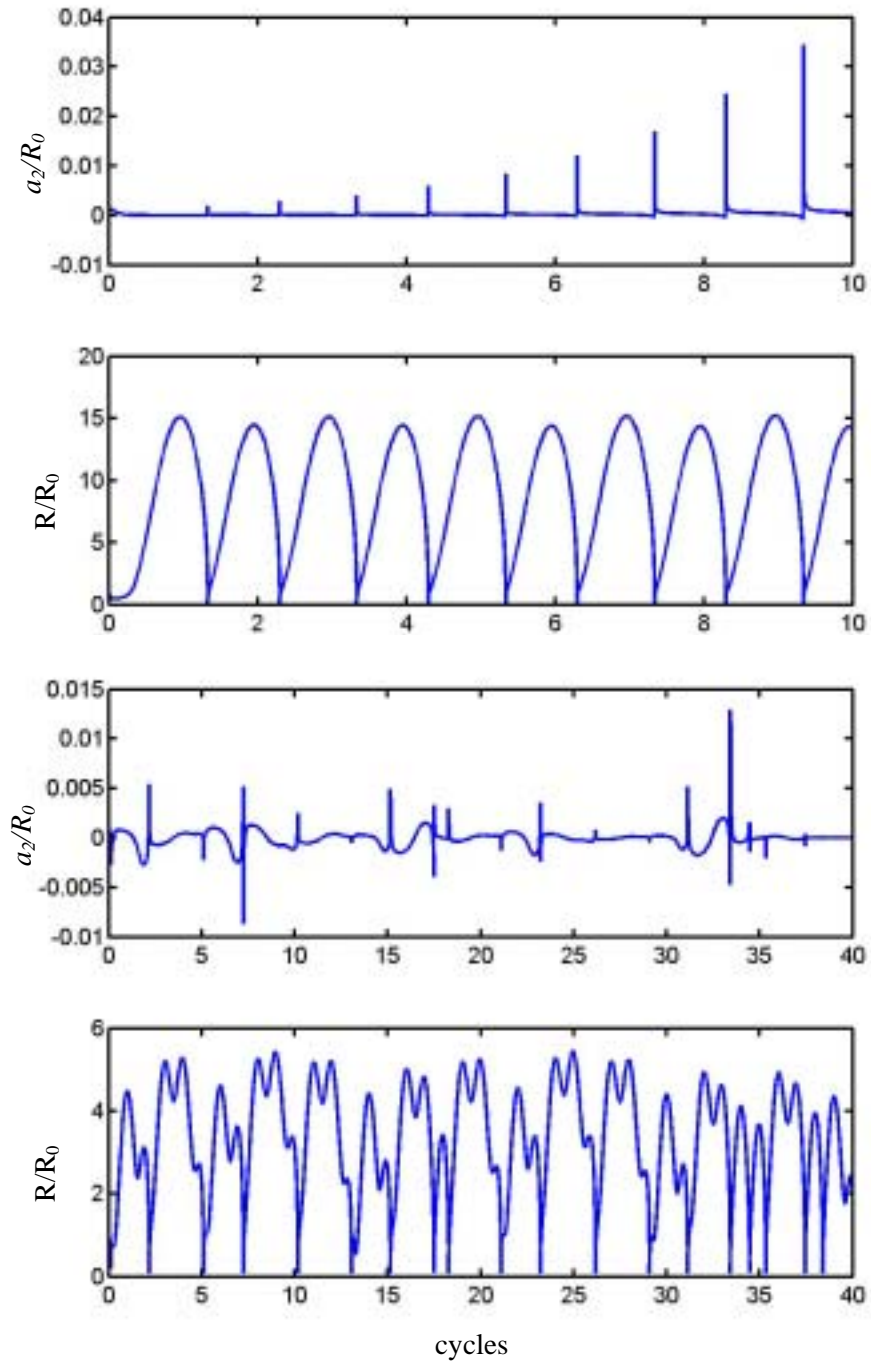
Figure 2.4 Examples of $R(t)$ and $a_2(t)$ curves for periodic and chaotic oscillating bubbles. P=2.0 MPa at 1 MHz. R_0=1 μm and μ=0.01 N.s/m^2 for the top two; R_0=4 μm and μ=0.06 N.s/m^2 for the bottom two.

a)

b)

cycles

45
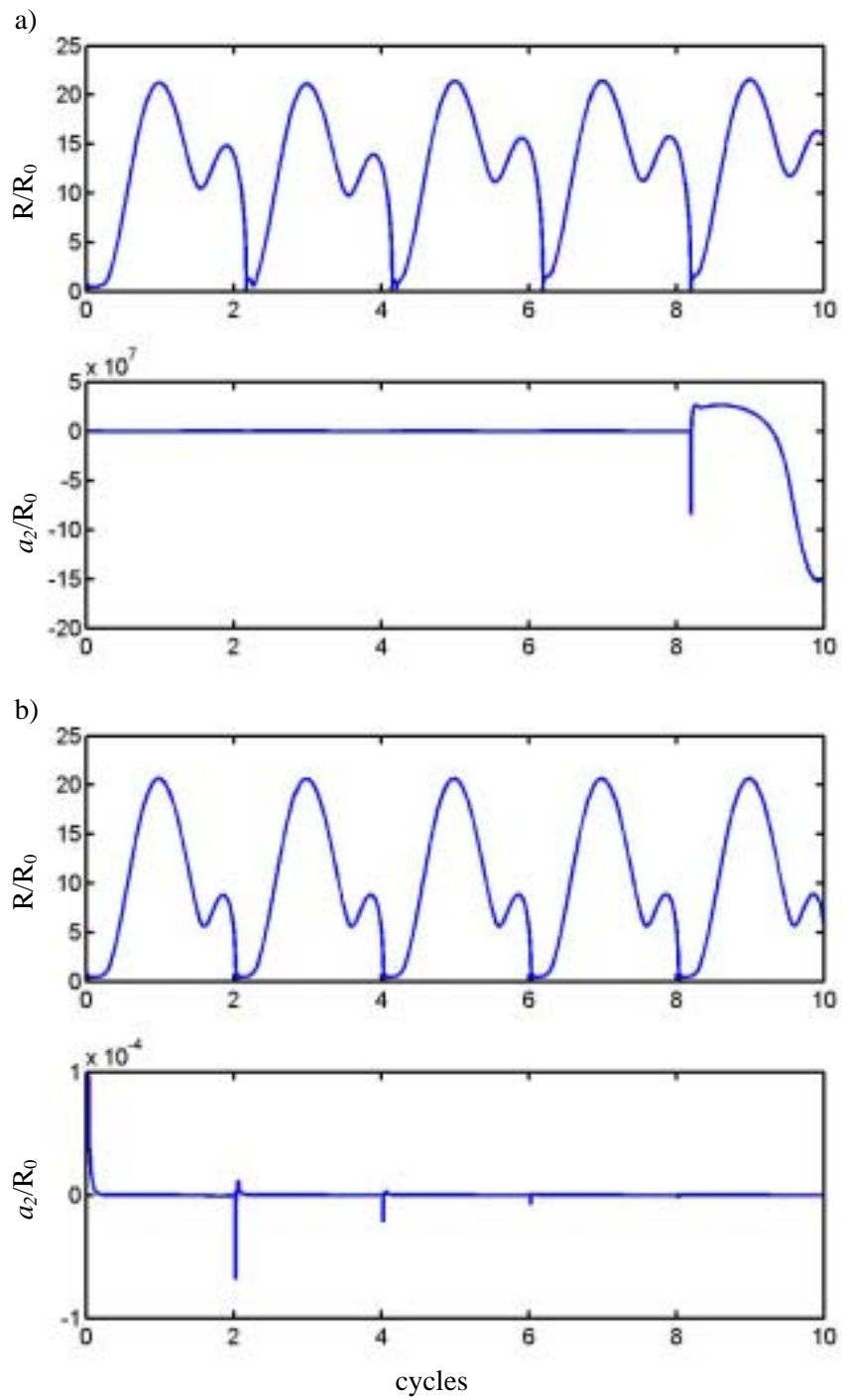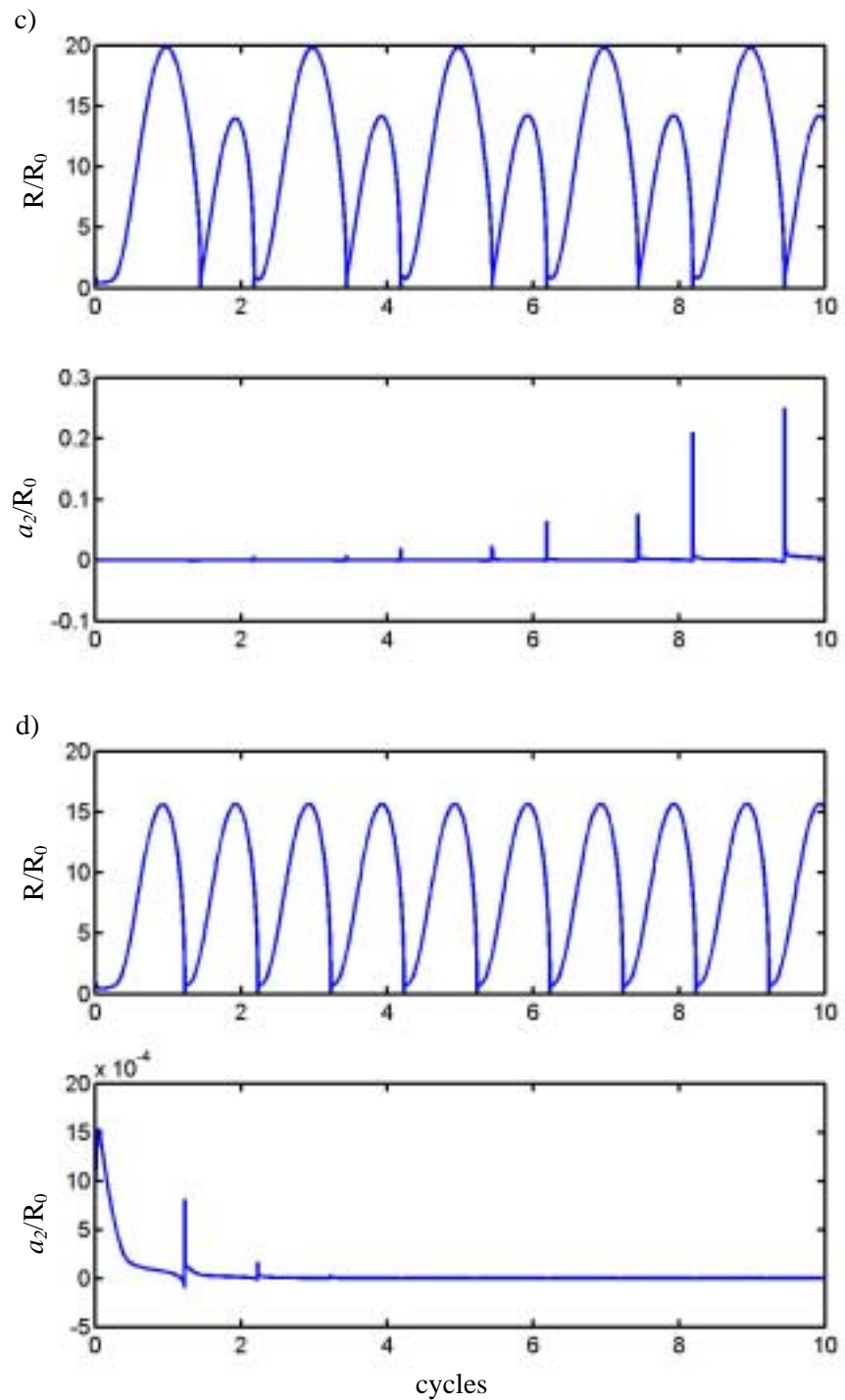
Figure 2.5 Examples of $R(t)$ and $a_2(t)$ curves for different viscosities at driving pressure 3 MPa and $R_0=1$ μm. a) 0.001 N.s/m^2; b) 0.004 N.s/m^2; c) 0.008 N.s/m^2; d) 0.03 N.s/m^2.
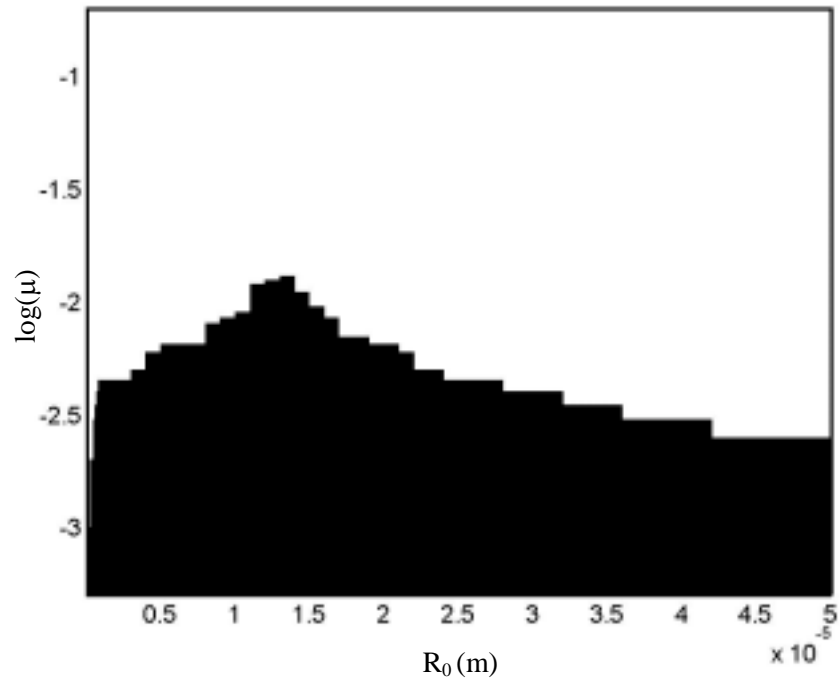
Figure 2.6a Shape instability region at driving pressure 1 MPa. The dark area is shape unstable region and the light region is shape stable region. The unit of μ is N.s/m^2.

47
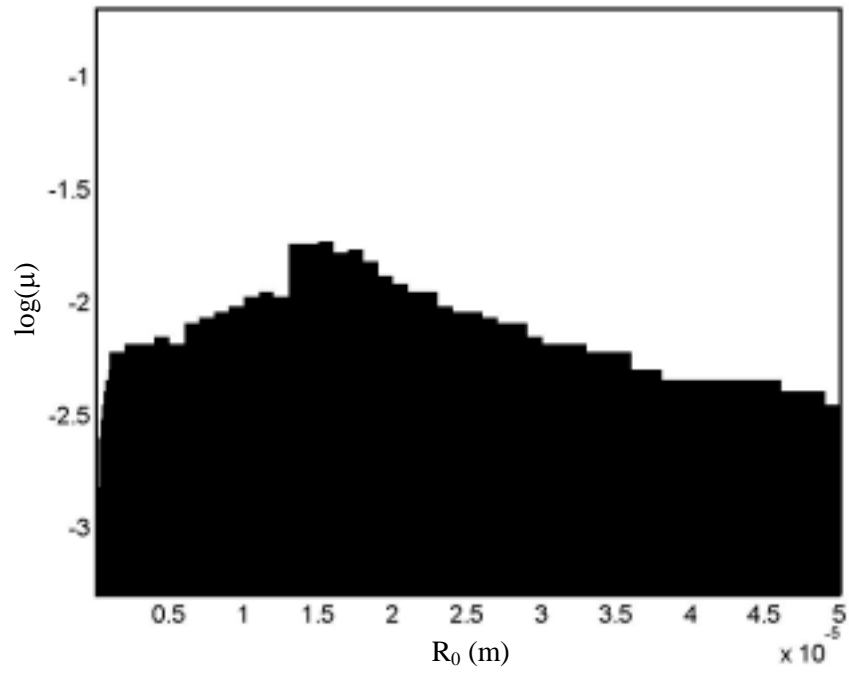
Figure 2.6b Shape instability region at driving pressure 1.5 MPa. The dark area is shape unstable region and the light region is shape stable region. The unit of μ is N.s/m^2.
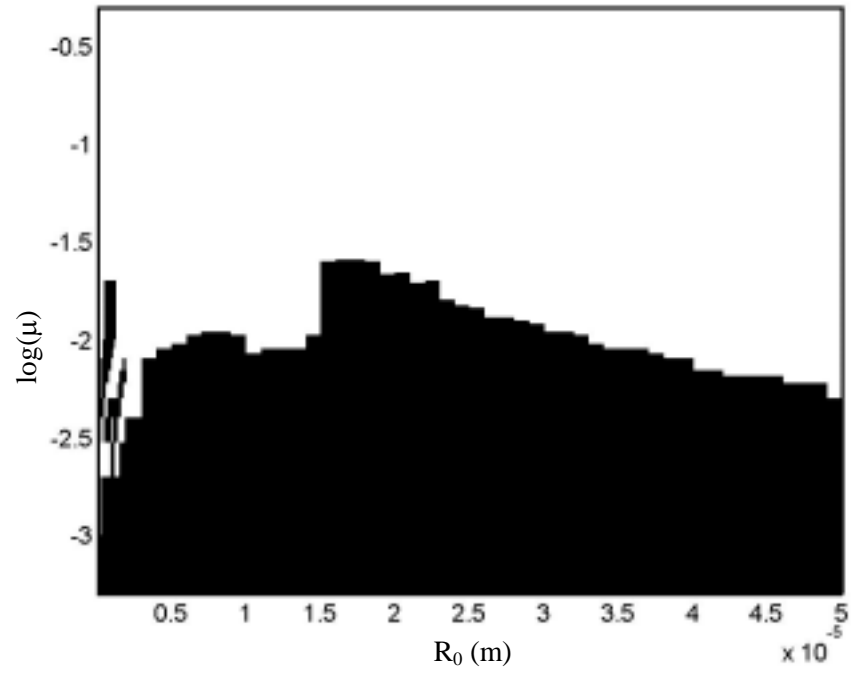
Figure 2.7a Shape instability region at 2 MPa and driving frequency 1 MHz. The dark area is shape unstable region and the light region is shape stable region. The unit of μ is N.s/m^2.
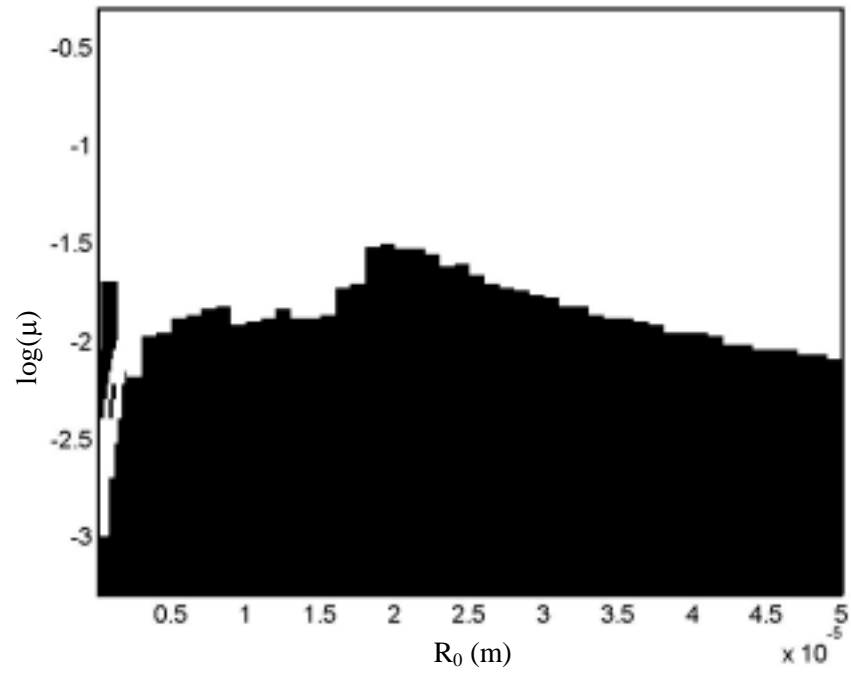
Figure 2.7b Shape instability region at 2.5 MPa and driving frequency 1 MHz. The dark area is shape unstable region and the light region is shape stable region. The unit of μ is N.s/m^2.
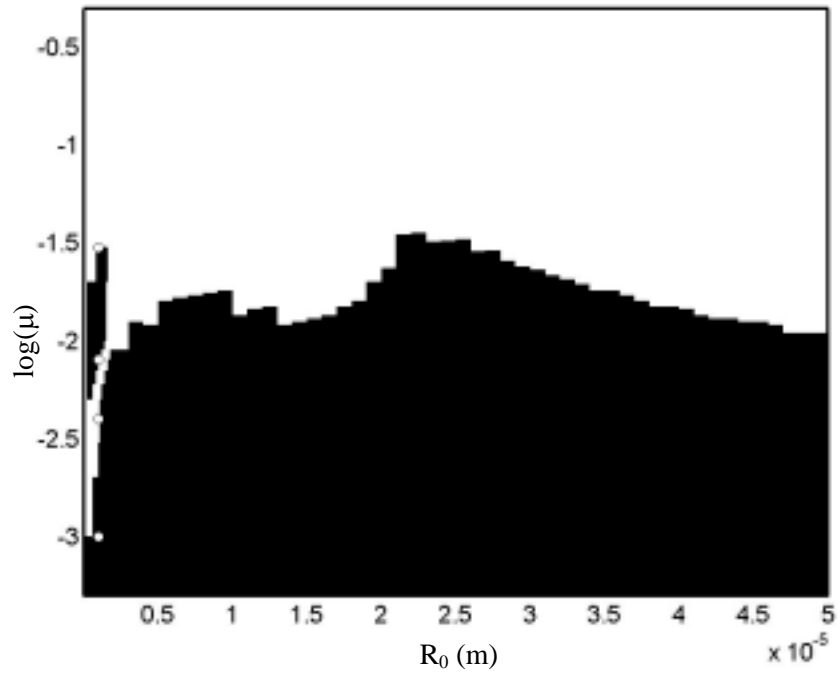
Figure 2.7c Shape instability region at 3 MPa and driving pressure 1 MHz. The four black dots represent the position of the $R(t)$ and $a_2(t)$ curve we showed in Figure 2.5. From bottom to top corresponding to a), b), c), and d) respectively. The dark area is shape unstable region and the light region is shape stable region. The unit of μ is N.s/m^2.
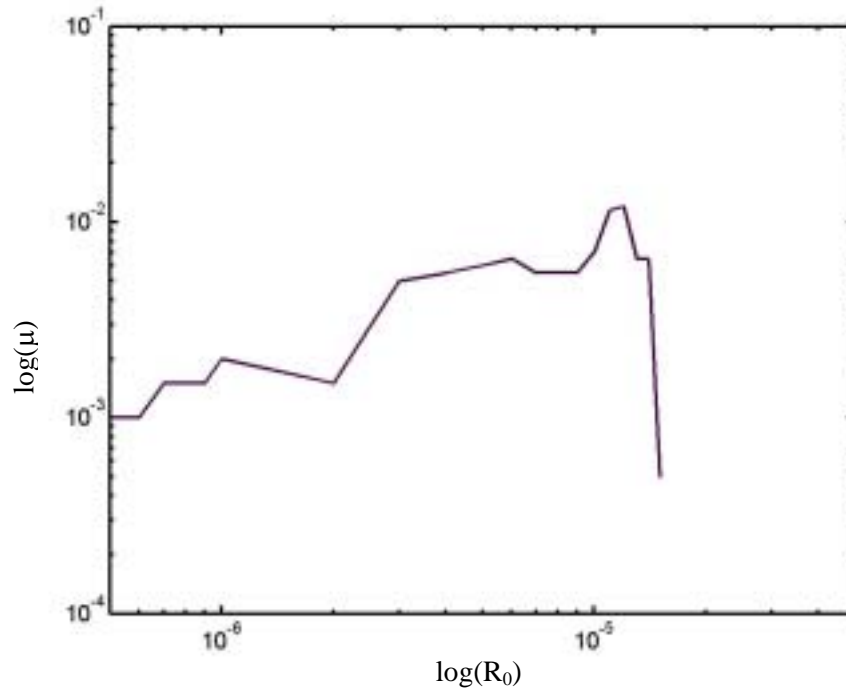
Figure 2.8 The shape instability threshold for mode 3 at 1 MPa. Above the threshold is shape stable region and below the threshold is shape unstable region. The unit of μ is $N.s/m^2$ and the unit of R_0 is m.
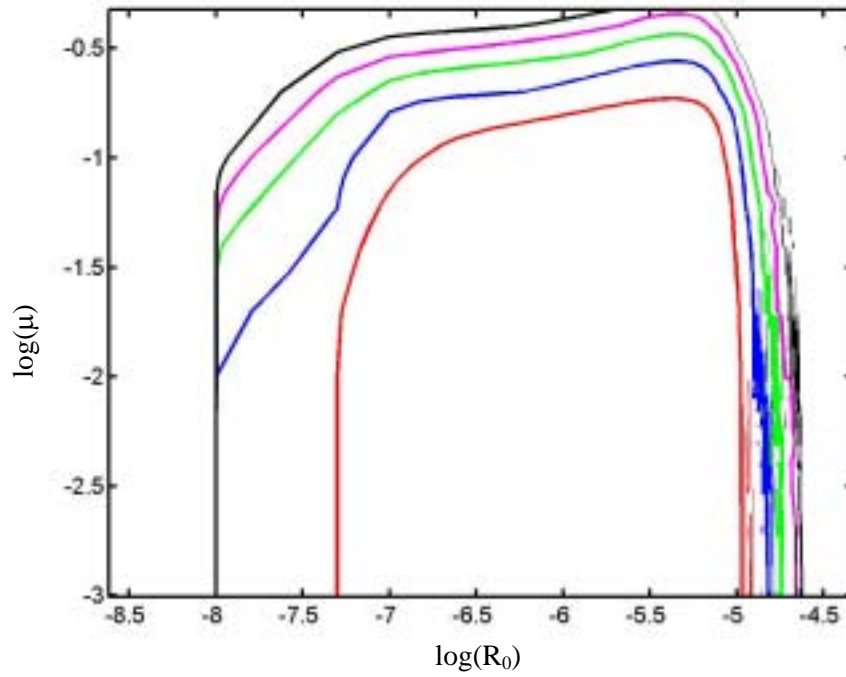
Figure 2.9 Rectified diffusion thresholds at 100% gas concentration sample for different driving pressures. f=1 MHz. From top to bottom, the driving pressures are 3.0 MPa, 2.5 MPa, 2.0 MPa, 1.5 MPa, and 1.0 MPa respectively. The unit of μ is N.s/m^2 and the unit of R_0 is m.
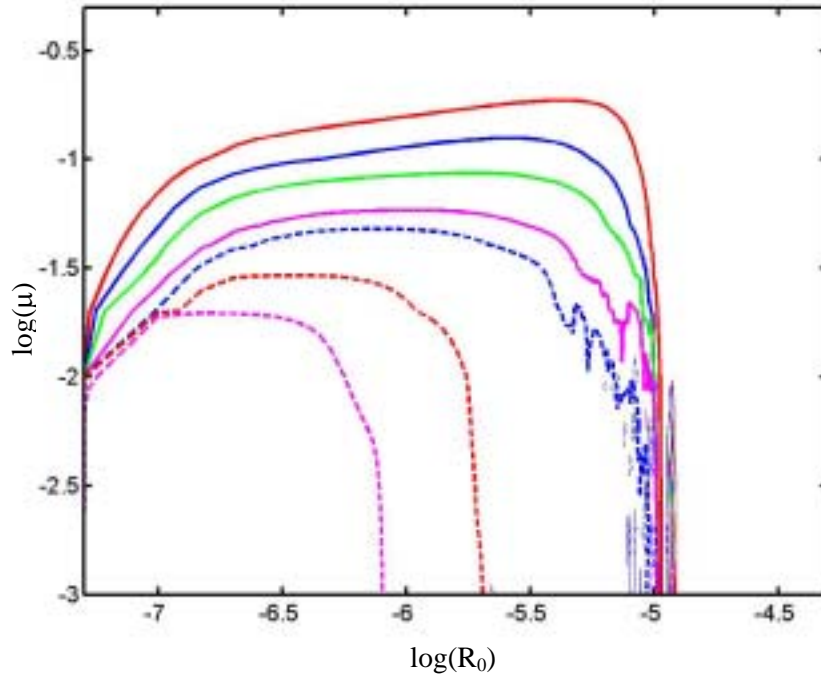
Figure 2.10 Rectified diffusion thresholds at1MPa for different gas concentrations. f=1 MHz. From top to bottom, c_i/c_0=1.0, 0.75, 0.5, 0.2, 0.1, 0.01, 0.001 respectively. The unit of μ is N.s/m^2 and the unit of R_0 is m.
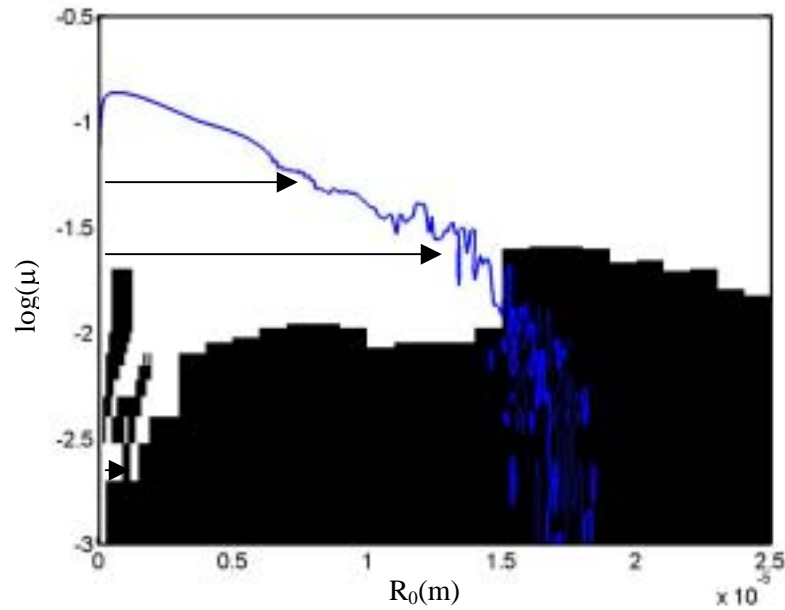
Figure 2.11 The overlap of the rectified diffusion threshold on the shape stability mapping at 2 MPa. Gas concentration c_i/c_0=10%. f=1 MHz. The dark region represents the shape unstable region and the light region is shape stable region. The line is the rectified diffusion threshold. The three arrows show three paths for bubbles to grow. From top to bottom, viscosities are 0.08 N.s/m^2, 0.02 N.s/m^2, and 0.002 N.s/m^2. The growth times are 1.11s, 3.45s, and 2.6e-11s respectively. All the bubbles start growing from 50 nm. The unit of μ is N.s/m^2.
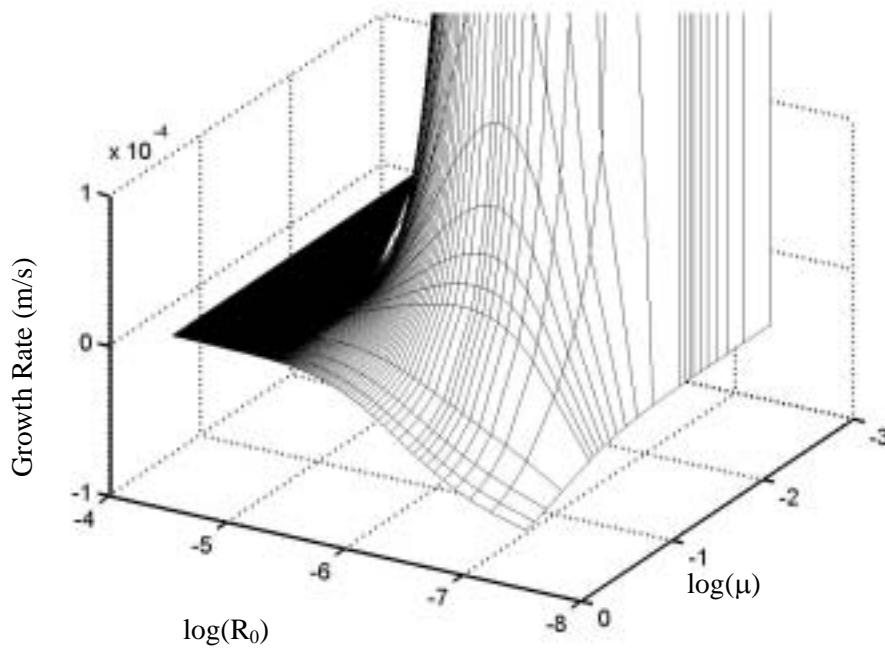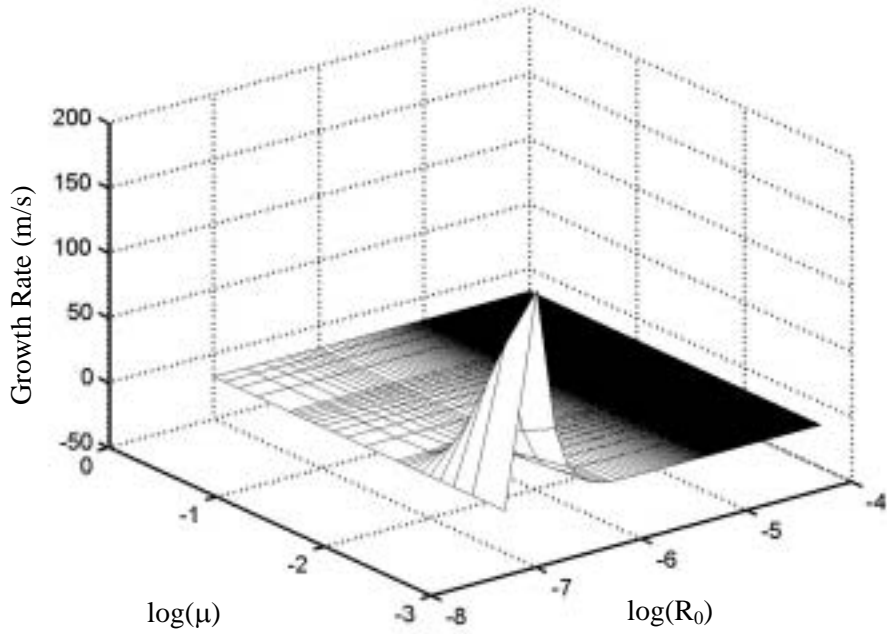
Figure 2.12a Bubble growth rate at 1 MPa and gas concentration 100%. The bottom plot shows details by zooming in the top plot. The unit of μ is N.s/m^2 and the unit of R_0 is m.
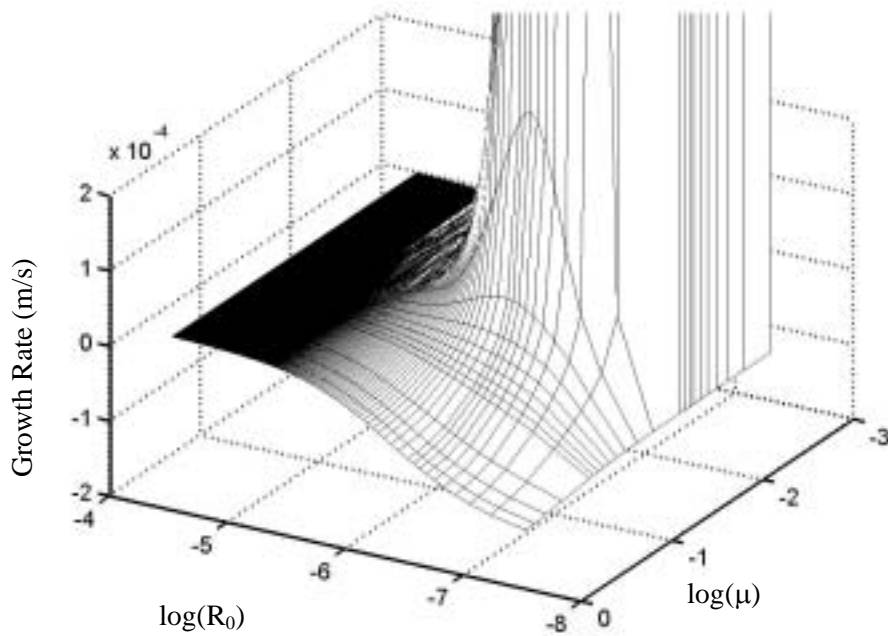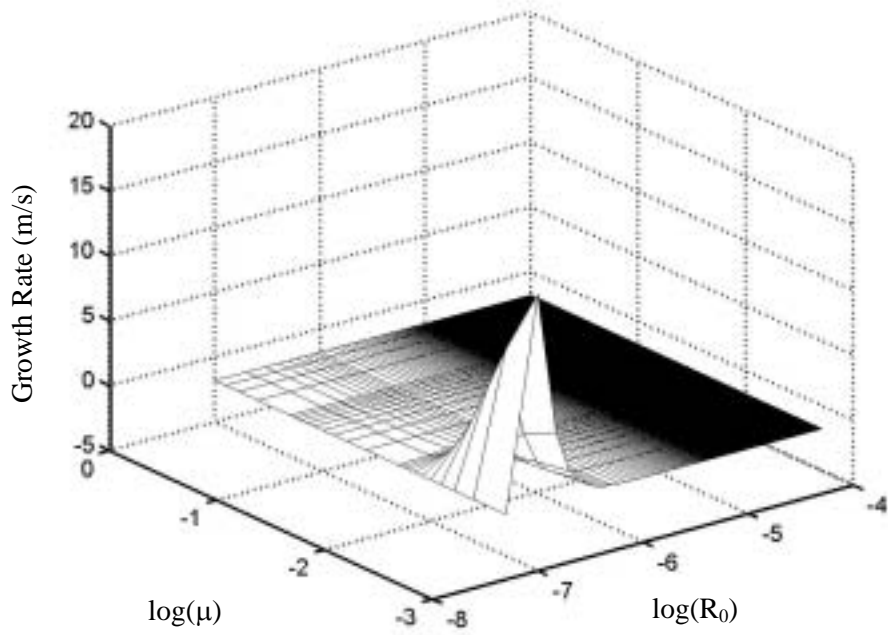
Figure 2.12b Bubble growth rate at 1 MPa and gas concentration 10%. The bottom plot shows details by zooming in the top plot. The unit of μ is N.s/m^2 and the unit of R_0 is m.
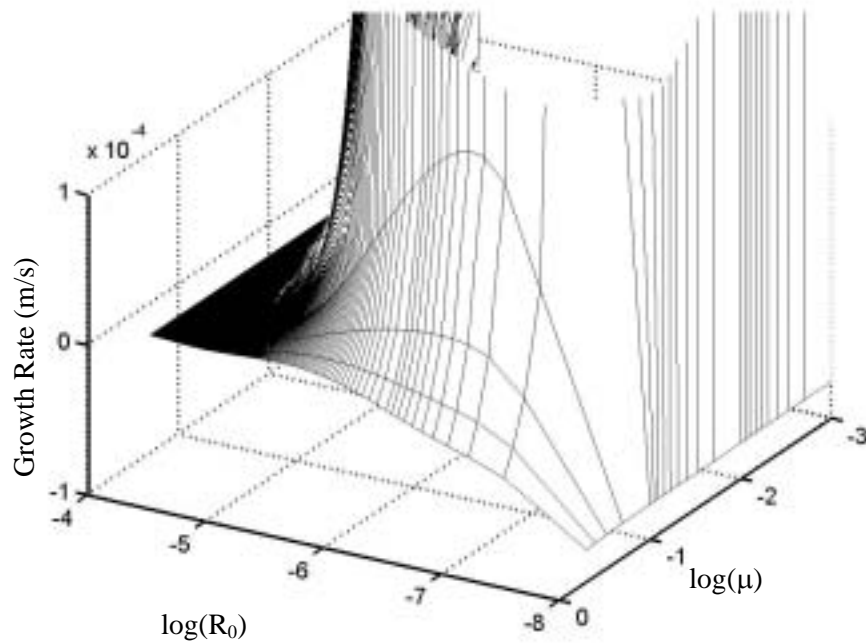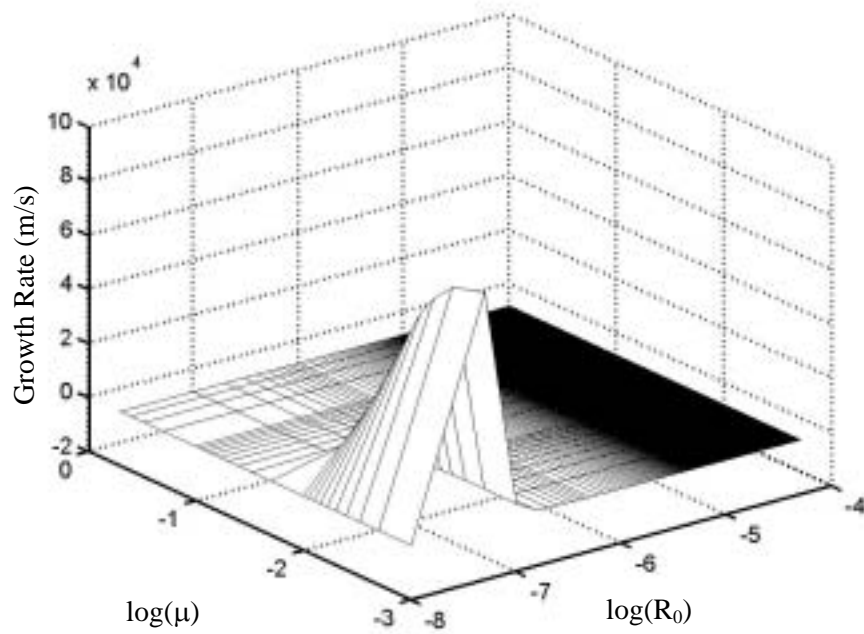
Figure 2.13 Bubble growth rate at 3 MPa. The gas concentration is 100%. The bottom plot shows details by zooming in the top plot. The unit of μ is N.s/m^2 and the unit of R_0 is m.
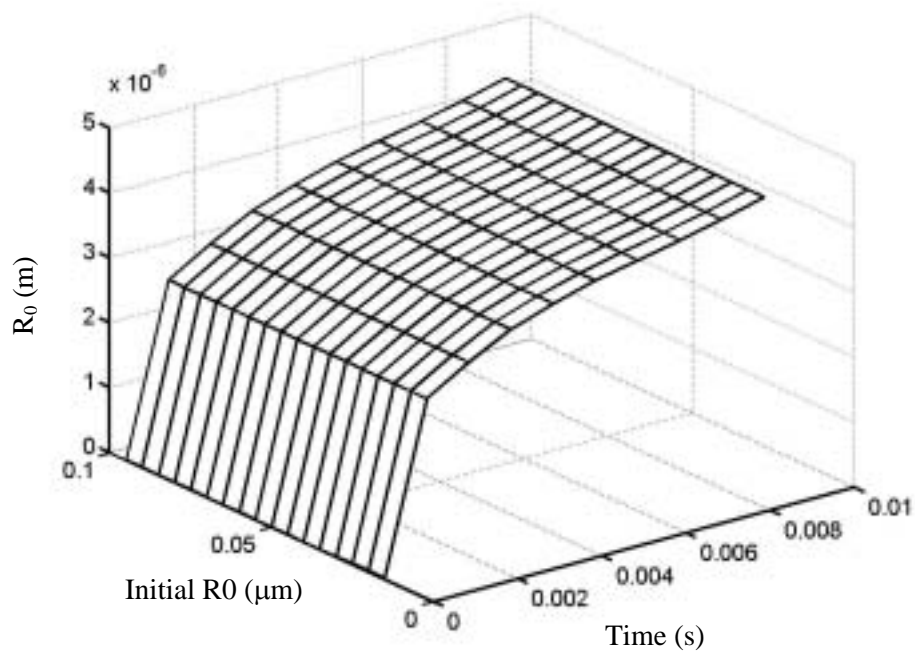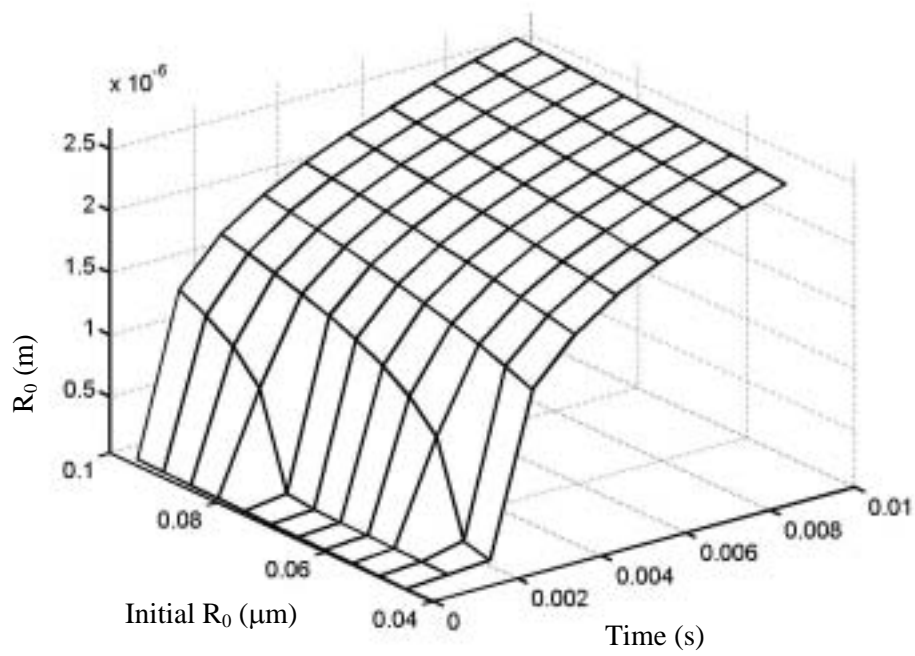
Figure 2.14 Bubble size evolutions at 2 MPa for different viscosities. a) (top) 0.05 N.s/m^2 and b) (bottom) 0.005 N.s/m^2 Dissolved gas concentration 20%.
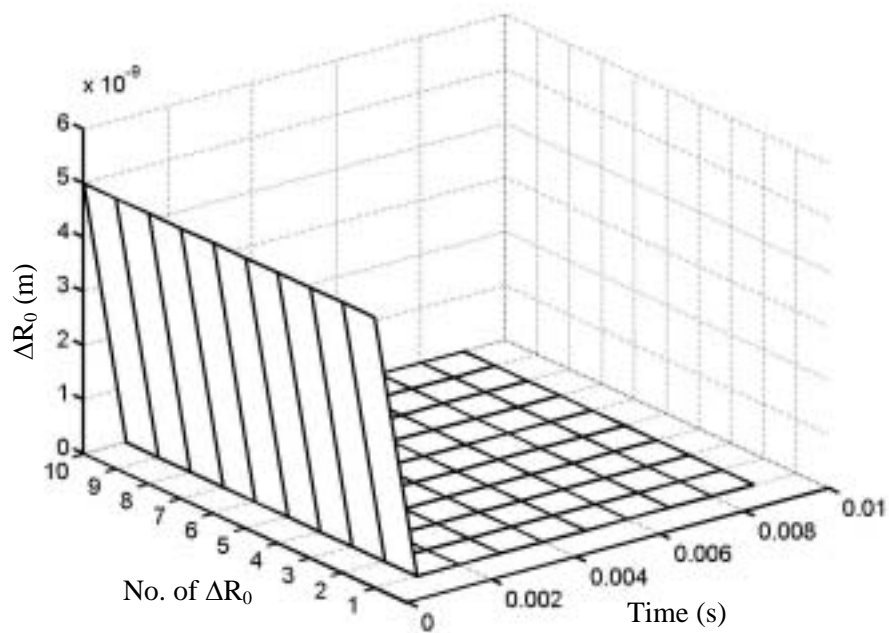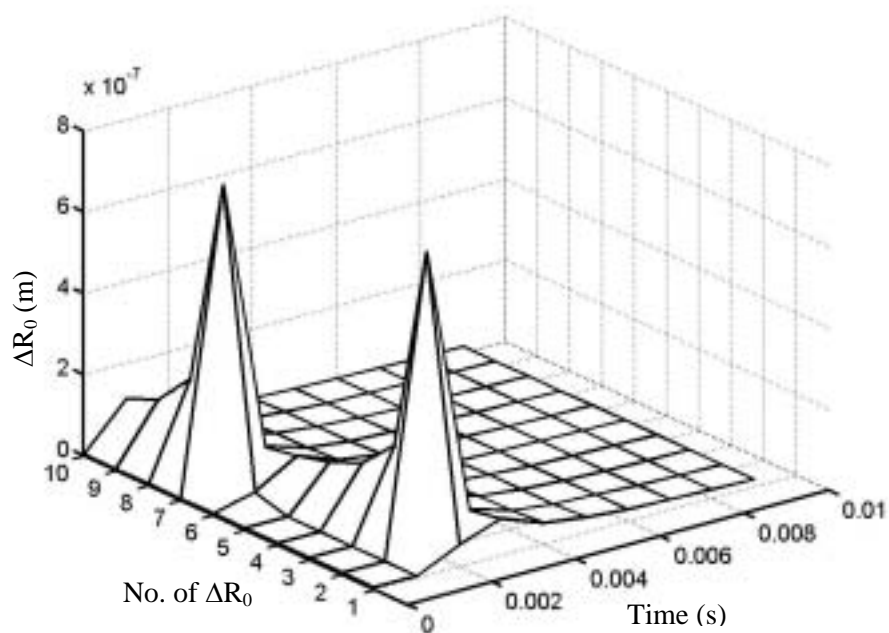
Figure 2.15 The evolution of the difference between bubble sizes. Here 11 bubbles are chosen initially, the R_0 are 45, 50, 55, 60, 65, 70, 75, 80, 85, 90, 95 nm. The first ΔR_0 indicates the difference between the 45 nm initial size bubble and 50 nm initial size bubble; and the second ΔR_0 indicates the difference between the 50 nm initial size bubble and 55 nm initial size bubble and so on and so forth for the No.3-10 of ΔR_0. Two viscosities are chosen: (top) 0.05 N.s/m^2 and (bottom) 0.005 N.s/m^2. The driving pressure is 2 MPa.

Chapter 3

Ultrasound Hyperthermia and theoretical model

The evaluation of temperature elevation during the ultrasonic insonation is very important in ultrasound therapy since the lesion is likely formed by thermal damage [7]. The purpose of this research is to investigate the heating behavior of ultrasound with the presence of cavitation, so an accurate temperature estimate is a key point in this work. In this chapter we will consider the heating of the tissue due to high intensity focused ultrasound. As the acoustic wave passes through an absorptive medium, energy will be dissipated. The conservation of energy is the basis of the heating theory. The energy propagating with the sound wave is deposited in the surrounding media and a temperature elevation is consequently induced. To quantify the thermal damage, effort in theory and experiment are both needed. In this chapter, we introduce the theoretical model we used in this work. We concentrate on high acoustic pressures where cavitation-enhanced heating plays a role. and analyze the heating related to cavitation phenomenon.

3.1 General consideration

For the purpose of this research, tissue-mimicking phantoms which lack blood vessels and non-acoustic sources of internal heat generation are considered in experiment and modeling. In general, the temperature prediction includes the heating and cooling effect. To accurately predict the heating effect, we need to know the details of the heating source. The cooling depends on the heat conduction of the medium itself and the initial temperature distribution. The

theoretical model is easy to apply to estimate heating if high intensity ultrasound is propagating in a homogenous medium. However, when cavitation occurs, the heating becomes much more complicated. The occurrence of cavitation in the tissue phantom can change the local material sound property and that actually makes the homogeneous medium inhomogeneous. The ultrasound energy will be re-distributed by the spatial distribution of the cavitation activity. In general, the presence of cavitation in a certain area can serve as a nearly perfect energy sink and enhance the local temperature very efficiently; and this may be very useful in ultrasound therapy. We will use our knowledge of single bubble dynamics, which we described in Chapter 2, to evaluate the heating source arising from cavitation.

3.2 Heating models

3.2.1 Linear heating

We start from a simple linear theory. The temperature change in a medium is going to follow the heat conduction equation, which has the form

$$\rho C \frac{\partial T}{\partial t} = K \nabla^2 T + Q \tag{3.1}$$

where ρ is the density of the medium, C the heat capacity, T the temperature, t the time, K thermal conductivity and Q is a heating source term. The first term in this equation accounts for thermal capacity and the second term accounts for thermal conductivity. The role of acoustic energy is to serve as a source term, which could be a temporal and spatial function. To obtain an analytical estimate, consider the simplified case of a wide sound beam and a low working intensity and short insonation time, so that the thermal conductivity in the radial direction can be ignored. Then the temperature gradient in the sound beam will be very small and can be ignored. Then the thermal conduction equation becomes

$$\rho C \frac{\partial T}{\partial t} \approx Q \tag{3.2}$$

Moreover, if the intensity of ultrasound is constant during the insonation, we can use a time-average of the heating source Q. Then the elevation of temperature will be

$$\Delta T \approx \frac{Q}{\rho C} \Delta t \tag{3.3}$$

In a sound field, the energy dissipation per unit volume is $Q=2\alpha I$, where α is the absorption coefficient and I is the local acoustic intensity. This method is called linear heating theory since the temperature rise is assumed linear here. If the temperature rise is measured, then the local absorption coefficient can be evaluated by this result. Fry and Fry [96][97] first used this result to infer the absorption coefficient of a medium.

3.2.2 The effect of conduction

In reality, people often use a focused narrow sound beam to achieve high intensity and then high temperature elevation in desired area; in this case the linear heating theory does not give a good estimate any longer, and heat conduction must be taken into account. By adopting the solution for an infinite line source which is given by Lele [98], Parker [99] was able to develop an analytic formulation to describe the temperature after a short pulse, which assumes a Gaussian distribution of the temperature field after a short insonation:

$$T(r) = T_0 e^{-r^2/\beta} \tag{3.4}$$

where β is a measure of the Gaussian distribution of the sound beam and T_0 is the peak temperature at r=0. Following this temperature field, the cooling can be modeled as

$$T(r,t) = \frac{T_0}{4Dt/\beta + 1} e^{-r^2/(4Dt+\beta)} \tag{3.5}$$

If axial conduction is taken into account [100], then the solution is modified as

$$T(r,t) = \frac{T_0}{4Dt/\beta + 1} e^{-r^2/(4Dt+\beta)} erf\left(\frac{z}{4Dt}\right) \tag{3.6}$$

where D is the thermal diffusivity and $erf(\cdot)$ stands for the normal error function. If the sound intensity on axis is maintained at a constant value of I_0 for a long duration, the observed temperature can therefore be expressed as the convolution of the impulse response of the system with a step input

$$T(r,t) = \int_0^t \frac{2\alpha I(r)}{\rho C[1 + (4D\tau/\beta)]} d\tau \tag{3.7}$$

At r=0, evaluating the convolution integral yields:

$$T(t) = \frac{2\alpha I_0}{\rho C}\left(\frac{\beta}{4D}\right)\ln\left(1 + \frac{4Dt}{\beta}\right) \tag{3.8}$$

then for short durations, $4Dt/\beta<<1$, this result reduces to the linear heating result.

These results have been shown by Parker to provide suitable estimates given the assumptions specified in the derivation. However, Parker's purpose in developing these equations was to infer the absorption in media, and his assumption that the temperature field has a Gaussian shape identical to the beam intensity is only true at low intensity. For our high intensity focused ultrasound source, the resulting temperature field is very likely to have a Gaussian shape, but the Gaussian variance β could be larger than that of the acoustic intensity due to strong radial conduction; Parker's solution will overestimate the temperature rise, as shown in Figure 3.1.

3.2.3 Bioheat Transfer Equation

A more complete and accurate model for the temperature field is Pennes bioheat transfer equation (BHTE) [12], which has the following form

$$\rho C \frac{\partial T}{\partial t} = K\nabla^2 T - w_b C_b (T - T_\infty) + Q \tag{3.9}$$

where the subscript b refers to the blood domain and w_b is the perfusion rate. This model is also a linear model and, with Q determined, this equation is easily solved by numerical methods and can give us more accurate results. In Figure 3.1, the comparisons between different models are shown. At the beginning of the heating, all three models agree very well. As the insonation time increases, conduction starts to play a role and the linear heating model starts to overestimate the temperature. Parker's heating model follows the numerical result of the BHTE very well, but eventually overestimates temperature too. We expect this discrepancy between models will increase as the temperature increases since conduction will play a much more important role for those cases.

In this work, only hyperthermia in soft tissues is simulated, and no blood vessels considered; the BHTE is simplified to

$$\rho C \frac{\partial T}{\partial t} = K \nabla^2 T + Q ,$$

(3.10)

which is of course the heat conduction, or diffusion equation

Source term in BHTE

In a homogenous tissue phantom, the problem of hyperthermia is reduced to a problem of determining the heating source term Q. In a sound field, the energy deposition per unit volume is equal to the energy loss of the acoustic propagation which can be modeled as [1]

$$Q = \frac{2\alpha}{\rho c \omega^2} \left(\frac{\partial p}{\partial t} \right)^2$$

(3.11)

where c is the sound speed in the medium, p is the acoustic pressure and ω is the driving frequency. Using this heating source gives a very good estimate for the temperature rise in the tissue phantom in general.

In reality, however, the acoustic pressure is not always easy to get. At low driving pressure, the acoustic field can be obtained through solving the wave equation (which will be discussed later). As the driving pressure exceeds a certain threshold value, cavitation will occur in the tissue phantom; then the local acoustic pressure can not be obtained by solving the homogeneous medium wave equation. The heating mechanisms due to cavitation have to be considered. Owing to the randomness of the occurrence of cavitation and the strong nonlinearity of bubble oscillations, to find a proper heating source Q becomes a very complicated problem. To accurately model this heating problem, then, we must implement the knowledge gained about HIFU bubble dynamics in Chapter 2.

3.3 Solving for the primary pressure field

We are going to start from a low intensity problem, which means the pressure field can be obtained through solving the wave equation. We chose to numerically solve the Westervelt equation [101][102] to get the primary sound field and the primary heating source term Q. A finite differential time domain (FDTD) code to solve the Westervelt equation has been developed by Hallaj [103] and used in previous work [48][13]. The primary disadvantage of the FDTD code is that it can only account for thermoviscous absorption, which means the absorption coefficient α is proportional to f^2. In many real tissues, the absorption coefficient α is proportional to $f^{1.1}$, as is the case in our tissue phantom. The argument we make here is that throughout our whole parameter space, the energy dissipated by the second harmonic component arising due to the nonlinearity of the tissue phantom is at the order of 1% of that of the fundamental component, thus the error due to the different absorption law will be limited to a very small value (See Appendix B).

The Westervelt equation has the form

$$\left(\nabla^2 - \frac{1}{c^2}\frac{\partial^2}{\partial t^2}\right)p - \frac{2\alpha}{c\omega^2}\frac{\partial^3 p}{\partial t^3} + \frac{\beta}{\rho c^4}\frac{\partial^2 p^2}{\partial t^2} = 0, \tag{3.12}$$

where β is the local coefficient of nonlinearity and $\beta=1+B/2A$ with B/A being the nonlinear parameter of the medium [104]. All other symbols are as defined above. The first term in the left-hand side is the D'Alembertian operator present in all wave equations. The first term inside the parenthesis accounts for diffraction in space and the second represents the propagation of the wave in time. The second term on the left-hand side represents the thermoviscous loss during the propagation of the wave. The third term is the nonlinear term accounting for wave distortion and the generation of higher harmonics during the propagation. Since 1) the HIFU source we used in the experiments is an axially symmetric transducer; 2) our tissue phantom is cylindrically symmetric; and 3) all the boundary conditions are cylindrically symmetric, a 2-dimensional form of the Westervelt equation will be used throughout this work. In a cylindrical coordinate frame, the Westervelt equation has the form,

$$\frac{\partial^2 p}{\partial r^2} + \frac{1}{r}\frac{\partial p}{\partial r} + \frac{\partial^2 p}{\partial z^2} - \frac{1}{c^2}\frac{\partial^2 p}{\partial t^2} + \frac{2\alpha}{c\omega^2}\frac{\partial^3 p}{\partial t^3} + \frac{\beta}{\rho c^4}\frac{\partial^2 p^2}{\partial t^2} = 0, \tag{3.13}$$

where r is the radial location and z is the axial location. The acoustic axis is set as the z-axis. The implementation of the numerical solution is based directly on the code developed by Hallaj. The desired solution domain is divided into a discrete grid in time and space, where $p_{i,j}^n$ represents the pressure at location (i, j) and time step n. The mapping to the spatial location and time from these indices is

$$z_i = (i-1)dz, \quad r_j = (j-1)dr, \quad t_n = (n-1)dt, \tag{3.14}$$

where dz, dr and dt represent the grid step in space and time respectively. The difference equations used are accurate to second order in space and time:

$$\frac{\partial p}{\partial r} = \frac{1}{2dr}\left(p_{i,j+1}^{n} - p_{i,j-1}^{n}\right),$$

$$\frac{\partial^2 p}{\partial r^2} = \frac{1}{dr^2}\left(p_{i,j+1}^{n} - 2p_{i,j}^{n} + p_{i,j-1}^{n}\right),$$

$$\frac{\partial^2 p}{\partial z^2} = \frac{1}{dz^2}\left(p_{i+1,j}^{n} - 2p_{i,j}^{n} + p_{i-1,j}^{n}\right),$$

$$\frac{\partial p}{\partial t} = \frac{1}{2dt}\left(3p_{i,j}^{n} - 4p_{i,j}^{n-1} + p_{i,j}^{n-2}\right), \tag{3.15}$$

$$\frac{\partial^2 p}{\partial t^2} = \frac{1}{dt^2}\left(p_{i,j}^{n+1} - 2p_{i,j}^{n} + p_{i,j}^{n-1}\right),$$

$$\frac{\partial^3 p}{\partial t^3} = \frac{1}{2dt^3}\left(6p_{i,j}^{n} - 23p_{i,j}^{n-1} + 34p_{i,j}^{n-2} - 24p_{i,j}^{n-3} - 8p_{i,j}^{n-4} - p_{i,j}^{n-5}\right),$$

At the beginning of the iteration, a backward formulation is used for the time derivative,

$$\frac{\partial^2 p}{\partial t^2} = \frac{1}{dt^2}\left(2p_{i,j}^{n} - 5p_{i,j}^{n-1} + 4p_{i,j}^{n-2} - p_{i,j}^{n-3}\right) \tag{3.16}$$

For the explicit method only one unknown term, representing the future pressure value, is permissible. The second time derivative in the D'Alembertian in the wave equation is chosen because the numerical solution was found to behave best in the original implementation [103].

3.3.1 Solution domain

A typical example of the geometry of the spatial domain for the simulation in this work is shown in Figure 3.2. It represents a cross section along the axial and radial axes, and the whole area is symmetric about the z-axis, so only half of the cross section is shown here. The shaded area at the right side represents the tissue phantom, which has a cylindrical shape with a flat surface facing the transducer. The arc at the left side represents the surface of transducer. In this case, it simulates our HIFU transducer, which has a spherical surface, and the center of the sphere located inside the tissue phantom, is indicated by a square dot. The HIFU transducer used in experiments has an active aperture of 70 mm and radius of curvature of 62.6mm. The remaining portion of the domain is modeled as water.

In this work, a 1-second continuous wave (CW) tone burst is used as the insonation signal in experiments. It takes only about three cycles for the HIFU transducer to reach steady-state; therefore, we can just use the solution for steady-state for this 1-second CW insonation, in which 10^6 cycles are included. We simulate the acoustic field for 100 μs, which is enough to allow the sound field to reach steady state at desired region. To suppress the numerical error, the acoustic energy dissipation is calculated in last 10 cycles and cycle-average values used in the temperature simulation. The solution domain should be large enough to avoid reflection from the edges of the computational domain, which is an artifact introduced by numerical simulation. Appropriate boundary conditions need to be applied at the computational domain edges, and will be discussed later.

3.3.2 Spatial grids and time steps

An accurate representation of a sinusoidal waveform generally requires a minimum of 10-12 spatial points per wavelength. For a source of frequency 1MHz and a sound speed of 1500m/s, the wavelength is 1.5 mm, therefore, a spatial grid which does not see substantial harmonic generation during propagation should be no greater than 0.15 mm. We will use a grid separation of 0.1mm. The maximum time step for which the stability of the solution is assured, is a function of the spatial grid and the speed of sound for wave propagation. A time step of 1×10^{-8} s is used in our simulation, which has been shown small enough to assure the stability of the solution.

3.3.3 Initial and boundary conditions

The initial condition in all simulations is a pressure value of zero everywhere. This is not required, however, and with proper saving of variables, a simulation could be resumed using

previous results. At the axis of symmetry, the boundary condition for cylindrical symmetry is used, which is,

$$\frac{\partial p}{\partial r} = 0 \tag{3.17}$$

At the transducer surface, a sinusoidal pressure wave is used to simulate the HIFU source. At all other surfaces, an absorption boundary condition (ABC) is imposed, and the simulations approximate the behavior of waves in infinite media. Lower order ABC's are relatively easy to implement. We employ Mur's well-known method that applies a radiation condition

$$\begin{aligned}
\frac{\partial p}{\partial r} - \frac{1}{c}\frac{\partial p}{\partial t} &= 0, \\
\frac{\partial p}{\partial z} - \frac{1}{c}\frac{\partial p}{\partial t} &= 0.
\end{aligned} \tag{3.18}$$

As a matter of fact, the focused nature of the source means the reflections are only a concern at the far boundary. By using ABCs, most of the energy reaching the boundary is dissipated numerically rather than reflected.

3.4 Heating source

3.4.1 Heating source due to the primary acoustic field

Now back to the main goal of this work: evaluating the temperature rise inside the tissue phantom. Solution of the primary acoustic field will allow us to evaluate the energy deposition from the sound field. Using the equation (3.11) with the current simulation grid, the heating source from the primary acoustic field is,

$$Q = \frac{2\alpha_{i,j}}{\rho_{i,j}c_{i,j}\omega^2 N}\left(\frac{1}{2dt}\right)^2 \sum_{n=1}^{N}\left(3p_{i,j}^n - 4p_{i,j}^{n-1} + p_{i,j}^{n-2}\right)^2, \tag{3.19}$$

where N is the number of time steps averaged.

3.4.2 Heating source due to cavitation

The preceding heating mechanism can give us very good estimates only at low intensity. Once the pressure increases to a certain critical value, cavitation is going to occur, and the heating source is going to become very complicated. Now, we are trying to evaluate the bubble-enhanced heating. Bubbles can enhance heating through several ways, such as viscous heating, scattering and radiation heating as we have discussed previously. In this work, we use a single-bubble model and focus on the damping mechanisms of single oscillating bubbles [72][105]. We assume that bubbles will not interact with other.

For an individual bubble, the heat deposition is equivalent to damping. Therefore we need to investigate the damping mechanisms of a single bubble. The damping for a single bubble has three aspects: viscous damping, radiation damping and thermal damping.

Viscous damping heating

Power deposition through viscous dissipation is actually a result of the interaction between the bubble wall and the surrounding medium. As a bubble oscillates, it has to push the surrounding liquid back and forth, and this will dissipate energy. The stress at an oscillating bubble wall due to the viscosity of the surrounding liquid has the form,

$$p_{vis} = \frac{4\mu\dot{R}}{R} \tag{3.20}$$

This stress acts over the whole bubble surface $4\pi R^2$, therefore, $p_{vis} \times 4\pi R^2$ represents the viscous force on the bubble surface. From simple dynamics, the power dissipated by viscous damping is equal to force times velocity. This yields [72]

$$W_{vis} = 16\pi\mu R\dot{R}^2 \tag{3.21}$$

This energy is dissipated solely as heat in the medium, and so this term is identically the viscous heating contribution. For a 1-second insonation, we use the time-averaged $R(t)$ to obtain this term. For linear oscillations in water, Prosperetti [72] showed the viscous damping will be important at higher frequencies, i.e., those in the megahertz range. In our current parameter space, since the viscosity of water only matches the lower limit, we expect that viscous heating could contribute a large fraction of the total effect.

Heating due to bubble acoustic radiation

Acoustic emission from an oscillating bubble consists of two parts: 1) the passive emission, which is only due to the presence of the object. For a micron-size bubble, the acoustic wavelength is much larger than the object (bubble), therefore, according to Rayleigh's scattering theory, only a very small amount of energy will be taken out of the sound wave by this passive emission; 2) the active emission. An oscillating bubble is actually a volume oscillator, which can be modeled as a monopole. The strength of this emission is therefore related to the volume changes. The acoustic emission from a volume oscillator has the following form in the far field,

$$p_{sac}(r,t) = \frac{\rho}{4\pi r}\frac{d^2 V}{dt^2}, \tag{3.22}$$

where r is the radial distance from the oscillator, and V is the volume of the oscillator. For an oscillating spherical bubble, this equation is readily rewritten as,

$$p_{sac}(r,t) = \frac{\rho R}{r}\left(2\dot{R}^2 + R\ddot{R}\right), \tag{3.23}$$

where R is the radius of the oscillating bubble. The time-averaged acoustic intensity can be written as

$$I_{sac}(r) = \frac{\left\langle p_{sac}^2(r,t)\right\rangle_t}{\rho c}, \tag{3.24}$$

$<\ >_t$ indicates the time-averaged quantity. The far field approximation holds for *1/kr<<1*, where *k* is the wave number. The far field limit certainly holds when the detected sound energy is a few cm away from the bubble. However, the limit may be violated when we need to determine the energy density of emitted sound near the bubble surface. In this case, a localized correction term is needed to correct this effect, and the scattered pressure becomes

$$p_{sac}(r,t) = \frac{\rho R}{r}\left(2\dot{R}^2 + R\ddot{R} + \frac{c}{r}R\dot{R}\right),$$ (3.25)

Fortunately, it has been shown by Hilgenfeldt *et al* [45][46] that the localized correction term to the emission of sound decays very rapidly, and even at distances as small as 1 μm from the bubble, the contribution from the correction term is small. Therefore, we will drop the correction term in the simulation. In general, compared to the active emission, the energy loss through the passive emission is negligible and will be omitted in this work.

Viscous heating is a local effect, and only the medium next to bubble surface can absorb the energy. The absorption of the radiated sound, however, is different. The sound emitted by a single bubble will propagate in the medium and be attenuated by the absorption of the medium. The absorption coefficient determines the volume which will be affected by the radiated sound. Therefore the energy deposition due to the acoustic radiation is a function of distance and absorption coefficients. In a lossy medium, the radiated pressure is written as

$$p_{sac}(r,t) = \frac{\rho R}{r}\left(2\dot{R}^2 + R\ddot{R}\right)e^{-\alpha_f r},$$ (3.26)

where the subscript *f* indicates the absorption coefficient α is frequency dependent. Then, at a certain distance *r*, the total emitted sound power is

$$\begin{aligned} E_{sac} &= 4\pi r^2 I \\ &= \frac{4\pi r^2}{\rho c}\int_0^{+\infty} p^2_{sac}(t)dt = \frac{4\pi r^2}{\rho c}\int_{-\infty}^{+\infty} p^2_{sac}(f)df \end{aligned}$$ (3.27)

where $p_{sac}(f)$ is the Fourier transform of $p_{sac}(t)$. If at the bubble surface, the emitted sound power is E_0, then the power deposition in the volume bounded by r is E_0-E_{sac}.

Thermal contributions to the heating

Another damping mechanism which may affect the heating is the thermal damping, or heat conduction. For an inertial bubble, the internal temperature may easily reach several thousand K when bubble collapses. The heat is then propagated according to the equation of thermal conduction. However, this high temperature only happens in very short (a few nanosecond) time scale and, during most of the cycle, heat is transferred into the bubble due to the large expansion decreasing the internal temperature. It has been shown that the net heat transfer in many cases favors heat deposition into the bubble (Kamath *et al.*, [106]). For a bubble oscillating isothermally, the thermal contribution has been shown to have a negligible effect on the heating by Hilgenfeldt *et al.* [43] The bubble model we used throughout this work takes account of thermal damping, and we believe it is better than the isothermal assumption; nevertheless we expect the effect of heat conduction through the bubble wall is very small, and we will ignore this contribution.

Additional heating mechanisms for bubble heating

Other potential sources of energy deposition from bubbles include bubble shape oscillations and multiple-bubble scattering. Shape oscillations on bubbles during noninertial cavitation were first observed by Kornfeld and Suvorov [107]. These oscillations often cause radiated sound at a frequency lower than that of volume pulsation, and non-spherical motion could lead to a much greater viscous dissipation than spherical oscillations owing to the increased shear induced. However, experimental evidence showed small bubbles would always keep its

spherical shape except in a few cases. We use the spherical bubble model in this work, and the heating due to shape oscillations is neglected.

Multiple-bubble scattering is another process which may enhance heating. Sound scattered by one bubble may be scattered again by other bubbles. During this process, sound is scattered back and forth and this will increase the opportunity for the sound to be absorbed. From another point of view, multiple-bubble scattering increases the effective path length of the sound propagation. Energy that would otherwise pass through is redirected and deposited in the surrounding area. As the primary acoustic field increases, cavitation occurs in the pre-focal area. The multiple scattering of bubbles in the pre-focal may cause "shielding" of the sound field. Energy normally focused at the focal region, is redirected and dissipated in the pre-focal region due to multiple-bubble scattering, which elevates the temperature in the pre-focal region. The focal region, which would normally be the highest temperature region, receives less energy, and only a small temperature elevation is obtained there. This process only happens at very high intensity cases since cavitation in the pre-focal region is required. Many experiments have shown 'tadpole' shaped lesions after HIFU exposure at high pressures and cigar shaped lesions at low pressures [33][37]. The 'tadpole' shaped lesions are caused due to the shielding effect.

This research will not consider the effect of multiple-bubble scattering, and to model this interaction is beyond the scope of this work. From a practical or applications perspective, it may even be desirable to minimize or avoid this effect for reasons of predictability.

The distribution of bubbles

All the preceding analysis about the heating due to cavitation is based on single bubble dynamics. We have made the estimate in previous work [48] that a bubble number of order 20 in the focal region is enough to produce enhanced heating. Our HIFU transducer has a total focal volume of about 10 μL of the focal volume (estimated from full width of half maximum

intensity); given this number and with the bubble radius of 10 μm, the void fraction in the focal region is very low. At this void fraction, the single bubble model could be valid.

However, to estimate the temperature rise in the focal region, we need to accurately estimate the heating rate at every point. The heating rate we discussed in the last section is only for a single bubble; the position of the bubble, however, needs to be determined. The occurrence of cavitation is related to the peak negative driving pressure amplitude. We therefore use a negative pressure value as a threshold for cavitation. The threshold value can be measured from experiments. A uniform bubble density distribution is assumed throughout the focal region. Another uncertainty that may affect the heating is the initial bubble size distribution in the tissue phantom, which is determined by the nuclei in the tissue phantom. Our current experimental technique does not allow us to control this in the tissue phantom. However, we can change the air concentration in the tissue phantom which we believe will change the nuclei size in the tissue phantom, and thus the cavitation threshold, growth rate and heating, as we will show in Chapter 4. For a 1-second insonation, the initial nuclei size will only have a limited effect on the heating, as we have shown in the bubble dynamics in Chapter 2, since the high speed growth rate right after the nucleation will eliminate the small initial differences between bubbles.

3.5 Solving for temperature

Having these heating sources in hand, now we are ready to solve the bioheat transfer equation. The numerical implementation of the BHTE is analogous to the pressure solution, although it is much simpler. The discretized partial derivatives in space used for the BHTE are the same as those for the pressure except for the time derivative, for which a centered difference is used to determine the next temperature value in time:

$$\frac{\partial T}{\partial t} = \frac{1}{2dt}\left(T_{i,j}^{n+1} - T_{i,j}^{n-1}\right) \tag{3.27}$$

Spatial and temporal grids, solution domain, initial and boundary conditions

Compared to the pressure solution, the temperature response is substantially slower. Thus we can use a much larger time step for the temperature. Specifically, a time step of 1 ms is sufficient for simulation stability and accuracy. The same spatial grid will be used in the temperature solution. The solution domain for the BHTE may also be decreased and limited only to the tissue phantom. This is because the tissue phantom is primarily heated from the center, and there is little heating away from the focal region. Then we only need to solve the BHTE in a small region centered at the focus of the acoustic field, which is also the peak temperature point. The large amount of water surrounding the phantom serves as an excellent constant temperature bath. Although the water path is important to the pressure solution, it simply serves as a constant boundary condition in the temperature solution. The initial condition is set to be the ambient temperature at every point.

3.6 Thermal dose

After the temperature elevation is determined, a method of thermal dose can be used to predict tissue survival or damage. The effect of temperature elevation in tissue during HIFU depends on the achieved temperature and the duration of the exposure. A given temperature history and approximate reaction parameters can be converted to an equivalent dose in degree-minutes at a constant temperature, thus enabling direct comparisons of different therapy studies. Therefore, a relative thermal response above 43 $^{\mathrm{o}}$C can be defined as an equivalent thermal dose at 43 $^{\mathrm{o}}$C by the following equation:

$$TD_{43}\left(\min\right) = \sum_{t=0}^{t=t_{final}} R^{\left(43-T_t\right)} \Delta t \tag{3.28}$$

where T_t is the temperature in degrees Celsius, and R is 0.5 above 43 $^{\mathrm{o}}$C and 0.25 below 43 $^{\mathrm{o}}$C. The total thermal dose to a tissue sample is determined by the temperature history of the sample taken at time points Δt apart. This value is an independent measure of the thermal damage to a sample in an experiment.

3.7 Example of model predictions

In this section we are going to show some typical predictions. The sound field is generated by a HIFU source, and the resulting temperature field is simulated by the method described above. The driving frequency used in the simulation is 1 MHz, and the duration is 1 second, which is the same as in our experiments. The material properties are listed in Chapter 4.

Figure 3.3 shows a plot of acoustic field intensity in the focal plane and a cross section through the z-axis, with a peak pressure amplitude of 1 MPa at the focus. The whole focal region has a cigar shape, and side lobes appear in the surrounding area, an effect due to diffraction. Compared to the geometric center of the transducer, the real focal region is shifted towards the transducer, and this is also an effect of diffraction of the sound beam.

The resulting temperature field is shown in Figure 3.4. For this 1-second insonation and the same material properties, the resulting temperature field is very similar to the intensity field. The temperature field is less sharply peaked than the intensity field due to heat conduction. As the intensity increases, the heat conduction will become more and more important and that will cause a large deviation from constant proportionality between the temperature and intensity at a given spatial location.
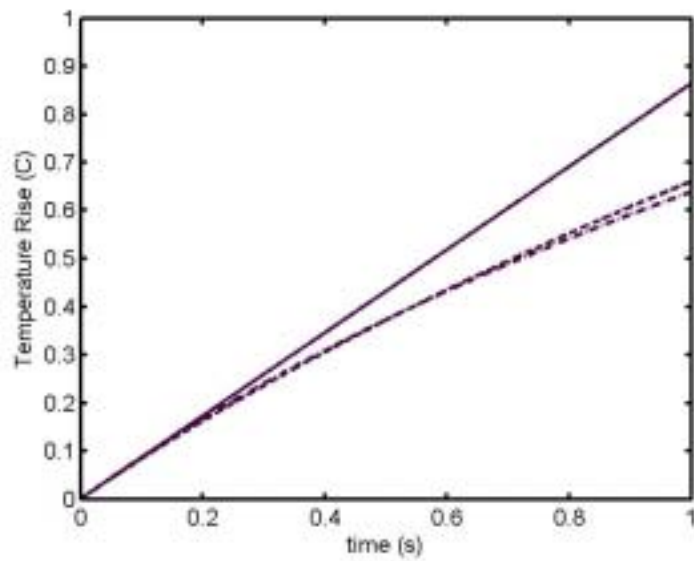
Figure 3.1 The comparison between different heating models. Linear heating rate (solid line), Parker's model (dash line) and BHTE model (dash and dot line). For the material properties we used in this simulation, see Chapter 4.
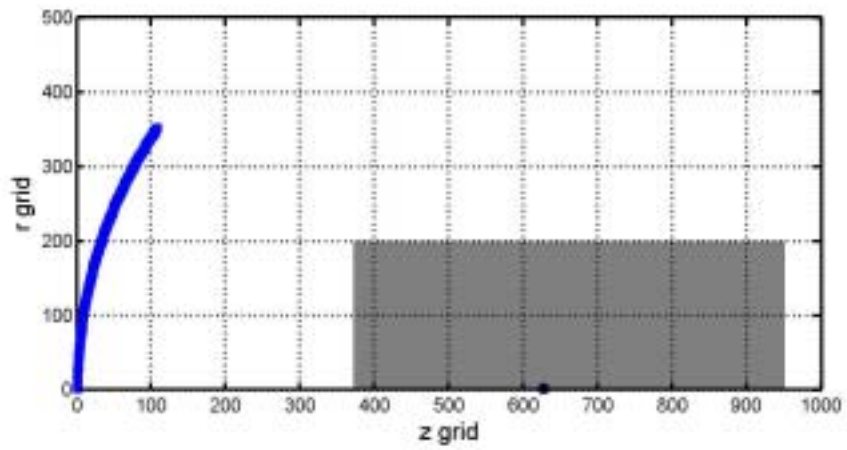
Figure 3.2 The solution domain for the FDTD code. The dark area indicates the tissue phantom. The black dot is the position of the geometry focus.
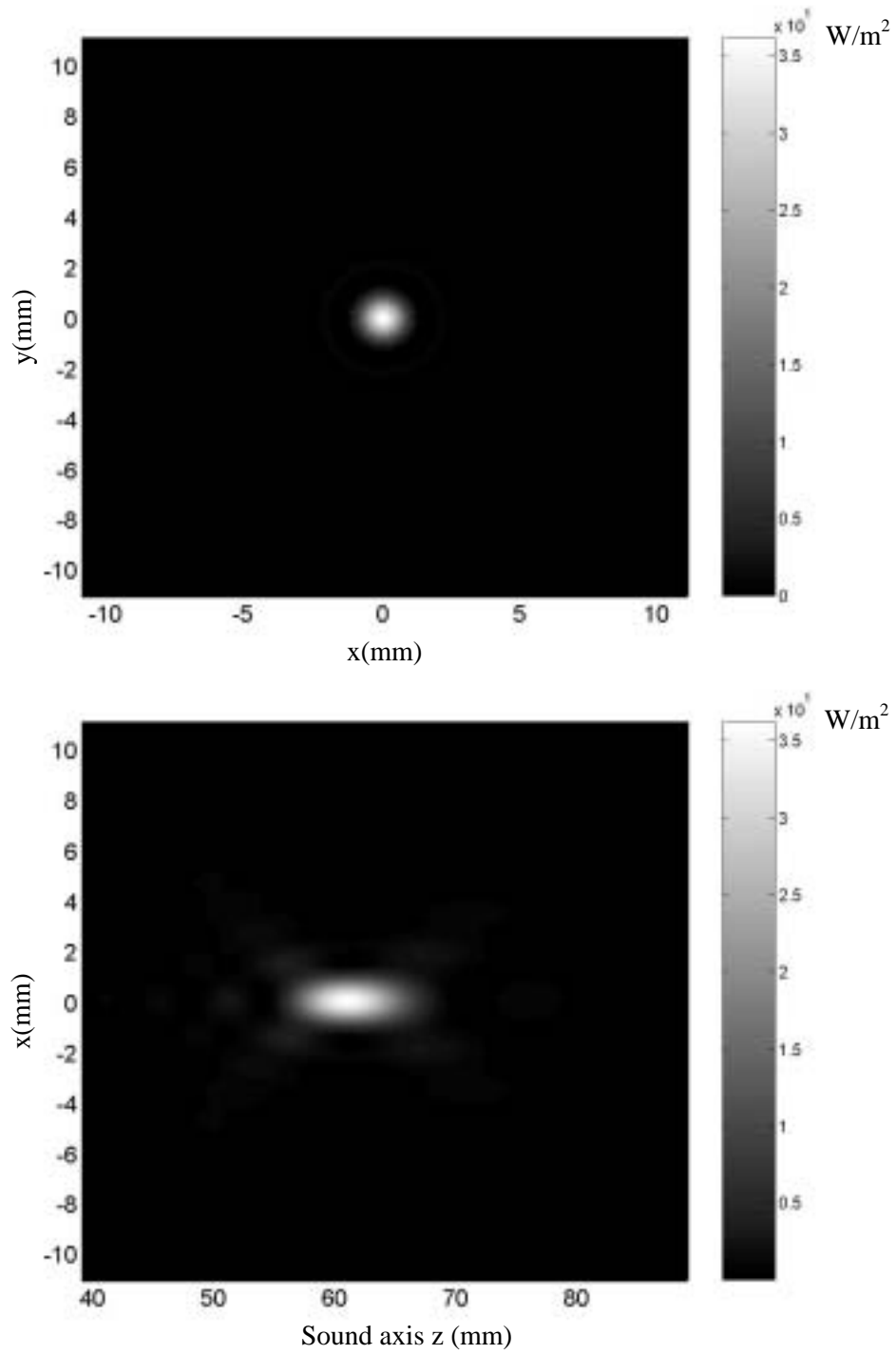
Figure 3.3 An example of intensity field mapping calculated by FDTD code at 1 MPa peak pressure. a) (top) focal plane mapping; b) (bottom) x-z plane mapping.
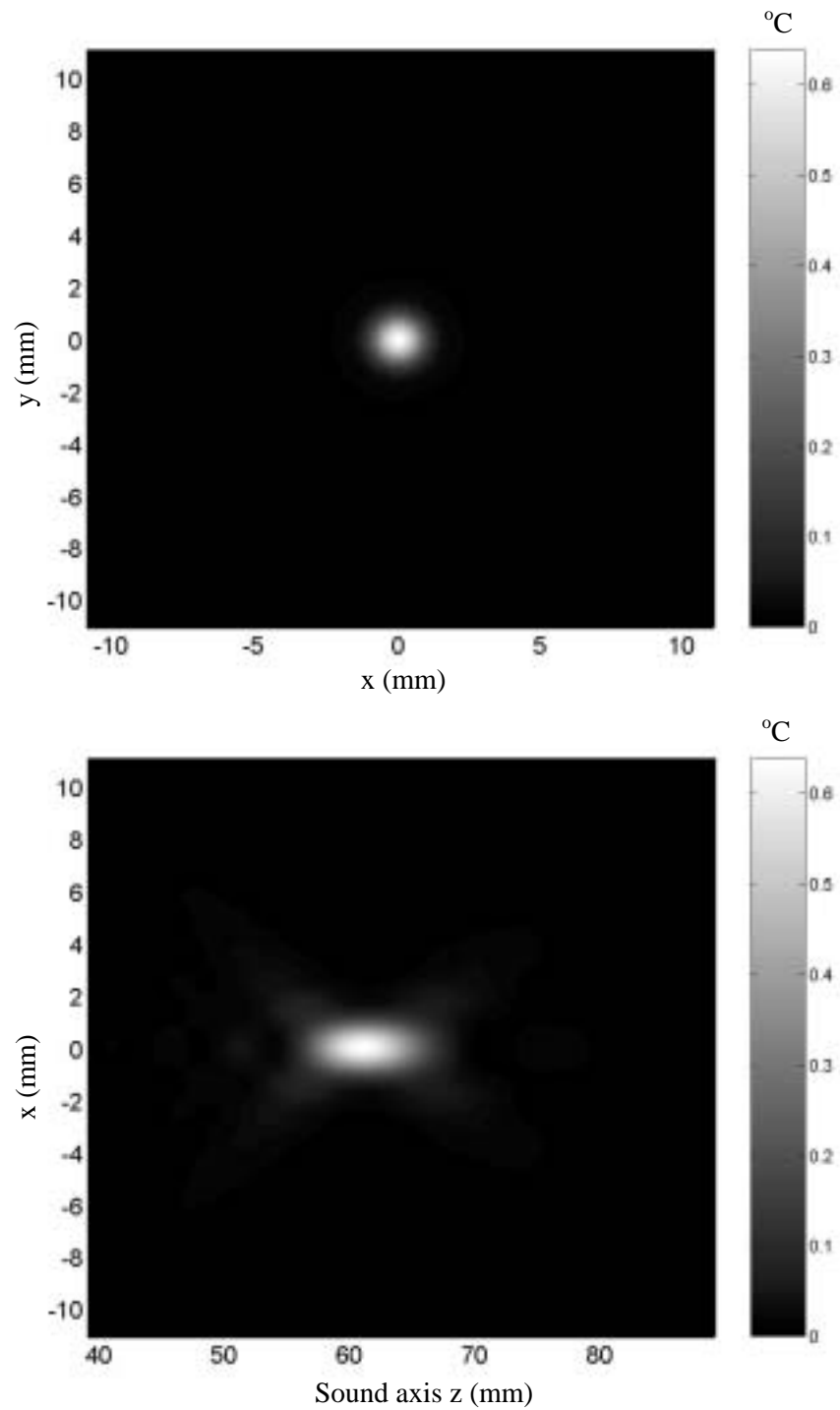
Figure 3.4 An example of temperature mapping at 1 MPa peak pressure for a 1-second insonation time. a) (top) focal plane mapping; b) (bottom) x-z plane mapping.

Chapter 4

Experimental setup and the results

We already presented the results for bubble dynamics in chapter 2 and the heating model in chapter 3. In this chapter, we are going to show some experimental results. As reviewed in Chapter 1, much in vivo and in vitro experimentation has exhibited bubble-enhanced heating. The characteristics of bubble-enhanced heating include a dramatically increased heating rate, threshold dependence and erratic temperature rise. Experimental evidence in this chapter serves as 1) a tool to verify the theoretical model; 2) a source for new physical phenomena which will help us to better understand this complicated phenomenon.

In this chapter, an experimental system is going to be developed. Three experiments are implemented and discussed. The First experiment is the observation of subharmonics emitted from cavitation; subharmonics are often used as evidence of the presence of cavitation. The second experiment investigates the effect of different dissolved gas concentrations on the heating behavior in the tissue phantom. The last experiment measures the heating due to the presence of contrast agents. Microbubble-based contrast agents can serve as the initial cavitation nuclei in the tissue phantom. The relationship between the threshold for enhanced heating and the inertial cavitation threshold for contrast agents is investigated. The temperature rise in the tissue phantom is monitored by thermocouples, and experimental data is collected through a PC by using MATLAB. The acoustic signal emission is received by a passive cavitation detector (PCD) and collected by a PC.

4.1 Experimental Apparatus
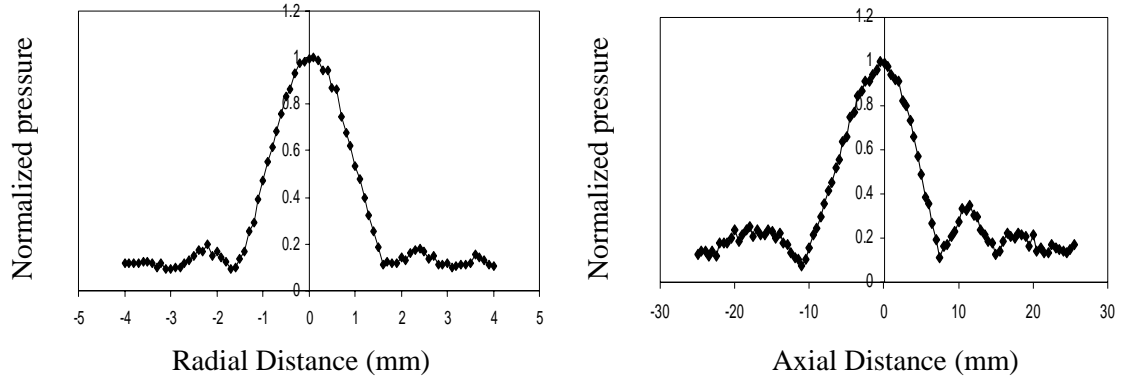
Figure 4.1 H101 Transducer measured beam profile
at 1MHz. a) Radial pressure profile, b) axial
pressure profile

In this work, we expanded previous work done by Holt and Roy [44], and Edson [48]. The experimental apparatus is similar to that of Edson [48]. The source of the system is a single element, spherical focused, piezoelectric transducer (H101, Sonic Concepts, Woodinville, WA). The transducer has a 6.26 cm geometric focal radius and a 7.0 cm aperture. The center frequency of this transducer is 1.1 MHz and the bandwidth is 0.85-1.35 MHz. At 1 MHz, the FWHM (full width of half maximum intensity) is about 1.5 mm at the focus and the focal region length is about 8 mm. The transverse and axial beam profiles are shown below in Figure 4.1. This calibration is done in water by using a PVDF hydrophone. In all the following experiments, 1-second continuous wave tone bursts of 1 MHz are is used. During the insonation, a 1 MHz sinusoidal wave is generated by a function generator (3314A, Hewlett Packard, Palo Alto, CA) and is then amplified by a power amplifier (A-150, 55dB fixed-gain, Electronic Navigation Industries, Rochester, NY) before going into a matching network. Finally, the signal goes into the

transducer from the matching network. All the experiments are conducted in an acrylic water tank. The size of the tank is $15 \times 15 \times 45$ cm.

In all the experiments, a tissue phantom is used. The use of the tissue phantom has the following advantages: 1) it decreases the experiment expense; 2) the material properties are easy to control; 3) it is convenient to control the shape of the tissue phantom. At high temperature, the tissue phantom is liquid and can be poured into a pre-prepared mold; and it will solidify in room temperature. The tissue phantom is constructed by first creating a mold with the desired shape. The phantom holder is a cylindrical pipe with 40 mm diameter and is about 60 mm long. One end is attached to an acrylic plate which has a screw hole on it, and the other end of the pipe is open. Before the tissue phantom solidifies, it is poured in the mold and then the open end of the holder is covered with an acrylic plate until it solidifies. There is a small window at the side of pipe, which is also covered with an acrylic plate before the solidification of the phantom. After phantom is poured into the mold, we wait for about 10 hours before the experiment starts. The two acrylic covers will be taken away when the experiment starts. Ultrasound is applied through the open front and focused inside the phantom.

Agar-graphite phantom

The agar-based phantom is a mixture of 600ml water, 24g of graphite power (for scattering), 18g of agar, 0.75g of methyl paraben (a preservative), and may also contain 16ml 1-propanol to adjust the sound speed in the phantom. First, deionized-water is heated to above 85 $^{\text{o}}$C, and then methyl paraben, agar, graphite (96% purity, 325 mesh, J.T. Baker, Paris, KY), and 1-propanol (optional) are added and well stirred. The whole mixture then may be degassed by exposure to a vacuum if desired. While degassing the whole mixture should remain in a thermal bath to keep temperature at around 70 $^{\text{o}}$C to prevent the mixture from solidifying. The whole mixture is then poured into the mold. It usually takes over 10 hours for the mixture to cool down,

and after cooling down the mixture becomes solid. During the process of cooling, the phantom should be isolated from air, as it should when the phantom is stored. The most appealing feature of the agar-based phantom is that the critical sound properties of the phantom can be easily varied by altering the phantom recipe and can be controlled independently. For example, the sound speed can be altered by adjusting the amount of 1-propanol, and the attenuation can be changed by using different amounts of graphite powder. Both of these properties have a nearly linear dependence on the weight percentage. The recipe and the properties of the phantom made by this recipe are given in Table 4.1 and 4.2 respectively.

Table 4.1 The recipe of the tissue phantom.

Component	Amount
Water	600 ml
Agar	18 g
Methyl Paraben	0.75 g
Graphite	24 g
1-propanol	16 ml (optional)

Table 4.2 The properties of the tissue phantom.

Property	Tissue	Tissue phantom
Density (kg/m^3)	1000-1100	1044
Sound speed (m/s)	1450-1600	1488
Attenuation (Np/m/MHz)	5.6-17	5.2
Thermal diffusivity (mm^2/s)	0.105-0.106	0.158
Specific heat (J/kg·°C)	3600-3900	3710

The measurement techniques for parameters reported in Table 4.2 have been described by Huang [13]. The nonlinearity coefficient for this tissue phantom is β=4.4. The agar-graphite phantom is black and totally optically opaque; it is not suitable if optical bubble imaging is desired.

Acrylamide phantom

The acrylamide phantom is an optically transparent tissue-mimicking material that is ideal for bubble imaging experiments, and we list it here for future work although the bubble imaging experiment is not a part of this dissertation. An acrylamide phantom is formed by co-polymerization of acrylamide and bis-acrylamide. Polymerization is initiated by tetramethylethylenediamine (TEMED) and ammonium persulfate. In this recipe, 5 ml 30% acrylamide stock solution (mix 29.2 g acrylamide powder and 0.8 g bis-acrylamide, increase sample volume to 100 ml with purified water), 8.4 ml purified water, and 1.5 ml 10X phosphate buffered saline (PBS, mix 8.76 g NaCl, 2.41 g Na_2HPO_4 and 0.41 g $NaH_2PO_4 \cdot H_2O$, increase sample volume to 95 ml with purified water, adjust to pH 7.4 with 6 M NaOH solution, make to final volume of 100 ml, filter with a 0.2-µm filter) are mixed and degassed for 15 min under vacuum. Then 75 µl ammonium persulfate solution is added (made fresh, 20 mg ammonium persulfate plus 100 µl water) followed by 10 µl TEMED. The solution is capped and mixed well and then poured into a mold and left to sit for 2 hours to ensure the reaction is sufficiently complete. The density of the gel is approximately 1030 kg/m^3, and the sound speed is about 1534 m/s. The attenuation is generally too low (less than 0.01 Np/cm@1 MHz) to simulate that of real tissue. Such low attenuation also makes it easier to induce shock formation in the propagation. Attempts made to improve the attenuation by substituting the water with a more absorptive liquid such as glycerin were generally not effective [13]. The acrylamide gel is however very attractive for future research work of bubble imaging.

4.2 Temperature Measurement

The temperature inside the tissue phantom is measured by one or more type E thermocouples (0.125 mm diameter bare wire, response time less than 40 ms, Omega Engineering

Inc, Stamford, CT) located about 22 mm deep from the surface of the phantom and in the middle of the cross section. The thermocouple is connected to a terminal block with cold-junction-compensation (SCB-60, National Instruments, Austin, TX). Another thermocouple is connected to the terminal block and placed in the water for ambient reference. The terminal block outputs are connected to the analog inputs of a multifunction input/output (MIO) computer board (AT-MIO-16E, 100 kS/s, 12 bits, National Instruments, Austin, TX), and the thermocouple voltages are acquired at 1 kHz. These thermocouple voltages are converted to temperature using MATLAB (MATLAB 6.0 Release 12, The Mathworks, Natick, MA) based on thermocouple type and incorporating the cold-junction-compensation reading.

A typical temperature measurement result is shown in Figure 4.2. The measurement is made in the agar tissue phantom. The tip of the thermocouple is placed at the focal plane and 0.5 mm off axis. The temperature is plotted as a function of time for an insonation duration of 1 second, a source frequency of 1 MHz with a peak negative pressure 1 MPa. Figure 4.2a shows the raw data without any averaging. The high frequency noise in the raw data is due to electrical noise in the temperature measurement system. A simple moving average filter can be applied with little or no effect on the relatively slowly changing temperature response in the tissue phantom. Figure 4.2b shows the filtered temperature data after 20-point moving average. The result shows a classic heating-cooling curve and very good repeatability. Unless otherwise specified, the temperature measurement results presented in this dissertation will be processed using a 20-point moving average.

Thermocouple artifact

When using thermocouples to measure temperatures in an ultrasound field, the error of measurement due to the presence of the thermocouple itself is usually referred as the thermocouple artifact. The existence of a thermocouple artifact was first analyzed systematically

by Fry and Fry [96][97] in their research to measure the absorption coefficient of the medium through measuring the rate of heating. The occurrence of the thermocouple artifact depends on many factors, such as the conduction through the thermocouple wire, the finite heat capacity of thermocouple wire, etc. Most of these only have negligible effects on the temperature measurement. However, the effect of viscous heating on the thermocouple surface has a significant effect on temperature measurement. When the acoustic wave is passing through the medium, a relative movement will be induced between the thermocouple surface and the surrounding medium due to the discontinuity of the material. Then the viscous force between the thermocouple surface and the surrounding medium will induce a local heating. The local heating will induce a sharp temperature gradient, and what the thermocouple senses is the peak of this local temperature. As shown in Fry and Fry's paper, this viscous heating-induced temperature rise is a function of acoustic pressure, frequency, viscosity, as well as the size and orientation of the thermocouple. In Fry and Fry's estimate for a 12.5-μm diameter thermocouple in caster oil, the ratio between the temperature induced by viscous heat solely and the undisturbed temperature rise is 0.9 when the thermocouple is orientated transverse to the acoustic field and 2.2 if the thermocouple is orientated along the acoustic field. In our case, we expect the effect of viscous heating should be larger since 1) a large size of thermocouple is used; 2) tissue phantom is a more viscous material than caster oil; 3) the thermocouple is oriented along the acoustic field.

Another type of error, which may be induced by the presence of the thermocouple, is ultrasonic beam distortion resulting from scattering by the thermocouple probe. In addition to changing the pressure profile, this can also cause an increase in the local power density and therefore, induce additional temperature rise. Hynynen and Edwards [108] reported that probes with diameter equal or greater than half of the square root of the sonic wavelength tend to scatter the wave and distort the sound beam significantly. Smaller probes with a diameter less than about

one-fifth of the square root of the wavelength had a very local and small effect on the sound field, and will not have a significant effect on the measurement.

The thermocouple we used in our experiment has a diameter of 0.125 mm, which is much less than one fifth of the square root of the wavelength (the wavelength in our case is about 1.5 mm). The scattering cross section of the thermocouple is also much less than that of cavitation, as we will see in Chapter 5. Therefore we do not see the sound beam distortion due to the presence of the thermocouple. However, the thermocouple artifact caused by viscous heating is an unavoidable effect when using thermocouples in an acoustic field. As shown by Hynynen *et al.* [108] even in water, thermocouple artifact has big effects on the temperature measurement. This is why Parker drew a conclusion that it is not possible to measure temperature in a sound field by using a thermocouple directly.

However, it is still possible to get actual temperature information from the thermocouple through some processing of the measured data. The first method used to correct this thermocouple artifact is the linear rate of heating method [96]. If the sound beam has a wide width and the intensity is low, the heating of the tissue is nearly linear for a short term. Then a rate of heating can be read at the steady state, and the temperature rise can be evaluated through this linear heating rate.

However, many transducers have a narrow beam, and the conduction in the radial direction forces the heating rate to deviate from the linear relation, as shown in Chapter 3. Parker [99][100] developed a temperature heating and cooling equation to fit the measured temperature data and then extrapolated back to find the real temperature in the medium. The same problem will occur when working at high intensity and long duration insonation. Hynynen *et al.* [109] adopted an empirical method in their measurement. They waited for a short period after the insonation and then read the temperature. But as temperature increases, the conduction becomes

much more rapid after the sound field is turned off, and this waiting time should be decreased to get the real temperature. To get a waiting time as a function of driving pressure is impossible in this experiment. In the previous work of our group, Huang [13] developed an *ad hoc* method to correct her measured temperature data by comparing the measurement in viscous non-graphite phantoms. However, one problem with applying that method in our experiments is we are looking for the heating above the cavitation threshold. This *ad hoc* method will not work beyond the cavitation threshold due to the randomness of occurrence of cavitation.

To solve this problem, it is first important to understand the physical background of the role of the thermocouple in our tissue phantom. Our tissue phantom is agar-graphite based. The role of graphite in our tissue phantom is to increase the attenuation of the phantom. An agar phantom without graphite particles has an extremely small attenuation and it is not measurable in our acoustic property measurement system. Adding scattering particles can increase the attenuation greatly. The investigation by Wu *et al.* [110] in a tissue phantom showed that the acoustic energy loss due to the presence of the graphite particles is a result of the effect of mode conversion [111]. Acoustic waves are compression waves, and when compression waves travel through the medium and encounter a particle, acoustic shear waves are excited. This acoustic shear wave is going to convert into internal energy within a few micrometers owing to the extremely high shear wave absorption in gel-type suspending material. According to the result of Wu *et al.,* mode conversion accounts for over 90% of the energy loss in an agar-graphite phantom and only a small part is due to multiple scattering. We simply note that this mechanism of energy loss is the same as the mechanism of the thermocouple artifact. Both of them are due to the presence of a particle in an otherwise homogenous material and both cause an energy loss due to the relative motion between the particle and the surrounding medium.

Now, we can simply understand that the presence of the thermocouple probe in the tissue phantom just increases the local absorption coefficient, and we can therefore employ an effective absorption coefficient. The temperature measured by the thermocouple is actually the real temperature in the surrounding medium of the thermocouple tip. Certainly, due to difference of the material properties between the graphite and the thermocouple, the viscous heating near the surface of each is different, and this effective absorption coefficient will be different from that of the medium itself. We assume that the temperature at the particle surface is the same as that in between the particles. This can be assured by the speed of the thermal diffusion.

This effective absorption coefficient can be measured by the rate-of-heating method. At the beginning of heating, the heat conduction is very weak, and the heating at the surface of thermocouple is linear (or we can say the heating at the medium surrounding the thermocouple tip is linear). A simple estimate through solving the heat transfer equation can give us the effective absorption in this local area. Then a small volume, which includes the part of the volume occupied by the thermocouple tip and a part of surrounding volume, is set to the effective absorption coefficient. We do not account for heat conduction caused by the thermocouple wire during the heating and cooling phase. Fortunately, during the heating phase, much of the thermocouple probe, not only the tip, is going to be heated up by viscous heating, and the conduction through the thermocouple wire probably has an effect on the temperature of the thermocouple part which is behind the tip, but the tip itself will be hardly by affected by the conduction through the thermocouple wire. However, the wire conduction will play a role during the cooling phase, as we will see in the comparison between the experiment and prediction in the following chapter.

4.3 Passive Cavitation Detection

Cavitation activity is monitored by a passive cavitation detector (PCD) [48][112], which is a spherically focused transducer (15 MHz center frequency, Panametrics, Waltham, MA) featuring a 19mm focal depth and a 6.4mm aperture. The transducer is aligned so that the location of the focal region overlaps with the focal region of the source transducer, and therefore it is most sensitive to the sound emitted at the highest intensity region in the sound field, where cavitation is most likely to occur. The PCD transducer will receive two types of signals. One is due to the incident sound scattering from the phantom, which consists of the primary 1 MHz frequency wave; also a small amount of higher frequency components could be received due to the propagation nonlinearity of the sound field. The second part of the received noise is due to the sound emission from cavitation. There are also two type emissions from bubbles. One is the direct scattering from bubbles, which consists of mainly 1 MHz frequency sound; the other is due to the active emission from bubbles, which includes broad frequency components and is related to the nonlinear motion of bubbles. Since the onset of the cavitation is going to be characterized by inertial oscillations, then strong higher harmonic components are expected, which are associated with a short time scale and high accelerations at bubble collapse. The broadband bubble-related noise is something we want to detect by using the PCD. The output of the PCD is first amplified (Model 5662, 54 dB, Panametrics, Waltham, MA) and filtered in high-pass mode with a cutoff frequency of 2 MHz (Model 3940, 24 dB/octave attenuation, Krohn-Hite Corp., Avon, MA) to reduce the effect of the 1 MHz primary field. Then the resulting signal is sent to a gated peak detector (Model 5607, Panametrics, Waltham, MA). The output of the peak detector is directed to the terminal block used by thermocouples and finally sampled with an MIO board. Since a high pass filter with a cutoff frequency of 2 MHz is used, we should only see very a weak scattering signal from the primary field, and strong signals could be primarily related to any inertial

cavitation (Edson [48]). Inertial cavitation is our main focus through this dissertation. Unless otherwise stated, "cavitation threshold" will indicate the inertial cavitation threshold. Figure 4.3 provides the schematic of the experiment system.

4.4 Acoustic pressure calibration

A primary concern in the experiment is the pressure at the focal region. There are two ways to solve this problem. One is to employ a needle hydrophone to measure the acoustic pressure in the focal region directly. By this method, however, we can only get the pressures at discrete points. Our temperature simulation requires knowledge of the intensity of the whole acoustic field. This method also is limited to experimental conditions. Another way to solve this is to make use of the accuracy of our FDTD code [48][13] to calculate the pressure field in the tissue phantom. Since we already know the sound properties of our tissue phantom, this method allows us to ascertain the sound field in the whole tissue phantom and thus evaluate the temperature inside the tissue phantom.

To simulate the acoustic field in the tissue phantom, we need the source pressure, i.e. the pressure at the transducer surface. We are unable to measure the pressure directly at the transducer surface. However, we know the input voltage of the transducer which can be measured directly. We then can develop a relation between the input voltage and the initial pressure we use in the FDTD simulation. First, numerically, we can calculate the pressure at a certain point in the sound field in water by using the FDTD code, e.g. the pressure at the focus, and some p_{source} will be used in the simulation. Then experimentally, the pressure at the focus can by measured in water, and we can record the input voltage of the transducer. Finally, we can bring these two results together, and through the pressure at the focus, the source pressure p_{source} in the simulation can then be related to the input voltage of the transducer. Since in the regime we are working, the

sound propagation remains linear, a linear relation can be assumed between the focal pressure and p_{source} or the input voltage of the transducer:

$$p_f^+ = c_1 V_t^+ \qquad \text{Experimental relation,} \qquad\qquad (4.1)$$

$$p_f^+ = c_2 p_{source}^+ \qquad \text{Numerical relation,} \qquad\qquad (4.2)$$

where p_f^+ is the peak positive focal pressure, p_{source}^+ is the peak positive source pressure and V_t^+ is the peak positive input voltage on the transducer. With these two relations in hand, we will have

$$p_{source}^+ = \frac{c_1}{c_2} V_t^+ = K V_t^+ \qquad\qquad (4.3)$$

This equation allows us to determine the appropriate source pressure to use in the simulations involving the tissue phantoms based on the input voltage measurement in experiments.

Figure 4.4 shows the relation measured in experiments and calculated numerical results. Both results are obtained in water. From these results, we estimate c_1=0.069 MPa/V and c_2=47.9675 from the plots, thus K=0.0014 MPa/V.

4.5 Experimental results

The experiments of Edson [48] have established the correlation between the temperature rise and cavitation activity in our tissue phantom. The purpose of this work is to further investigate the relationship between the temperature rise and bubble activity. The increase of the heating rate is due primarily to the presence of inertial cavitation, as shown in Edson's results. However, what will affect the occurrence of inertial cavitation in a tissue phantom? How will these inertial bubbles oscillate after creation, and what is its effect on temperature rise? Theoretical predictions are limited by the complications of this issue. However, it is possible to

get some important information through experiments, and that can help us to understand the physics of cavitation in this area. Furthermore, it can help us simplify some aspects of this problem and build a physical model to predict it. Cavitation activity is affected by the incident sound pressure, frequency and insonation duration, and the material properties of the tissue phantom. Different tissue phantoms may have different cavitation thresholds and could yield different temperature rise behaviors. The first result we will show here is the acoustic emission result. The second experiment is to investigate the effect of gas concentration on the cavitation threshold and temperature rise. Finally, the observation of temperature rise due to the presence of contrast agents will be investigated.

4.5.1 Harmonic emission from the tissue phantom

Many researchers have monitored the occurrence of cavitation using acoustic emissions. The emission from a bubble is characterized by broadband noise including the harmonic components of the driving frequency. Specifically the observation of the subharmonic component becomes a kind of criterion for the occurrence of bubbles in many biological ultrasound experiments [34][41][70]. The emission of subharmonic signals from bubbles has a lot of sources, such as the bifurcation of the bubble motion, the shape oscillation of the bubble and the interaction between bubbles. In the parameter space we study, all these sources are possible. As we discussed in previous chapters, we predicted the chaotic oscillation of bubbles numerically, and thus we expect subharmonics in this region (Lauterborn *et al.*, [95]). Multiple bubble interaction is another source for subharmonics although we do not attempt to quantify this effect here. Finally, recall that the bubble size distribution is bounded by the shape instability threshold, and this also is a source for subharmonics (Eller and Flynn, [113]). All of these are our motivation for these experimental observations.

In this experiment, the output of the 15 MHz transducer was acquired by a spectral analyzer (Hp 89140, 16 bits), and the temporal peak of each frequency component was recorded. We found if the tissue phantom contains no 1-propanol, we could not observe subharmonics. Therefore 1-propanol was added to the tissue phantom in order to observe subharmonics. As we described previously, the role of 1-propanol in this tissue phantom is to increase the sound speed. Another material property 1-propanol affects is the viscosity. More 1-propanol will decrease the viscosity. The results for the harmonic components are shown in Figure 4.5. When the driving pressure is less than 1 MPa, only fundamental and second harmonics were observed. The level of the second harmonic signal is much less than that of the fundamental. The second harmonic signal is due to the nonlinearity of the tissue phantom. When the driving pressure is larger than 1 MPa, the level of the fundamental and second harmonic signals suddenly jump to a much higher level and, as the pressure further increases, the level of the second harmonic becomes almost the same as fundamental harmonic. At the same pressure value, other harmonics were observed too. Simultaneously, we also observed the subharmonic signal, which usually is thought of as a unique feature of cavitation. Compared to other harmonic components, the subharmonic signal is always much lower.

From these results we attempt to collect some information about the bubbles in our tissue phantom. The signal of the subharmonic is very weak, which is about 20dB less than the second harmonic. This may be because 1) only a few bubbles grow into the chaotic region; 2) since bubbles have to pass though the chaotic region before they hit the shape instability threshold, bubbles may never hit the shape instability threshold; 3) viscosity in the tissue phantom is very high. In the high viscous region, there is no chaotic oscillation and the bubble size distribution is bounded by the rectified diffusion threshold. Since we did not observe subharmonic signals in the tissue phantom when there was no 1-propanol, we probably can conclude that the viscosity in our

97

tissue phantom is very high and that is the reason why the level of the subharmonic signal is low. This conclusion is consistent with our bubble dynamic results in chapter 2. Bubble shape instability and chaotic oscillations, which are the most likely sources for subharmonics, only happen in the low viscosity region.

4.5.2 Dissolved gas concentration measurement

The dissolved gas concentration in the tissue phantom will affect the nuclei distribution directly, so it will have an important effect on the onset of cavitation [114][115][116][117][118]. Different gas concentration samples could have different heating behaviors due to the different nuclei and bubble growth rates. To measure the gas concentration inside the tissue phantom, we employed a Foxy Fiber Optic Oxygen Sensor (A755, OceanOptic, Inc.). The tissue phantom is prepared in air, so we assume the oxygen percentage will not change in the tissue phantom, it is always a constant percentage of the total gas in the phantom. Then by measuring the oxygen concentration inside of the phantom, we can know the total air concentration in the phantom. The Foxy Fiber Optic Oxygen Sensor uses the fluorescence of a ruthenium complex in a sol-gel to measure the partial pressure of oxygen and then uses Henry's law to obtain the corresponding oxygen concentration. Oxygen molecules are able to quench fluorescence, and the degree of fluorescence quenching depends on the partial pressure of oxygen, as well as the absorption and scattering of the medium. Thus it is necessary to calibrate the oxygen sensor in our tissue phantom first before using it.

To calibrate the oxygen sensor, we first need to prepare standard samples. We made a tissue phantom sample in air and then cut it into roughly 1.5 cm cubes. These small samples were stored in different water samples which have different dissolved air concentrations. Water samples are pre-degassed under different ambient pressures. After phantom samples are stored in

water, the same ambient pressures continue maintaining. We used these samples to calibrate the oxygen sensor every day until it yielded consistent results, then the calibration was finished and the oxygen sensor ready to use. Since the diffusion process is very slow, it can take more than two weeks to reach the gas equilibrium in the samples. Because 1-propanol could cause permanent damage to the oxygen sensor, the tissue phantoms we used in this experiment did not include 1-propanol. This caused a low sound speed of 1488 m/s at room temperature. There are two algorithms available to convert relative fluorescence intensity to oxygen concentration. One is a linear algorithm, the Stern-Volmer equation, which can give us good results at low air concentrations (less than 20% of the saturation value), and only requires two standard samples to calibrate. Alternatively, we may use a second order polynomial algorithm, which needs at least three standard samples to calibrate. Temperature also has an effect on the output of the oxygen sensor, and it is necessary to calibrate the sensor at different temperatures if one expects to use the oxygen sensor over a broad range of temperatures. But if the temperature change is within 3 degree Celsius, which the oxygen sensor cannot sense, temperature compensation is unnecessary. Since we always worked at room temperature, which is around 20 ^{o}C$\pm$2 ^{o}C, we do not expect the temperature to affect our results, therefore, we do not use temperature compensation in our experiments. The calibration result is shown in Figure 4.6. After the calibration, the Stern-Volmer constant or the coefficients in the second order polynomial equation were determined. When the oxygen sensor was used to measure the air concentration, we still needed an additional known air concentration standard sample to achieve the calibration.

To obtain different gas concentration tissue phantoms, we degassed the phantom for different periods. To get low air concentration tissue phantom samples, we used well-degassed clean water. After the phantom was poured into a flask, the flask was placed in a 70 degree C water bath to keep the phantom from solidifying. We degassed the liquid phantom for about one

99

hour. To obtain moderate air concentration tissue phantom samples, we used gassy clean water to prepare the phantom and only degassed for half an hour. Finally, a tissue phantom sample was immersed in air saturated water for one week to get an air saturated tissue phantom sample. For each measurement, more than 600 mL of tissue phantom material was made and poured into three holders: one for experimental use, and the other two for measuring sound speed and attenuation coefficient. After the sound speed and attenuation coefficient measurements, the two samples were used to measure the air concentration. Since all the samples were made by the same process, we can assume there is the same air concentration in these tissue phantom samples. The experiment was accomplished in a tank filled with well-degassed clean water. Since the air concentration in the tissue phantom sample could be different from that of surrounding water, a change in the tissue phantom sample may occur while the experiment, which takes over four hours, is proceeding. To monitor this, we recheck the air concentration in the sample which is used in our temperature measurement experiment after the temperature measurement. It was found that these air concentration measurement results (at the center of the phantom where the focal region was located) were consistent even over four hours!

To determine the air concentration in the tissue phantom, a one point calibration is needed to supplement the air concentration measurement. We cut some samples and put them into air saturated water for several days to allow them to become saturated. These samples were used as the standard samples which have the saturated value.

4.5.3 Temperature measurement results

In these experiments, our purpose is to investigate the role of cavitation in HIFU and try to explain how cavitation activity is related to temperature rise. We used 1-second continuous wave (CW) burst as the incident sound. As described before, the temperature is measured by a

single thermocouple which is directed to an MIO computer board and sampled at 1 kHz. The data are gathered by MATLAB 6.0, and a 20-point moving average is employed to smooth the results. The results are presented in Figure 4.7. The results of three different air concentration samples are presented here. Five measurements are made for each driving pressure. As pointed out in the work of Holt and Roy [44] and Edson [48], the cavitation threshold corresponds to the sudden peak temperature jump. Several features may be mentioned:

a) The measured cavitation threshold changes for different air concentration samples. Low air concentration samples have higher threshold pressures than high air concentration samples. In these results the cavitation threshold decreases from 1.8 MPa to 1.4 MPa. The reason for this may be due to the nuclei size changes in different air concentration samples, as well as the limited insonation time.

b) At lower air concentration, the measured peak temperature is erratic. This is indicated by the oscillations of the peak temperature mean, as well as the size of the error bars. For high air concentration samples, the peak temperature has a very smooth slope and exhibits high repeatability. The magnitudes of the standard error are less that 1 ^{o}C before the saturation range for 100% air saturated sample, but can larger than 20 ^{o}C for 24% air saturated sample.

c) The peak temperature rise finally reaches a saturation region after 3 MPa, as presented in previous work [44]. But for low air concentration samples, it only takes several pressure steps to get to a saturation region and then it grows up again, and reaches another saturation region after 3MPa. For high air concentration samples, however, it takes far more pressure steps to get to the saturation region.

Results of this experiment indicate that the erratic heating behavior is only related to the low dissolved gas concentration samples. Low dissolved gas concentration can cause erratic occurrence of cavitation, and thus erratic heating. If there is enough dissolved gas in the medium,

then the occurrence of cavitation is repeatable and, there is enough gas for every bubble to grow, therefore the heating becomes much more repeatable.

4.5.4 Heating with contrast agents

Bubble-based contrast agents have been broadly used in medicine to improve ultrasound imaging [2]. When an ultrasound field is applied to contrast agents, the oscillation of these micron-size bubbles will emit sound, which usually is much stronger than the emission of the background since an oscillating bubble has a very large scattering cross-section. Then an ultrasound scanner can image the region where the contrast agent is. In this work, we are trying to understand bubble-enhanced heating. Contrast agents can provide us a good initial bubble size distribution. The use of bubble-based contrast agents in our tissue phantom will lower the cavitation threshold. Actually there is no nucleation threshold in the tissue phantom since bubbles are already there. The threshold for bubble-enhanced heating to occur will depend on the concentration of contrast agent, since even at low acoustic pressure the contrast agent bubbles will increase the effective absorption. The contrast agent we use in our experiments is Optison which is still in clinic use. Optison is a bubble-based contrast agent with mean diameter of 2.0-4.5 μm. The gas inside of Optison is octafluoropropane (C_3F_8), which has a very low solubility in water. The shell is made of human serum albumin. Since there is a shell around the Optison, the behavior of this contrast agent will be different from that of regular cavitation. The deformation of the shell is finite and it will definitely affect the oscillation of the Optison. Under low amplitude pressure, the shell of the Optison can oscillate linearly and keep emitting sound which can be used in medical imaging. However, linearly oscillating bubbles with a radius around 1 μm will not enhance the heating in the tissue where large concentrations of bubbles are needed. For low Optison concentrations, inertial oscillations are required for Optison to result in enhanced

heating. The shell of Optison bubbles will break up as the Optison goes into inertial oscillations. Once the Optison shell breaks up, its oscillation is going to be pretty much like a free bubble and can be modeled by regular bubble models.

In the clinic, Optison is injected into a patient's body directly, and the circulatory system will bring Optison to the target. In our tissue phantom, there is no such circulatory system, and directly injecting the Optison into the tissue phantom did not work simply because the unbalanced pressure between the outside and the inside of the tissue phantom squeezed the Optison out of the tissue phantom. To solve this problem, we built a small tunnel across the tissue phantom which operates just like a small vessel in tissue. The Optison flows across the tunnel and the ultrasound is focused at the tunnel. A drawing of this design is showed in Figure 4.8.

When the tissue phantom is made, a single wire is placed in the cylindrical mold. After the solidification of the tissue phantom, the single wire is removed and a tunnel for Optison to flow through is created. Optison is diluted first before being injected into the tunnel. A syringe pump is used to inject Optison, and a constant speed of 0.25 ml/min is used. The diameter of the single wire is about 0.48 mm. The thermocouple tip is 0.5 mm away from the tunnel. During the insonation, the ultrasound is focused at the Optison flow. Two Optison concentrations are used here, one has 50-80 bubbles/μL and another has 500-800 bubbles/μL. The measured temperature results are showed in Figure 4.9. The reference temperature rise is obtained by just using clear water without Optison passing through the tunnel during insonation. Prefocus temperature rise is measured by a thermocouple which placed 3.8mm ahead of the focal thermocouple. Comparing the temperature rise at the focal region, we can see when Optison is used, the enhanced-heating threshold is slightly lower. In general for the same pressure, when Optison is used, a higher temperature rise is induced. However, below the enhanced-heating threshold, there is only a slightly higher temperature rise at around 1.1MPa when Optison is used. As pressure increases,

the saturation area is reached and both temperature rises are about the same. For the prefocal temperature, when the Optison is used, the enhanced heating threshold is slightly higher (actually no big difference if realize the large error bars) at low Optison concentration, and lower at high Optison concentration case. No significant differences are observed when bubble concentration is changed. This is not unexpected because after all the input energy is deposited in the bubble region, further increasing bubble density will not increase the temperature since the total input energy is constant.

This experiment did not simulate the case in reality, in which Optison can diffuse into the whole focal region through numerous capillaries, and which would induce a much higher heating rate in the focal region. To simulate this in experiment, we used multiple wires when the phantom was built. Five 0.2 mm diameter wires were used and the thermocouple tip was surrounded by these wires but without touching them. In this way multiple tunnels can be formed after these wires are removed, and more Optison can flow through the target area in the same time period. Therefore, we can expect more heating in this case. The results are shown in Figure 4.10. Compared to the reference temperature rise, it appears there are two temperature thresholds in the focal region when Optison is used. At a pressure value which is below the cavitation threshold value in the tissue phantom, we can see a clear enhanced heating when Optison is used at about 0.9 MPa. Then the second jump happens when the cavitation threshold value of the tissue phantom is reached at about 1.3 MPa. For the reference temperature rise, only one temperature jump happens at the cavitation threshold.

The output of the PCD can give us more information about this, which is shown in Figure 4.11. For all these three driving pressures, the PCD outputs are close to zero when no Optison is present. However, when Optison is used, we start to see some signals at 0.88 MPa, and the signals become much stronger at 1 MPa pressure. Since the output of the PCD is an indicator of inertial

cavitation, we concluded the threshold for the Optison to oscillate inertially is about 1 MPa. The first temperature jump, when Optison is used (Figure 4.10), happens around 1 MPa. It seems clear that Optison can enhance the heating greatly in the tissue phantom only after the pressure is above the inertial cavitation threshold of the Optison. The enhanced heating between the first temperature jump and the second temperature jump is caused by Optison solely and may be useful as a tool for controlled bubble-enhanced heating.
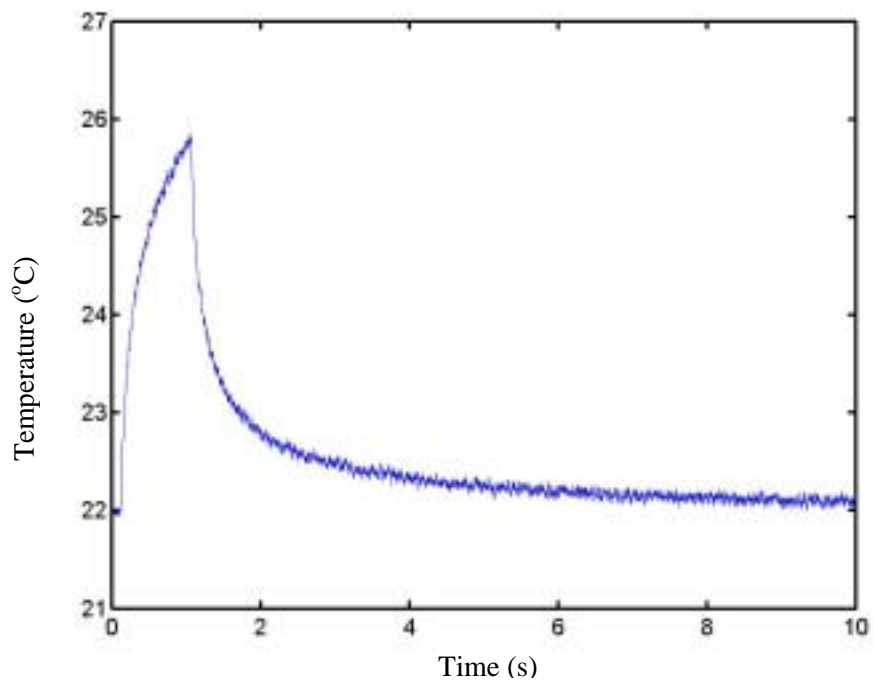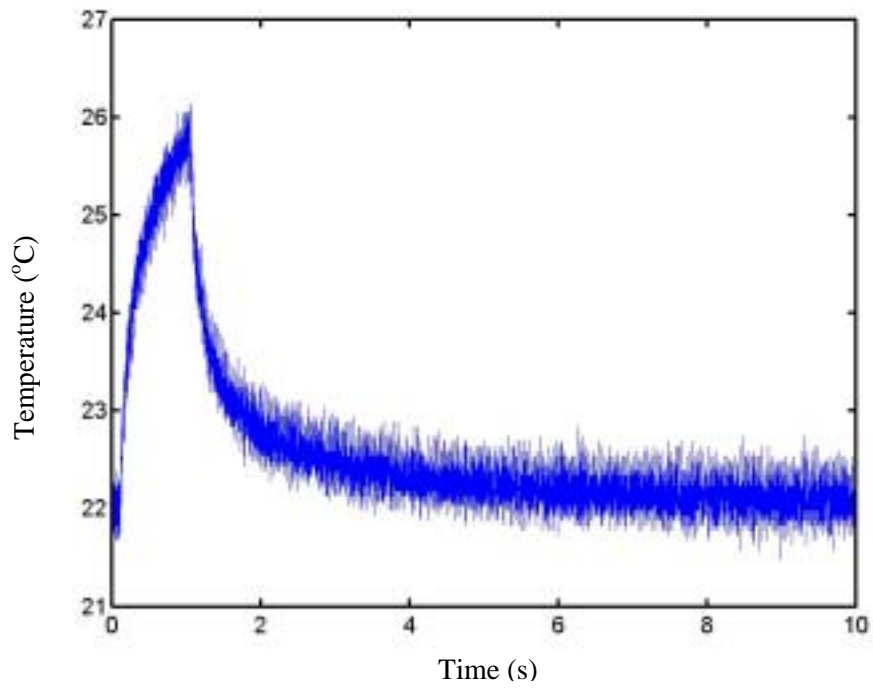
Figure 4.2 Measured temperatures by a thermocouple, 0.5mm away from the focus, vs time a) (top) raw data; b) the same data as a) but smoothed with a 20-point moving average. The driving pressure is 1 MPa.
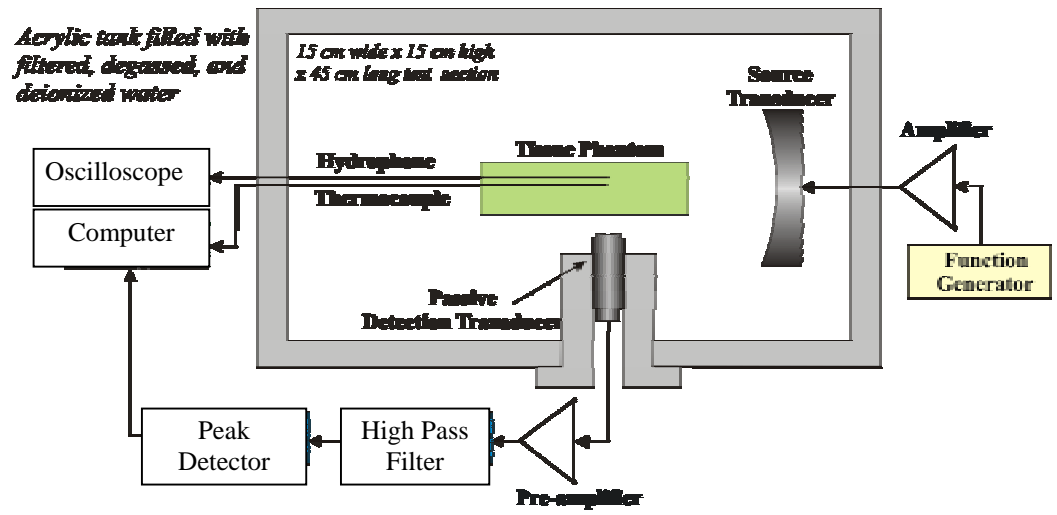
Figure 4.3 Schematic of the experimental setup [48].
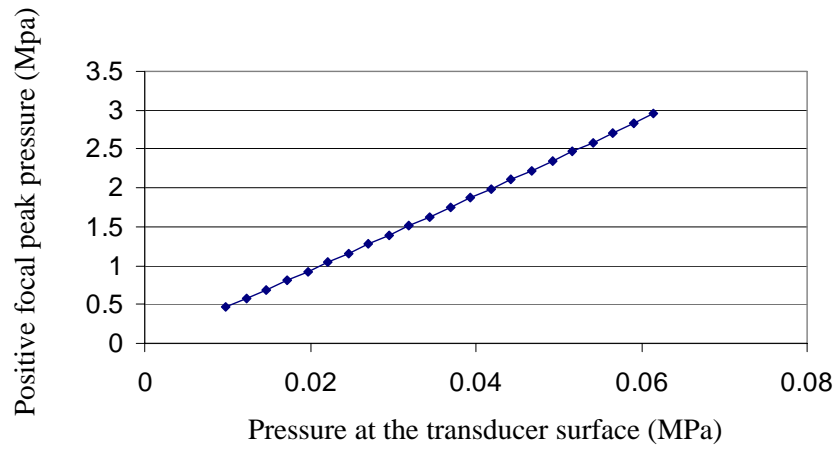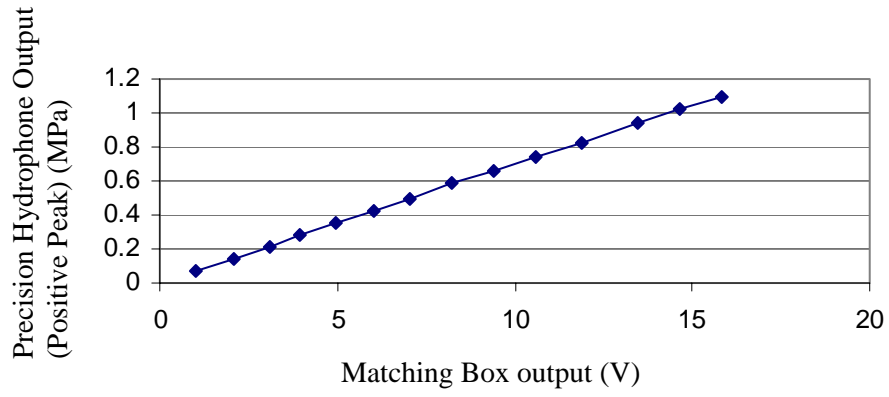
Figure 4.4 Source calibration in water and simulation by FDTD code
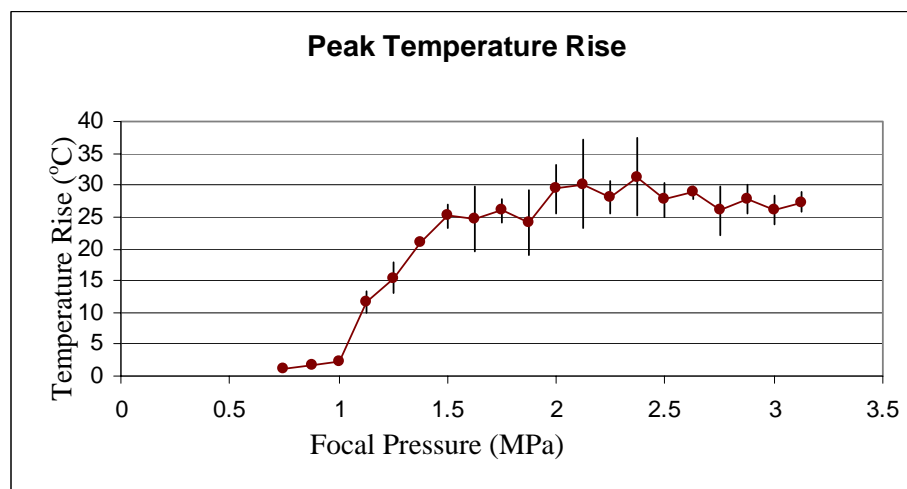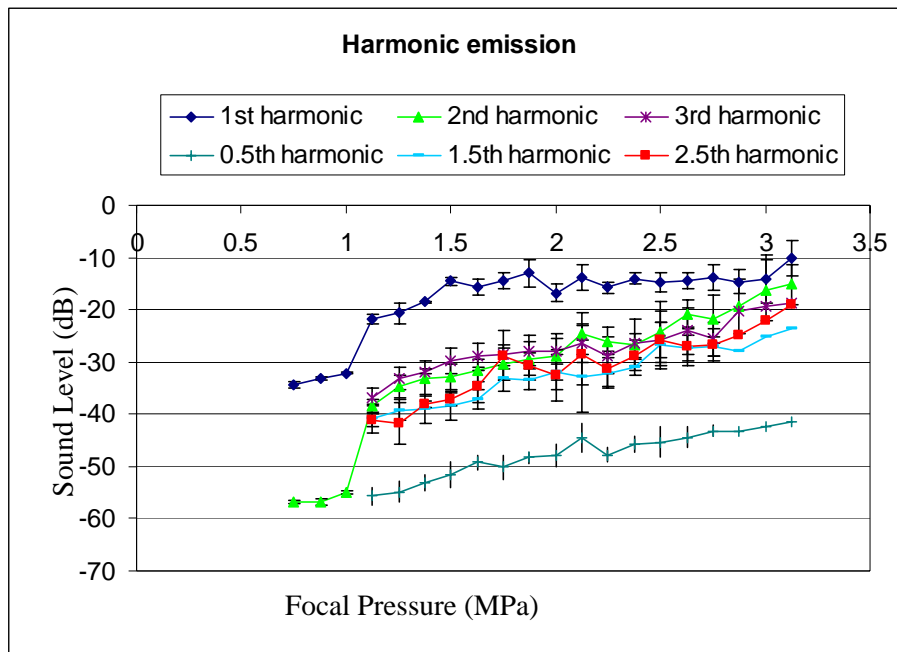
Figure 4.5 Harmonic emissions from a tissue phantom and the corresponding temperature measurement.
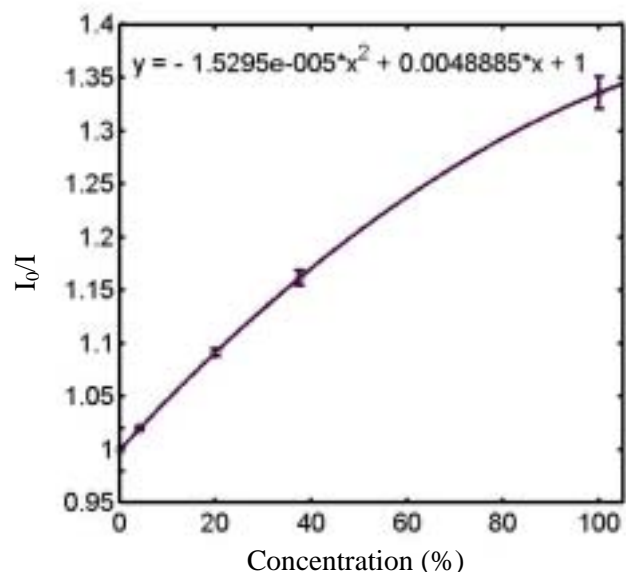
Figure 4.6 The calibration data of the Foxy Fiber Optic Oxygen Sensor. I_0 is the intensity of the fluorescence when there is no oxygen and I is the measured intensity of the fluorescence. The fitted second order polynomial equation is shown too.

a)
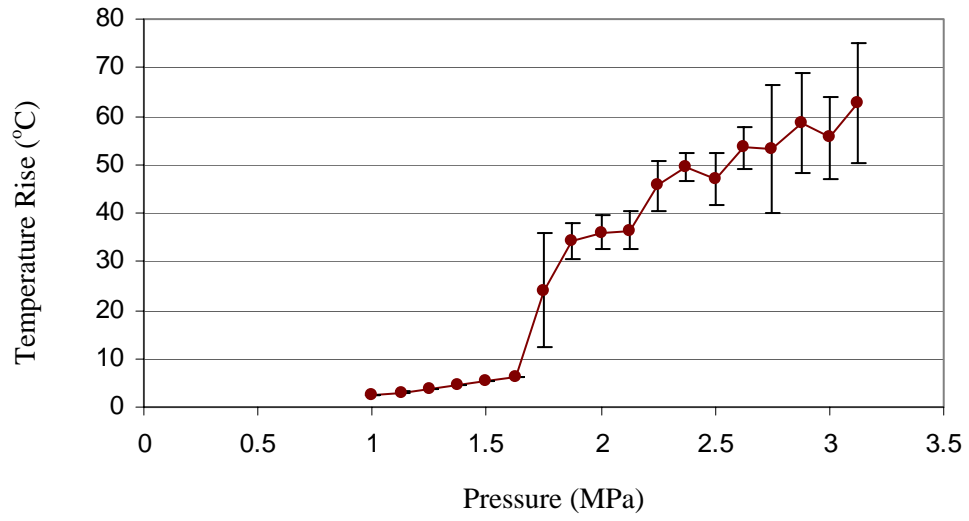
b)
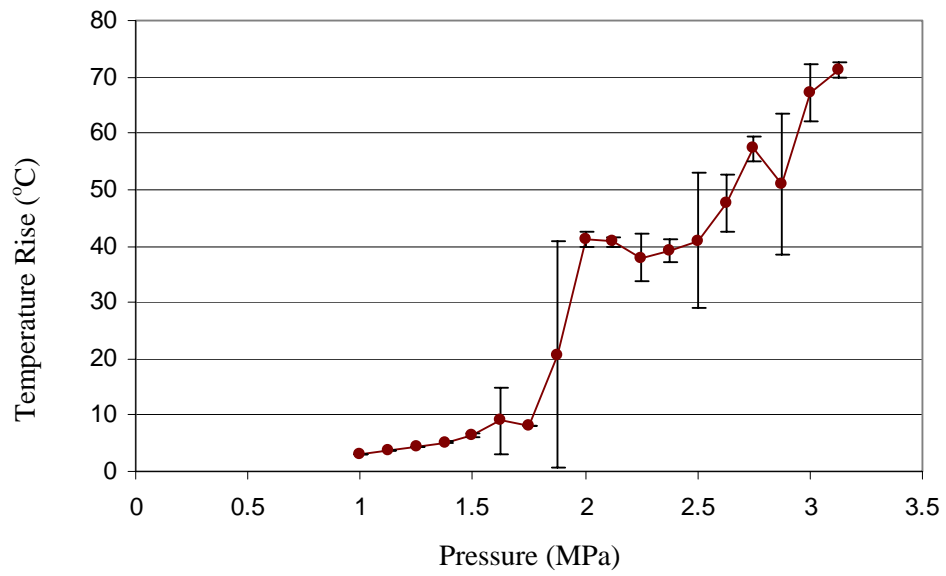
c)
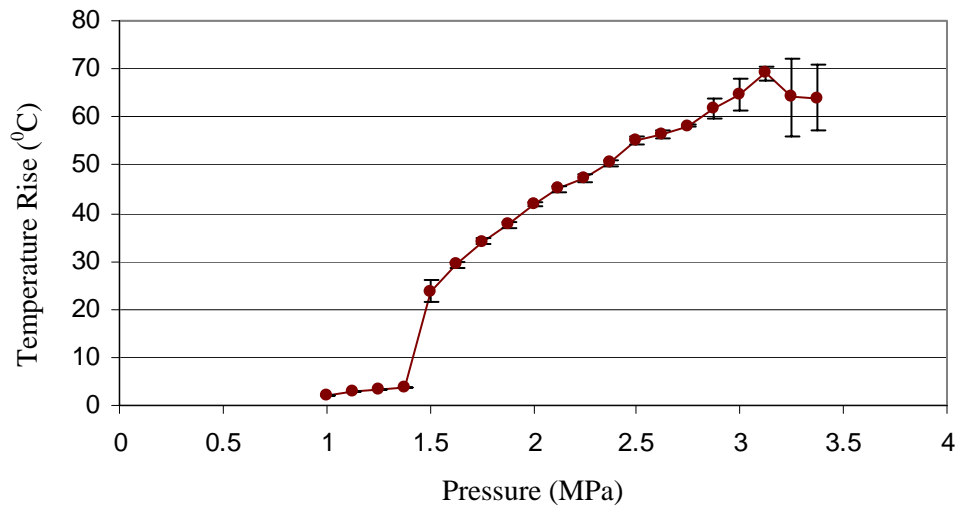
Figure 4.7 Temperature measurement results for different dissolved gas concentrations. a) $c_i/c_0=39.2\%\pm3.6\%$; b) $c_i/c_0=24.2\%\pm3\%$; c) $c_i/c_0=100\%$.
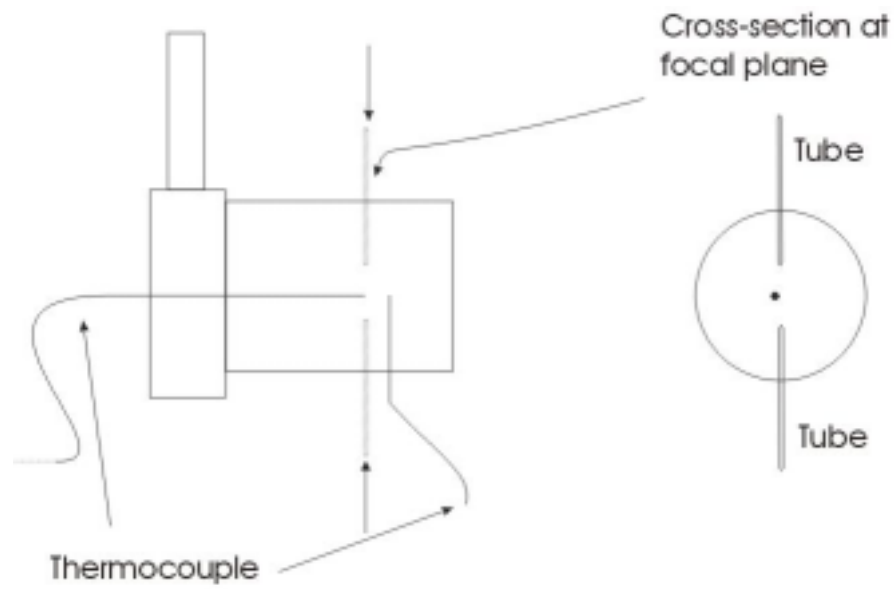
Figure 4.8 The schematic for the holder used in Optison heating experiments
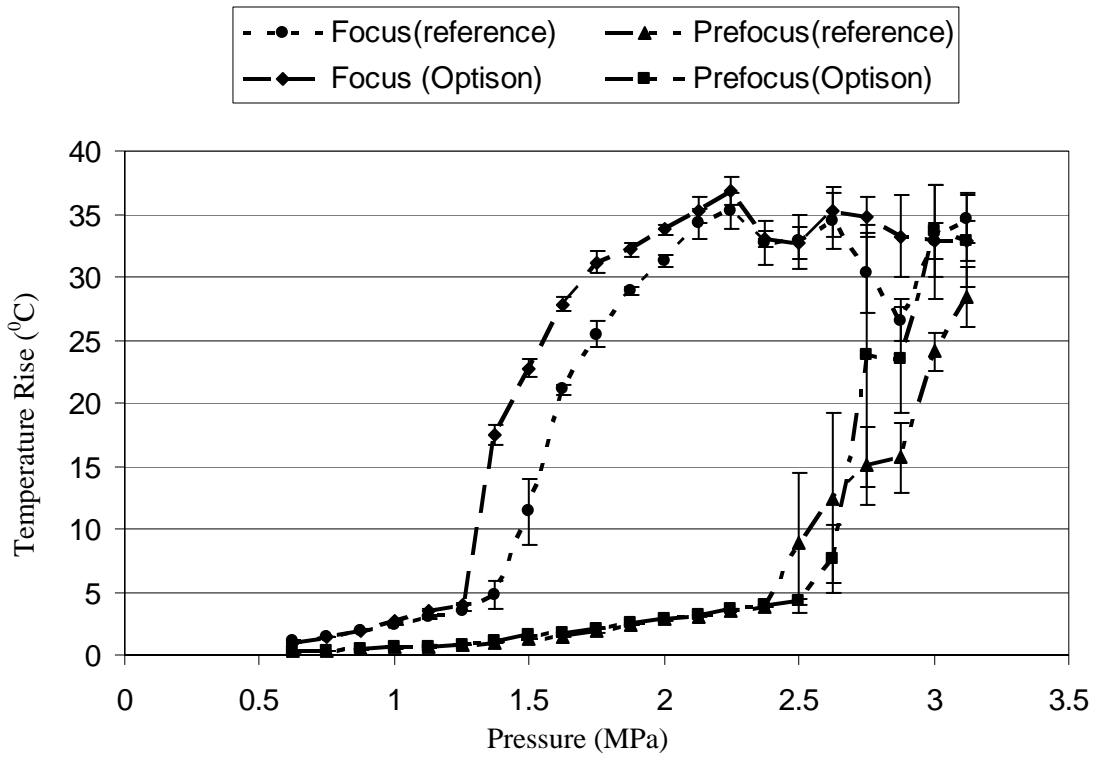
Figure 4.9a Temperature measurement results with a single wire at micron bubble concentration 50-80/μL
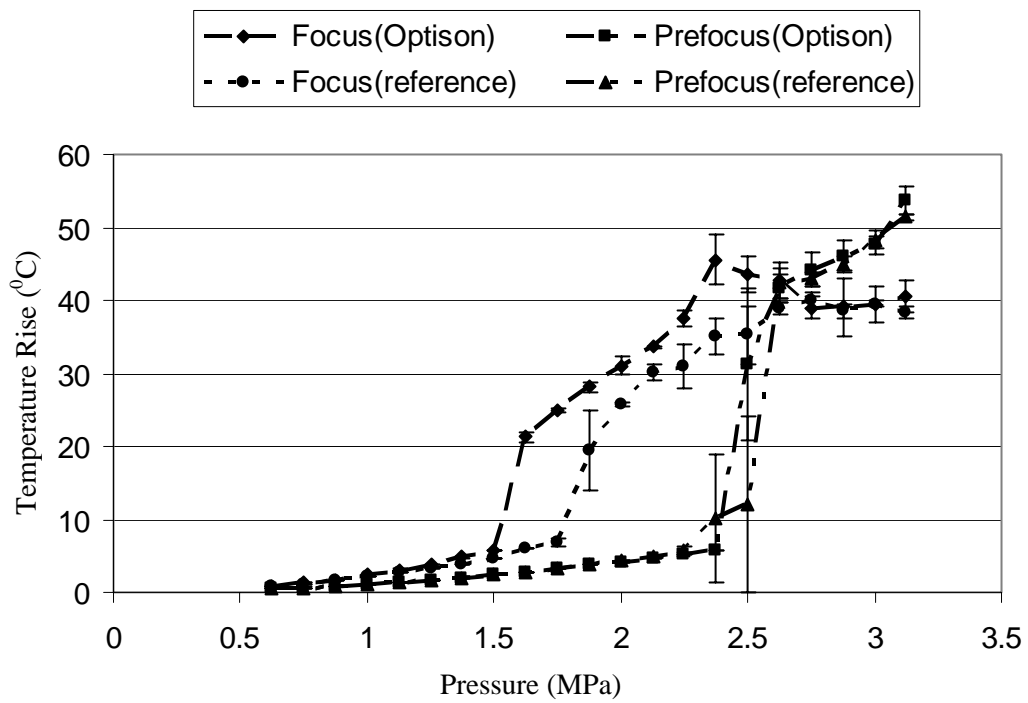
Figure 4.9b Temperature measurement results with a single wire at micron bubble concentration 500-800/μL
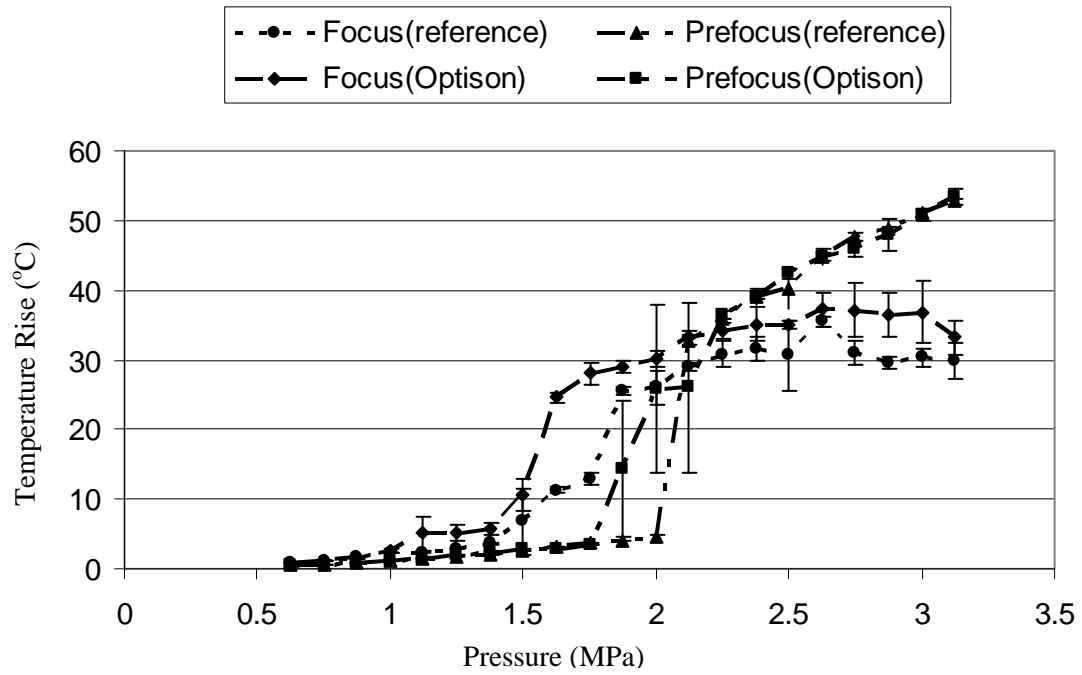
Figure 4.10a Temperature measurement results with multiple wires at micron bubble concentration 50-80/μL
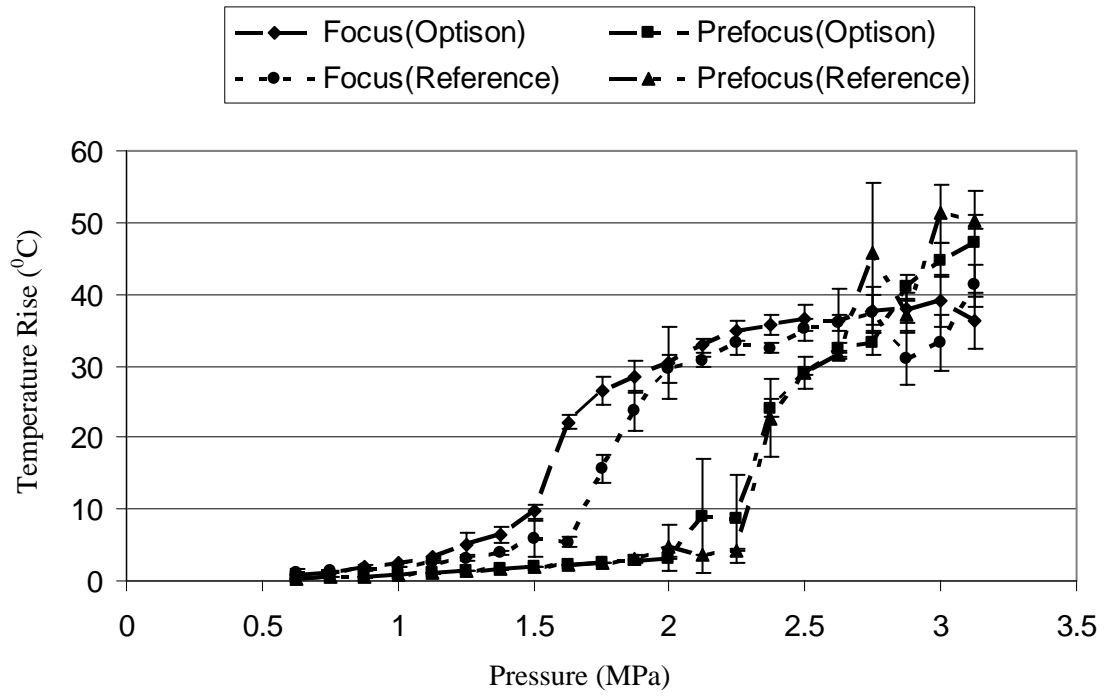
Figure 4.10b Temperature measurement results with multiple wires at micron bubble concentration 500-800/μL
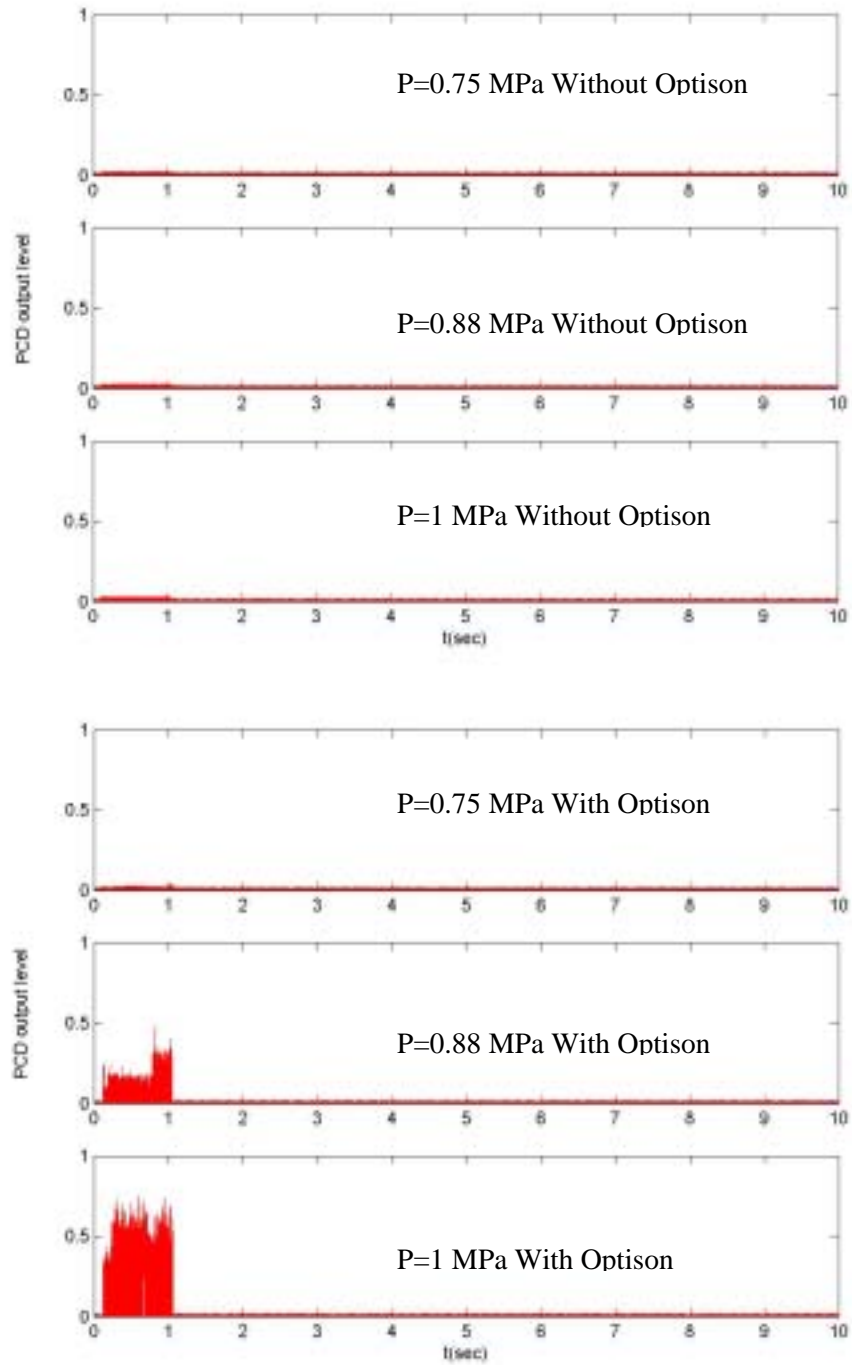
Figure 4.11 The PCD output with and without Optison for different diving pressures: 0.75 MPa, 0.88 MPa and 1 MPa

Chapter 5

Simulation results and the comparison between the model predictions and the experiments

We now are aware of the bubble dynamics in this region. The analysis of the heating mechanism in Chapter 3 allows us to estimate the heating during the HIFU exposure. Also, we have shown experimental results in Chapter 4. One of the goals of this project is to predict the temperature rise in the tissue phantom. In this chapter, we predict the temperature by solving the BHTE and estimating Q using the knowledge of bubble dynamics. The temperature measured with thermocouples will be corrected for the thermocouple artifact in this chapter.

The total scattering-cross section of the bubbles will be calculated, which is directly related to the dissipated energy. And at low gas volume fraction, (this is likely to be true as we will show the results of low fitted bubble densities in the tissue phantom), we treat all bubbles as isolated. Thus the primary pressure field will not change, and the energy deposition due to the presence of these bubbles can be easily calculated as a summation of that of all the bubbles. The temperature rise in the sound field can be obtained through numerical solution of the BHTE. The bubble number is determined by fitting the experimental data.

A very important phenomenon in high intensity focused ultrasound is the occurrence of shielding at high intensity. To model this, an effective absorption coefficient due to the presence of the cavitation is evaluated. The modeling of the shielding requires the recalculation of the sound field by using an effective absorption coefficient. The current FDTD code is not the most suitable algorithm for modeling the shielding due to the limitation of the computational time;

119

however, the results for energy deposition can still give us some valuable insight into this problem.

5.1 General considerations

A single bubble as a heating source can be easily calculated. However, bubble-enhanced heating during HIFU exposure is certainly caused by bubble populations, thus the heating caused by multiple bubbles has to be evaluated. We still do not know the bubble numbers in the focal region; however, previous work in our group [44][48] estimates the bubble number in the focal region to be on the order of 20. This means the gas volume fraction of the focal region is very small and on the order of 10^{-4} (the focal volume of our HIFU transducer is about 10 μl). This result suggests to us that, at least as far as bubble dynamics is concerned, the single bubble theory is appropriate. Thus in our simulations, the interaction between individual bubbles will be ignored. The unknowns in this simulation are the bubble number and the bubble locations in the focal region. The bubble number is basically determined by the number of nuclei of sufficient size in the tissue phantom. Our tissue phantom is a homogenous material, so it is natural to assume cavitation nuclei are homogenously distributed. Cavitation is caused by the negative swing of the acoustic pressure, so we are going to use the peak negative pressure as the cavitation threshold variable. The threshold value is measured from experiments. Once the focal pressure increases beyond the threshold value, cavitation will occur at that region. The homogenous distribution of nuclei will yield a homogenous distribution of bubbles in that region.

The nonuniform driving pressure profile at the focal region yields a distribution of bubble dynamics and thus a heating source distribution. Finally, to match the measured temperature in experiments, we have to deal with the problem of the thermocouple artifact. Also the introduction of the thermocouple may decrease the cavitation threshold. And most likely cavitation is formed

at the surface of the thermocouple; this will affect the assumption of the homogenous distribution of the cavitation nuclei. But the thermocouple only occupies a small volume, and so we ignore this perturbation.

We will start this chapter by presenting the cross-section and energy deposition due to single bubble.

5.2 Cross sections

Scattering cross section

As we have shown in Chapter 3, the enhanced heating due to cavitation mainly comes from viscous heating and radiation heating. We are going to focus on the radiation heating first in this section. A way to measure the strength of the scattering from an oscillating bubble is to calculate the scattering cross section, which is defined as the ratio of the scattered power to the incident intensity [15],

$$\sigma_{sc} = \frac{W_{sc}}{I_{inc}}, \tag{5.1}$$

where W_{sc} is the scattered power, I_{inc} is the incident intensity, and σ_{sc} represents the scattering cross section. I_{inc} and W_{sc} can be determined from the formulae in Chapter 3.

The scattering cross section is an important indicator. Large σ_{sc} means more energy is taken out of the incident wave which will have a chance to be preferentially reabsorbed by the medium. Thus the local power deposition is going to increase and therefore additional temperature rise is going to be induced. The magnitude of the scattering cross section is decided by the nature of the cavitation. Inertial cavitation has a much larger scattering cross section than noninertial cavitation. Here we show the results of scattering cross section as a function of bubble equilibrium radius R_0 in Figure 5.1a and 5.1b. The driving pressure is 2 MPa and the viscosity is

fixed at 0.005N.s/m^2 and 0.05N.s/m^2. In both cases, the scattering cross section has a maximum value in the small bubble region and then decreases as the bubble size increases. This corresponds with our knowledge that bubbles which are just larger than the critical radius, which is defined by the Blake threshold, oscillate inertially and therefore have a large scattering cross-section. The scattering cross section for viscosity 0.005N.s/m^2 is two orders larger than that of viscosity 0.05N.s/m^2. This indicates bubbles scatter much more energy when oscillating in a less viscous medium. We also observed that the oscillation of the values of the scattering cross-section occurs in the chaotic region.

Extinction cross section

Large scattering cross section means a large "acoustic radiation heating". Viscous heating also plays a role in this heating problem. The energy loss due to radiation and viscous damping together can be taken account of by the extinction cross section, which is very similar to the scattering cross section but includes the effect of viscous damping (thermal damping is ignored):

$$\sigma_{ext} = \frac{W_{ext}}{I_{inc}} \tag{5.2}$$

where W_{ext} is the power loss due to scattering and viscous damping at the bubble surface, and σ_{ext} is the extinction cross section.

A plane wave of intensity I_{inc}, traveling a distance Δz through a population of N_b bubbles per unit volume, each having an extinction cross section σ_{ext}, has its intensity reduced by $\Delta I = -N_b\sigma_{ext}\Delta z$. Then integration gives [15]

$$I = I_0 \exp\left(-N_b\sigma_{ext}z\right) \tag{5.3}$$

where I_0 is the intensity at z=0. Thus the extinction cross section indicates the total acoustic energy loss due to the presence of a bubble. Here we show the extinction cross section as a

function of bubble equilibrium radius in Figure 5.2 for viscosity 0.05 N.s/m^2 and 0.005 N.s/m^2 at p_a=2.0 MPa. All the parameters are the same as those used in the plot for scattering cross section. In the high viscosity case, although the scattering cross section is smaller than the small viscosity case, the extinction cross section is much larger, and the maximum value occurs at a larger bubble radius. This is because the high viscosity suppresses the inertial oscillation of the bubble and increases the viscous damping loss.

5.3 Power deposition

To evaluate cavitation heating, first, the results for power deposition in the current parameter space are calculated. The power deposition results can be used to calculate the heating source term Q in the bioheat transfer equation. Some similar results for power deposition have also been showed by Edson [48].

Power deposition due to radiation

The total radiation power deposition for a 1-µm bubble at driving pressure of 2 MPa is shown in Figure 5.3 as a function of viscosity and distance from the bubble. The total deposited radiation power is defined as the power loss, *i.e. E_0-E_{sac}* (See Chapter 3). The driving pressure is 2 MPa.

In general, large radiation power deposition occurs in the small viscosity region, and the peak is around 0.008 N.s/m^2. For a fixed viscosity, the radiation power deposition asymptotes very quickly. This indicates most of the radiation energy is absorbed within 1 mm from the bubble surface.

Figure 5.4b shows a mapping of total radiation power deposition in the viscosity and bubble equilibrium space. The distance from the bubble is fixed at 1 mm, and the driving pressure is 2 MPa. The biggest energy deposition occurs in the small bubble size and small viscosity

region, which is the region just above the Blake threshold. As the bubble gets bigger and enters the resonance region, power deposition is moderate. And as the bubble is even larger, the oscillation becomes linear, and radiation energy deposition becomes very small.

The deposited radiation power is also shown in Figure 5.5 for two fixed viscosities: 0.005 N.s/m^2 and 0.05 N.s/m^2 as a function of r, the distance away from the bubble surface, and R_0, the bubble equilibrium radius. At low viscosity, for all R_0, most of the radiation power is dissipated within 1 mm. For high viscosity, the radiation power deposition exhibits linear behavior, that is because the lack of nonlinear components in the scattered sound by these bubbles. However, at high viscosity, viscous heating is dominant, and the radiation heating can be ignored compared to viscous heating. Therefore, the total deposited radiation power within 1 mm from the bubble surface will be used to calculate temperature as the contribution from the radiation part.

The heating source term Q due to radiation heating is also showed in Figure 5.6 for two different viscosities. Since heating is directly related to the total deposited power, similar results are obtained here. Once again, at high viscosity, the heating source term, which is due to radiation heating solely, is at least 1 order lower than that of the low viscosity case.

Power deposition due to viscous damping

We showed the power deposition due to viscous heating. Viscous heating occurs near the bubble surface and then the heat is conducted through the medium. The viscous heating rate will depend on how big the bubble surface area. In Figure 5.4a we show the power deposition due to viscous heating in the viscosity and bubble equilibrium radius parameter space. The largest viscous heating happens for large bubbles and high viscosities. Compared with the radiation heating results, viscous heating has a maximum value in the small radiation heating region. On

the other hand, radiation heating achieves its maximum value at the small viscous heating region. The maximum values of both are on the same order.

5.4 Temperature rise enhanced by bubbles

Now we start to use the current model to predict the temperature rise inside our tissue phantom. The whole process for the prediction was described in Chapter 3. Several assumptions need to be established before starting this simulation:

1). Once the pressure reaches the cavitation threshold (experimentally determined), bubbles are assumed present, and the initial bubble size is determined by the Blake threshold.

2). After cavitation occurs, bubbles will grow until they hit either the shape instability threshold or the rectified diffusion threshold which depends on the viscosity of the tissue phantom.

3). If the bubble hits the shape instability threshold, it is will break up; we assume 1 fragment of the same initial size survives, thus the total bubble number remains constant.

4). If the bubble hits the rectified diffusion threshold, it will be trapped there and oscillate at a constant size.

5). If we only consider the viscous heating of cavitation, every oscillating bubble in the tissue phantom is like a point source. The conduction inside the tissue phantom will smooth the temperature. We are going to use average values for viscous heating in the bubble region

The validity of 1) and 2) have been discussed in Chapter 2. Assumption 3) is likely to be true in an average sense. After a bubble breaks up, it may break into pieces larger than the initial size, and then it will take a shorter time for it to expand. These pieces will merge together to become one bubble. They yield more heating at the beginning; the merge, however, is going to allow these bubbles to jump to a bigger size and decrease the growing time. So on average,

assumption 3) actually may give an equivalent value for the heating. The validity of 4) is assured by the definition of the rectified diffusion threshold. The validity of 5) depends on the speed of heat conduction. At 1 MHz, the thermal diffusion length $\sqrt{D_0/2f}$ is 0.6 μm, and thus is large enough for heat to conduct through the local region at a time scale of milliseconds.

Temperature rise below the cavitation threshold

Before we present the results of cavitation-enhanced heating, we first examine the temperature rise induced by HIFU in the low intensity region, i.e., below the cavitation threshold.

We have shown the temperature rise data in Chapter 4. Below the cavitation threshold, the induced temperature is actually quadratic in the local driving pressures, as we showed in the Chapter 3. However, we must correct the temperature measurement by accounting for the thermocouple artifact. We are going to correct this effect by adopting an effective local absorption coefficient, and we have described the whole procedure in detail in Chapter 3. The effective local absorption coefficient we measured through the rate of linear heating method at the beginning of the heating is 96.9 Np/m. The local area we set to this absorption coefficient is shown in Figure 5.7. Figure 5.8a shows one example of the agreement between the simulation and the measurement. A 3D temperature code is used to simulate this temperature rise. The simulation results, with thermocouple artifact correction and without thermocouple artifact correction, are also shown in Figure 5.8b and c, respectively. The measurement results using the 125μm thermocouple are shown in Figure 5.8b. Since the large viscous heating at the thermocouple surface, the results without the correction are much smaller than the measurement. But the good agreement is obtained after employing the thermocouple artifact correction. As we discussed before, using very small thermocouples can also reduce the thermocouple artifact. The results measured by a smaller thermocouple with 12.5 μm diameter are shown in Figure 5.8c.

And as we expected, a good agreement between the measurement and the simulation is obtained in Figure 5.8c for pressure below the cavitation threshold, where no correction is applied.

Temperature rise above the cavitation threshold

Due to the thermocouple artifact, we are unable to measure the undisturbed temperature rise in the tissue phantom. We presented the temperature rise below cavitation threshold in the tissue phantom using data corrected for the thermocouple artifact by the method presented above. For the temperature rise above the cavitation threshold, the same ideal is used. To simulate the effect of the thermocouple artifact, we assume that the cavitation induced energy depositions are proportional to the absorption coefficients, i.e., the ratio between the energy depositions without and with thermocouple is equal to the ratio between the absorption coefficient of the tissue phantom and the effective absorption coefficient in the thermocouple region.

Two unknowns we will need in the simulations are the bubble number and the viscosity. We are going to show the results for different viscosities, and fit the bubble number to match the temperature data measured in experiments.

Figure 5.9 shows a typical simulated heating curve with a bubble density of 2.7/μL at the focal region. The viscosity using in this simulation is 0.005 kg/(m·s), which corresponds to the viscosity of human blood. The driving pressure is 2 MPa. In the heating phase (the first 1 second), good agreement is obtained between the measured data and the corrected simulation result. Some disagreement is observed in the cooling stage. We think this disagreement is due to the heat conduction through the thermocouple wire and the finite heat capacity of the thermocouple wire. In the heating stage, since the whole thermocouple probe is heated up, the heat conduction through the thermocouple wire will affect the temperature at the rear of the probe, and the very tip of the probe is actually protected and will not be affected by this conduction. The cooling stage,

however, will be affected by this conduction. The finite heat capacity and conduction of the thermocouple wire will always have an effect on the measurement.

We now will present the simulation results and compare with the experimental measurements. The first correction result is for the temperature measurement of a 100% air concentration sample. The results for two fixed viscosities are presented, 0.005Ns/m^2 and 0.05Ns/m^2. Figure 5.10 is an example of the simulation result and the required bubble number is presented in Table 5.1.

To get undisturbed temperature, i.e., without the thermocouple in place, we simply set the effective absorption coefficient in the tissue phantom everywhere the same but keep the bubble density unchanged. An example of this result is shown in Figure 5.10. We see a large difference between the measurement and the TC-corrected result. When the thermocouple is not there, the largest temperature rise is only about 10 ^{o}C, which is much less than the 60 ^{o}C measured by the thermocouple measured at p_f=2.8MPa. Even though the temperature rise is much lower, it is still much higher than the temperature rise caused by the primary acoustic field alone. One point we want to emphasize is that the resulting enhanced heating is related to the absorption coefficient of the tissue phantom. If a more absorptive tissue phantom is used, then one should expect a much larger enhanced heating.

The results for a 100% air saturated tissue phantom are presented in Table 5.1. For both viscosities, as the driving pressure increases, the bubble density required to match the measured temperature decreases. In general, the high driving pressure should nucleate more bubbles. The reason we think that most likely can account for this counter-infinitive prediction is that shielding occurs even at this low void fraction. The shielding effect can cause a low bubble density in two ways, 1) when shielding occurs, the pressure in the focal region is going to decrease, and this will decrease the bubble density; 2) at low driving pressures, bubble oscillations will be less violent.

Assuming the primary field is unchanged and using the unchanged driving pressure to calculate bubble heating and match the measurements will cause the observed decrease in the predicted bubble density. The prediction of shielding is a complicated problem, and we are going to present a simple model for it in the last section of this chapter.

There is a large decrease in bubble density from 1.57 MPa to 1.68 MPa. The reason for this is due to the choice of the cavitation threshold. In simulations, we use an experimental determined threshold value. In reality, the cavitation threshold should be a region, not just a single value. Cavitation may already occur before this value, but we can not measure it since either its signal is too weak to measure, or the pressure step in experiments is too big to catch this critical value, or both. Therefore, the use of the threshold may cause the cavitation region to be smaller in simulation than reality. This difference will affect the bubble density at low pressures but not at high pressures since once the cavitation region is getting bigger, this difference will be negligible.

Table 5.1 Required bubble densities for a 100% air saturated tissue phantom to match the temperature measurement

Focal Pressure (MPa)	Interpolated Measured Temperature Rise (^{o}C)	Required Bubble Density (μl^{-1}) ($\mu=0.005$ N.s/m^2)	Required Bubble Density(μl^{-1}) ($\mu=0.05$ N.s/m^2)
1.57	27.0	10.5	60
1.68	31.6	4.7	12
1.79	35.3	3.3	5.4
1.90	38.6	3	5.1
2.01	42.3	2.7	4.3
2.12	44.8	2.4	3.7
2.23	46.9	2.5	3.1
2.34	49.6	2.4	2.8
2.45	53.1	2.4	3
2.55	55.6	1.9	2.7
2.66	56.8	1.7	2.7
2.77	58.6	1.3	2.6

In Table 5.2, we present the results for temperature rise after thermocouple artifact correction. Compared to the measured temperature rises, these temperature rises are much lower. However, compared to the temperature rise induced by the primary field, a larger temperature rise is observed, which is due to the enhancement by cavitation. As we pointed out previously, the heating in the tissue phantom is also related to the absorption coefficient. The tissue phantom we used here only matches the lower limit of the absorption in human tissue. Therefore, a much higher temperature due to bubble-enhanced heating is expected in real tissue.

To reach the same temperature requires more bubbles when the viscosity is 0.05 $N.s/m^2$ than if the viscosity is 0.005 $N.s/m^2$. This is determined by the bubble dynamics. At low viscosity, due to the shape instability threshold, bubbles are limited to small size, which happens to correspond to the maximum radiation heating. At high viscosity, bubbles are bounded by the rectified diffusion threshold at a relative large size of ~20 μm, near where the viscous heating is dominant. The maximum radiation heating has the same order as the viscous heating, however, bubbles can not reach the maximum viscous heating region due to the rectified diffusion threshold. Therefore, at low viscosity, bubbles likely have higher heating rate and a smaller bubble density is required.

We also show the same results for 20% saturated air concentration. The measured values we used are the data for a 24% saturation phantom. These results are presented in Table 5.3 and Table 5.4. For this low air concentration phantom, the required bubble density also roughly decreases as the pressure increases, but the trend is not as big as the saturated sample. This may indicate that the shielding effect is not as strong as the saturated sample due to fewer bubbles being present in this case.

Table 5.2 The temperature (at focal plane off-axis 0.5 mm) in the tissue phantom after correcting the thermocouple artifact for a 100% air-saturated tissue phantom. Bubble densities are the same as Table 5.1 for each pressure.

Focal Pressure (MPa)	Temperature Rise without cavitation (^{o}C)	Calculated Temperature Rise (^{o}C) (μ=0.005N.s/m^2)	Calculated Temperature Rise (^{o}C) (μ=0.05N.s/m^2)
1.57	1.12	7.94	21.4
1.68	1.29	6.71	8.45
1.79	1.46	6.94	6.45
1.90	1.65	7.37	7.5
2.01	1.85	7.42	8.21
2.12	2.07	8.1	8.39
2.23	2.29	9.85	8.83
2.34	2.52	10.5	9.02
2.45	2.77	11.5	10.4
2.55	3.03	11.4	10.5
2.66	3.30	11.8	11.2
2.77	3.58	11.5	11.5

Table 5.3 Required bubble densities for a 24% air saturated tissue phantom to match the temperature measurement

Focal Pressure (MPa)	Interpolated Measured Temperature Rise (^{o}C)	Required Bubble Density (μl^{-1}) (μ=0.005N.s/m^2)	Required Bubble Density(μl^{-1}) (μ=0.05N.s/m^2)
1.57	7.95	1.1	5
1.68	8.56	0.3	0.5
1.79	8.42	0.1	0.2
1.90	25.3	1.7	2.1
2.01	41.1	2.7	3.1
2.12	40.7	2.2	3.1
2.23	38.4	1.9	2.8
2.34	38.8	1.8	2.1
2.45	40.2	1.5	1.8
2.55	43.7	1.3	1.7
2.66	50.3	1.4	2.1
2.77	56.5	1.3	2

To investigate the effect of viscosity on the bubble number, we presented the required bubble density for different viscosities at a driving pressure of 2 MPa in Table 5.5, where D_b represents the bubble density. It is very clear that different viscosities have different effects on the

required bubble density and therefore the resulting temperature. This is expected due to the variation in bubble motion with viscosity. The maximum difference between the resulting temperatures is around 1.5°C, and this can be treated as the uncertainty in the temperature due to the uncertainty in the viscosity.

Table 5.4 The temperature (at focal plane off-axis 0.5mm) in the tissue phantom after correcting the thermocouple artifact for a 24% air saturated tissue phantom. Bubble densities are the same as Table 5.3 for each pressure.

Focal Pressure (MPa)	Temperature Rise without cavitation (°C)	Calculated Temperature Rise (°C) ($\mu=0.005$N.s/m^2)	Calculated Temperature Rise (°C) ($\mu=0.05$N.s/m^2)
1.57	1.12	1.98	3.33
1.68	1.29	1.77	1.5
1.79	1.46	1.78	1.75
1.90	1.65	4.88	4.75
2.01	1.85	7.3	7.45
2.12	2.07	7.47	7.65
2.23	2.29	8.04	7.25
2.34	2.52	8.48	7.26
2.45	2.77	8.32	8.05
2.55	3.03	8.81	8.42
2.66	3.30	10.4	10.4
2.77	3.58	11.5	10.9

Table 5.5 Required bubble densities for different viscosities for a driving pressure of 2 MPa, in a 100% air saturated tissue phantom. Temperature rise after thermocouple artifact correction is also shown. The measured temperature rise is 42.3°C.

μ(N.s/m^2)	0.001	0.003	0.005	0.007	0.009	0.01	0.03	0.05	0.07	0.09
D_b(μl^{-1})	2.9	2.5	2.7	3	3.3	3.5	5.8	4.3	2.9	2.6
Temperature Rise (°C)	7.34	8.19	7.42	8.58	8.73	8.87	7.74	8.21	7.93	7.69

5.5 A preliminary of prediction of shielding

The results we showed above have indicated the importance of the bubble shielding effect. To predict bubble-enhanced heating correctly, we have to deal with the shielding effect.

Bubble shielding involves multiple scattering, the interaction between bubbles, etc, and is a very complicated phenomenon. In this section, we try to use a simple model to predict this problem. We certainly do not expect the problem can be solved here; however, we hope this model can serve as a good start to the solution of this complicated problem.

In general, the presence of a bubble population in a sound field will cause a change in the attenuation and sound speed of the medium. We try to evaluate the change of these two properties and then investigate the shielding effect. The effective absorption coefficient can be evaluated through the calculation of the extinction cross section, as discussed in Section 5.1. This means the local effective absorption coefficient is going to be a time-dependent function. We are going to use Wood's equation to predict the sound speed, which has the following form [119][120],

$$\frac{1}{c_{mlf}^2} = \frac{(1-\chi)^2}{c_l^2} + \frac{\chi^2}{c_g^2} + \chi(1-\chi)\frac{\rho_g^2 c_g^2 + \rho_l^2 c_l^2}{\rho_l \rho_g c_l^2 c_l^2} \tag{5.4}$$

where c_l is the sound speed in liquid, c_g is the sound speed in gas, ρ_l and ρ_g are the density of the liquid and gas respectively, χ is the void fraction and c_{mlf} is the sound speed in the mixture, where 'lf' means low frequency, limited to frequencies below the resonance frequency of the bubbles.

Since we deal with strongly nonlinear bubbles, the void fraction is actually also a function of time. To make this problem simpler, we use a time-average bubble volume to obtain an average void fraction,

$$V = \left\langle \frac{4}{3}\pi R(t)^3 \right\rangle_t \tag{5.5}$$

Also the equilibrium size of the bubbles is limited to small size compared to the linear resonant size, which is required by Wood's equation.

There are several kinds of model to simulate the pressure field. One suitable acoustic model is a layer-by-layer model which allows us to simulate the sound field layer by layer, and

the local absorption coefficient and sound speed can be changed with each layer. Another model is our FDTD code which is probably a better tool for the prediction of shielding. In FDTD code, the pressure field is calculated from time point to time point. When cavitation occurs, the induced effective absorption and sound speed are going to change with time, and that will cause a redistribution of the local pressure field and again, cavitation may occur in new areas, and existing cavitation may cease or continue to grow under the new driving pressure. As we pointed out at the beginning of this section, this is going to be just a start to solve a very complicated problem, and we are going to make it simple. Only the energy distribution at some certain time is simulated due to the limitation of the available computation time.

Figure 5.11 is the heating source term for 2 μm bubbles and the peak pressure is 3.1 MPa at the focal region. Sound speed c and absorption coefficient α are evaluated for a driving pressure of 1.6 MPa and are assumed uniform in the focal region in order to avoid numerical discontinuity. Two bubble densities are used here. At 20/μl, only a small shift is observed (keep in mind, the real focus is at 62 mm). When bubble density is increased to 40/μL, much more energy is deposited in the prefocal region. The viscosity for this case is 0.05 N.s/m^2.

Figure 5.12 is another example for viscosity 0.005N.s/m^2 and with roughly the same peak pressure. The comparison is between the same bubble densities but different bubble sizes. Shielding happens at the large bubble size.

The prediction for cavitation enhanced-heating including shielding is a very complex problem. We here only show some simple results, and many assumptions are used to simplify the prediction and decrease the computation time. A more accurate model requires taking account of the strong nonlinearity of the bubbly liquid, which is beyond the scope of the current work.
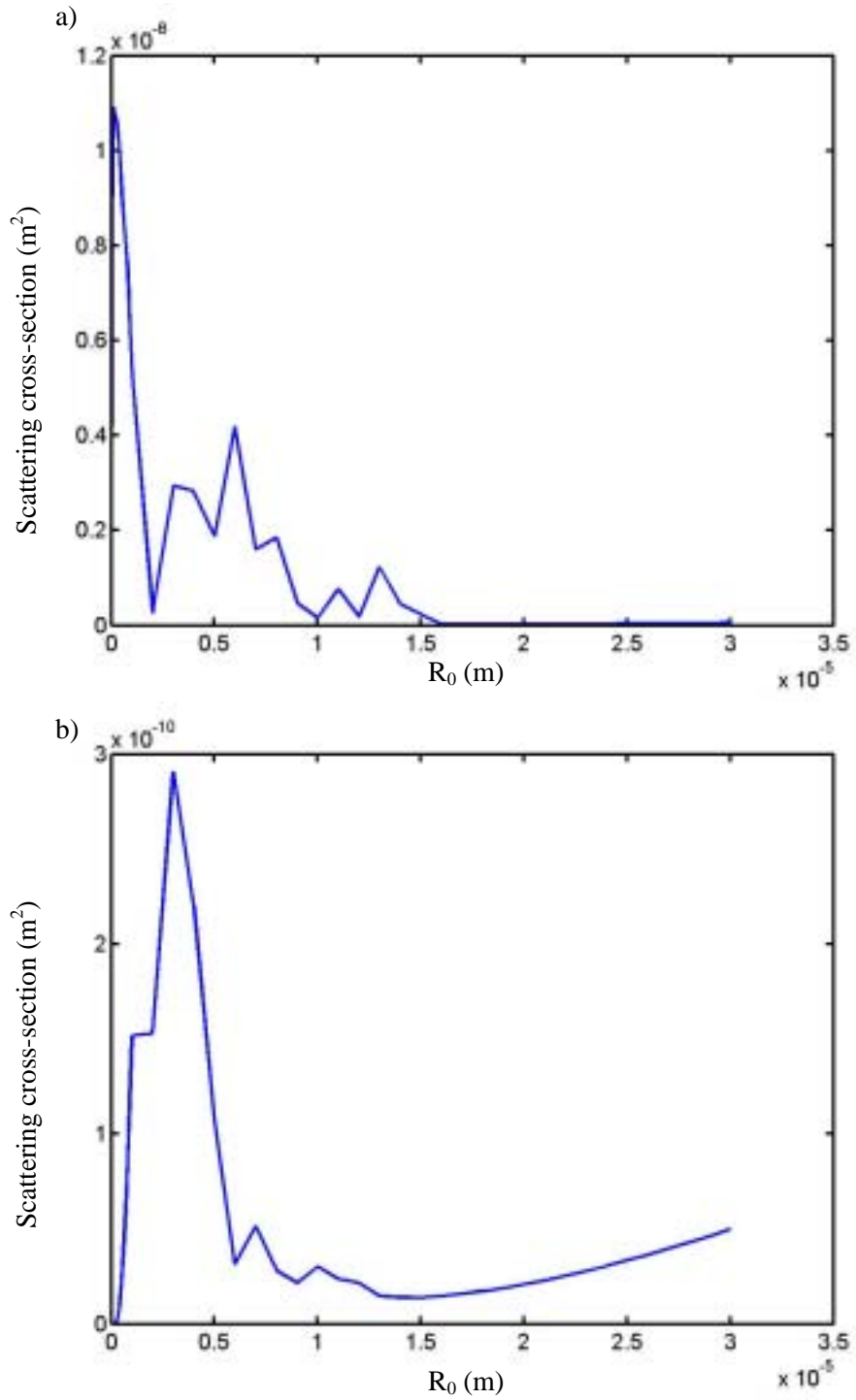
Figure 5.1 Scattering cross-sections for different viscosities at driving pressure 2 MPa, a) 0.005 N.s/m^2 and b) 0.05 N.s/m^2
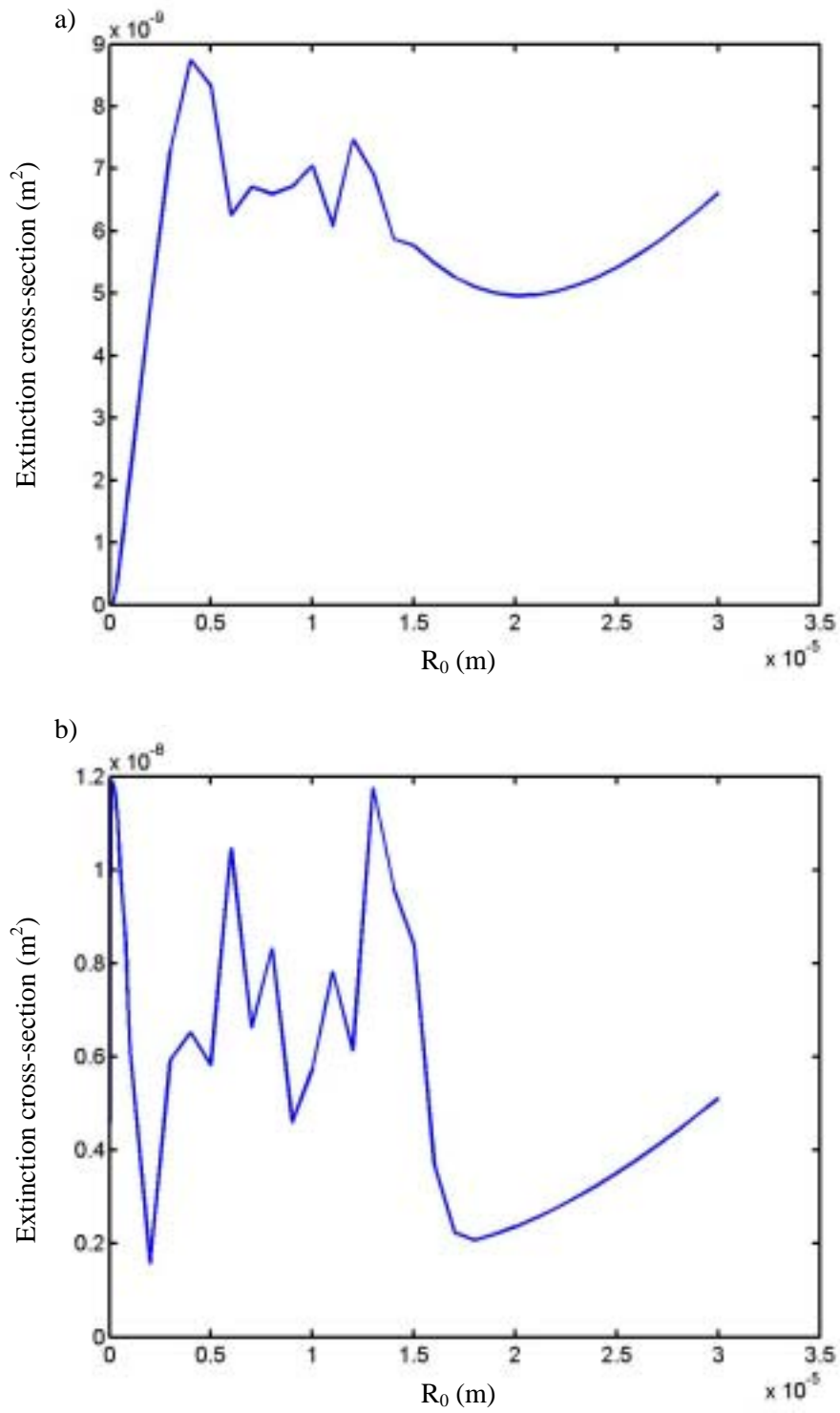
Figure 5.2 Extinction cross-sections at driving pressure 2 MPa for viscosity a) 0.005 N.s/m^2 and b) 0.05 N.s/m^2.
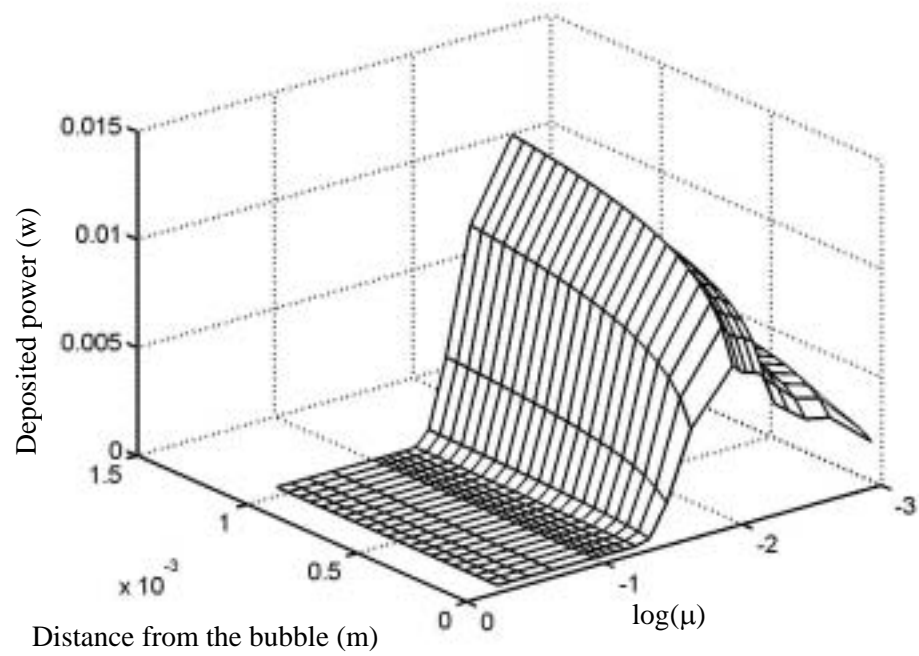
Figure 5.3 Total radiation power deposition for a 1 μm bubble as a function of viscosity and the distance from the bubble surface. Driving pressure 2 MPa. The unit of μ is N.s/m^2.

a)

b)
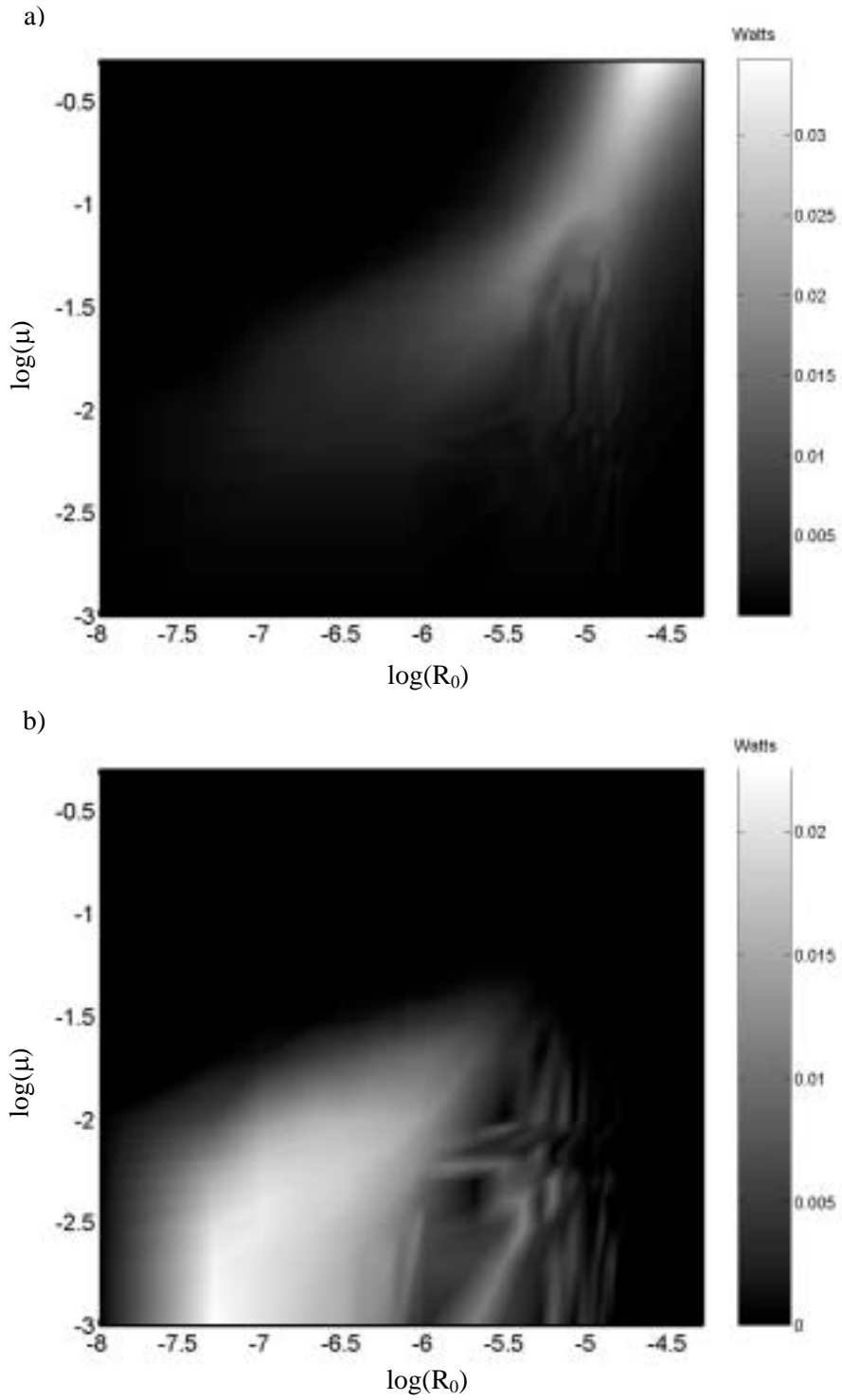
Figure 5.4 Power deposition in the parameter space of viscosity and R_0 at 2 MPa. a) Viscosity power deposition; b) Radiation power deposition within 1mm from the bubble surface. The unit of μ is N.s/m^2 and the unit of R_0 is m.
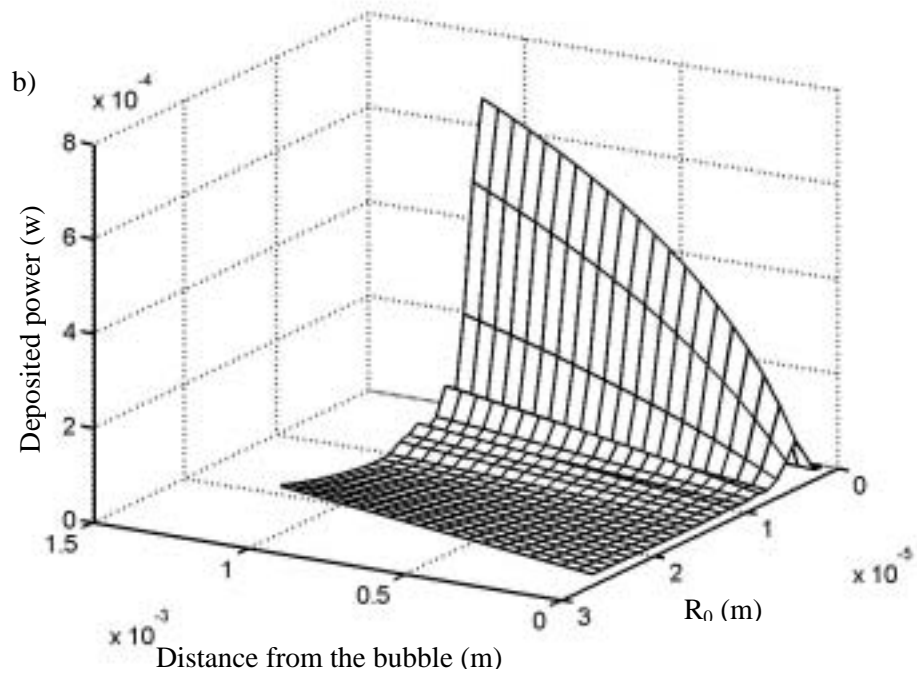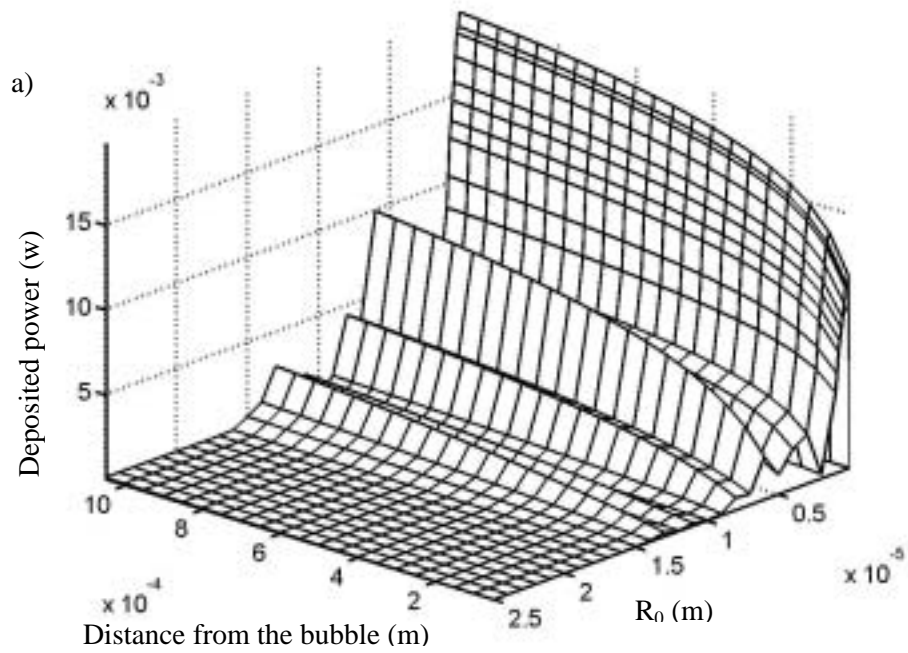
Figure 5.5 Total radiation power deposition as a function of R_0 and he distance from the bubble surface. a) $\mu=0.005$ N.s/m^2, b) $\mu=0.05$ N.s/m^2. Driving pressure 2 MPa.

a)

b)
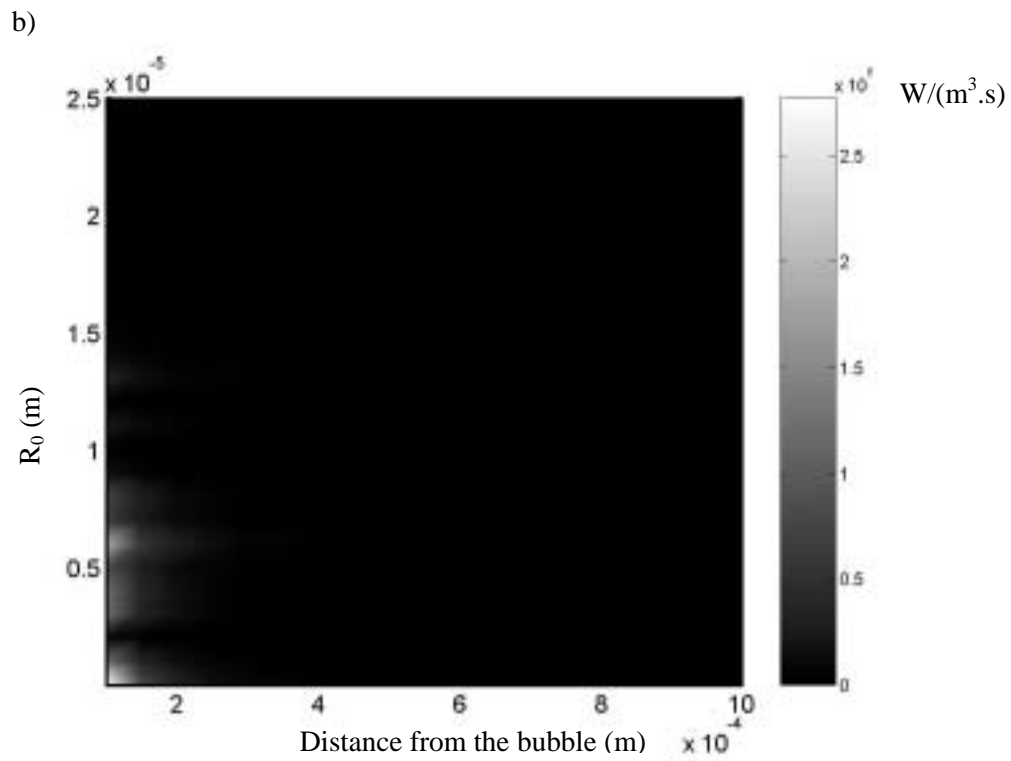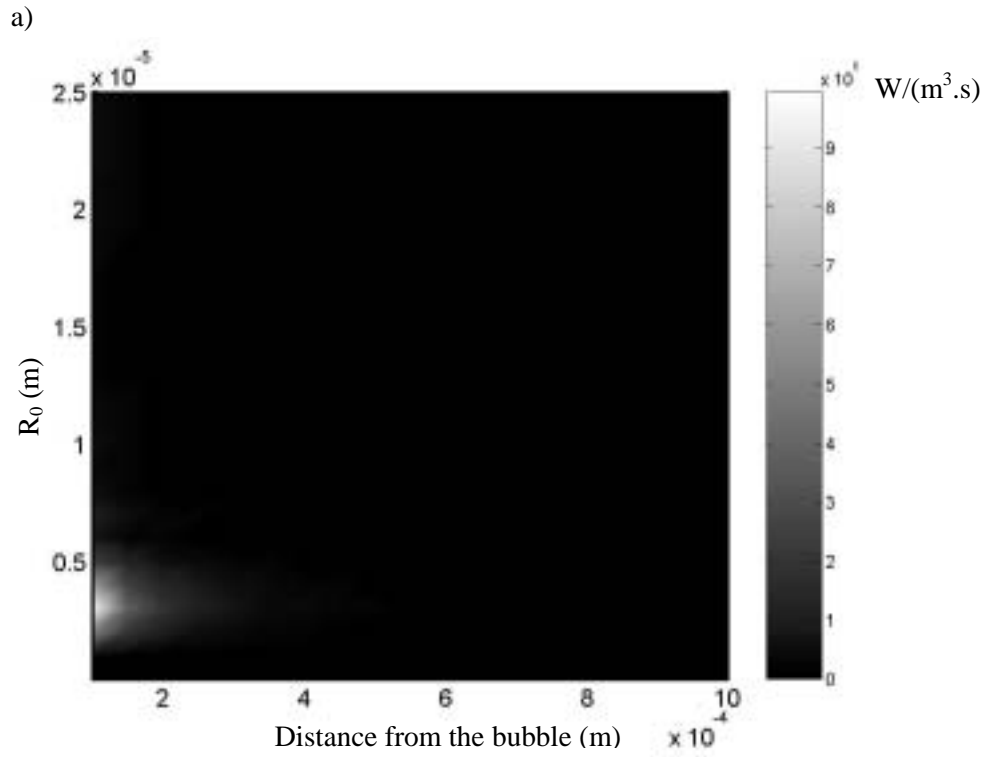
Figure 5.6 Radiation heating source term in the BHTE at driving pressure 2 MPa for a) μ=0.05 N.s/m^2, b) μ=0.005 N.s/m^2

140
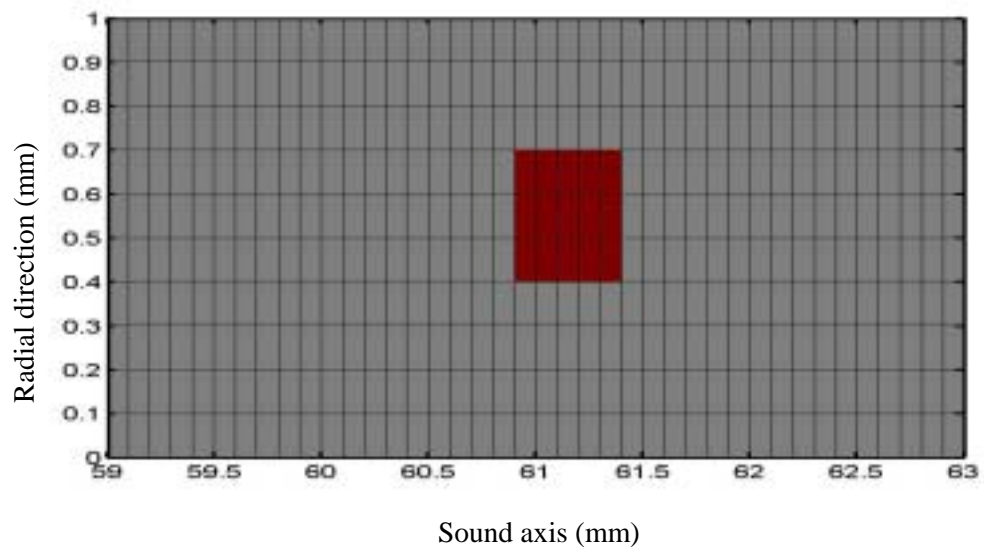
Figure 5.7 The area for the effective absorption (dark area).

a)

Time (s)

b)

c)
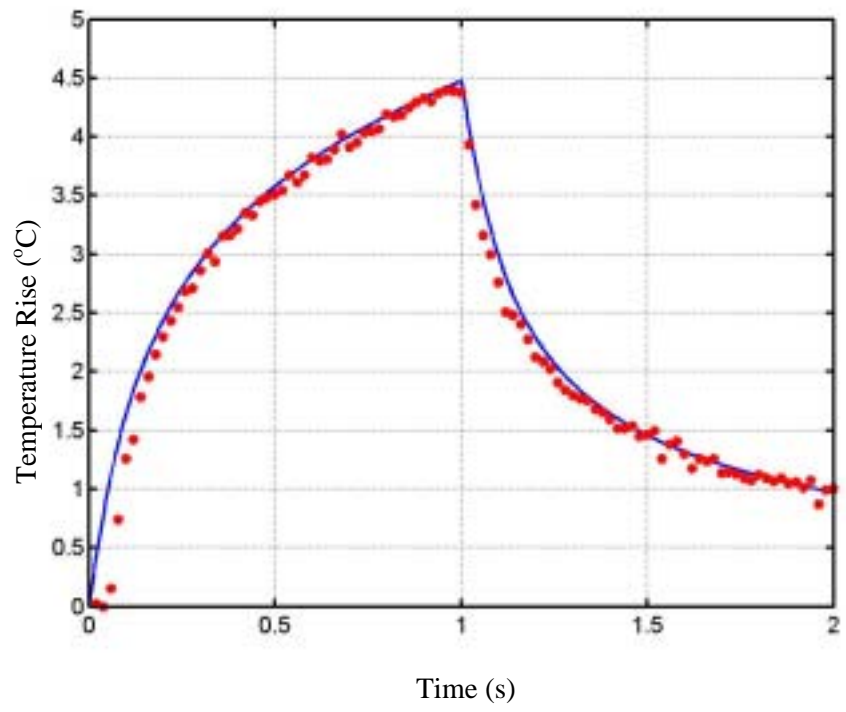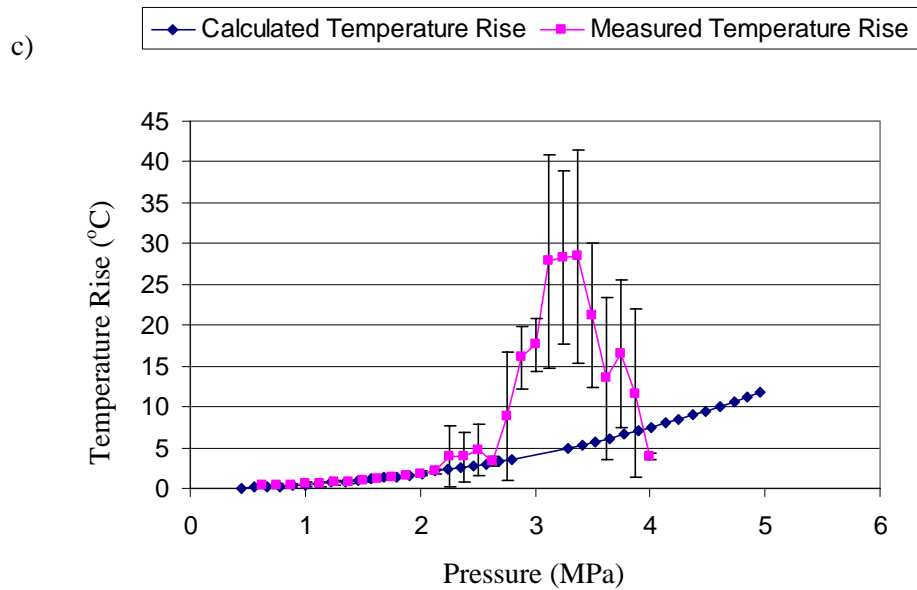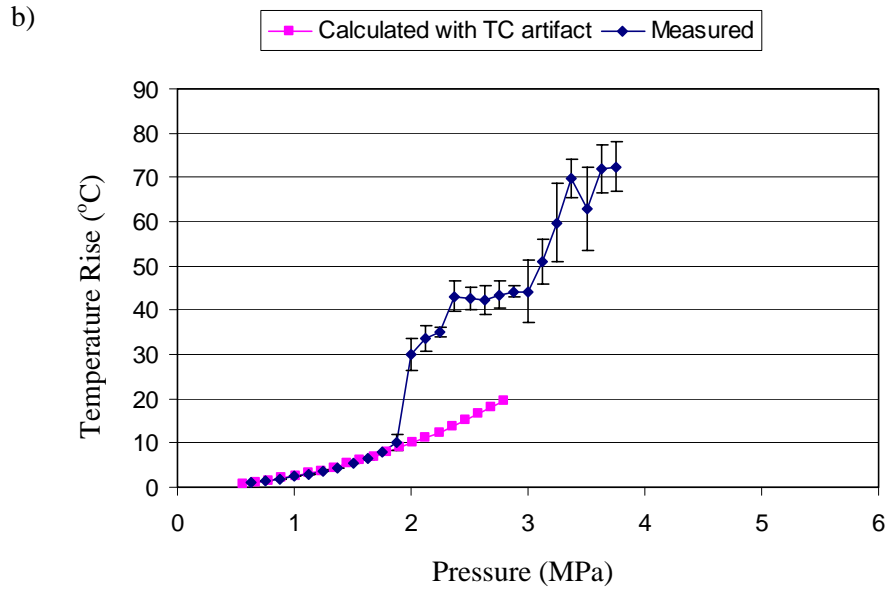
Figure 5.8 The comparison between the measurements and simulations. a) the comparison of the time heating curve between the measurement (dot) and the simulation (solid line) at 1.375 MPa peak pressure b) the comparison results between the measurement by a 0.125 mm thermocouple and the simulation after thermocouple couple artifact correction; c) the comparison results between the measurement by a 0.0125 mm thermocouple and the simulation without the thermocouple artifact correction; pressure.
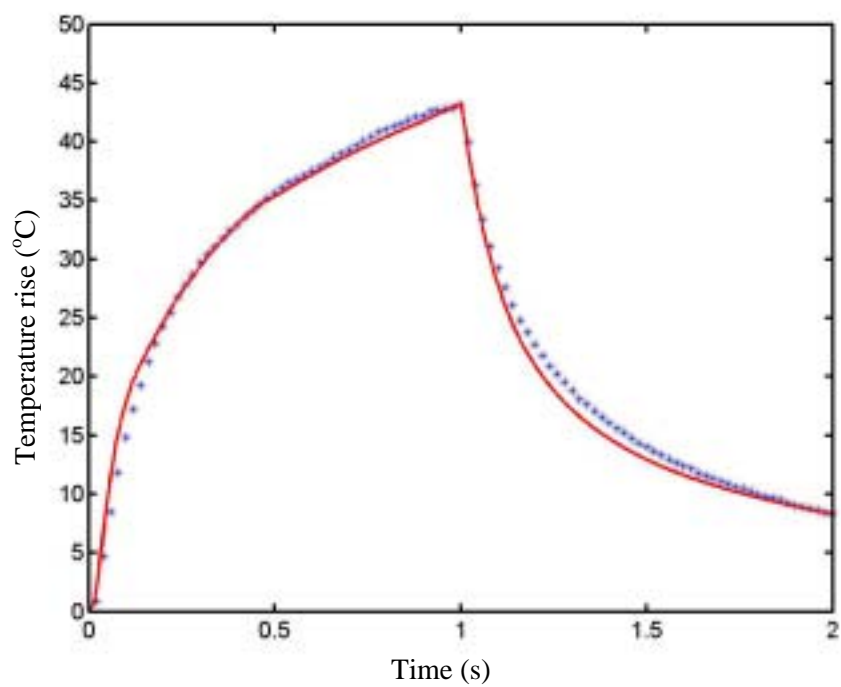
Figure 5.9 A comparison between the measured temperature (dash line) and the simulation (solid line). Driving pressure is 2 MPa and gas concentration 100%. Viscosity is 0.05 N.s/m^2 and the bubble density is 2.7/μL.
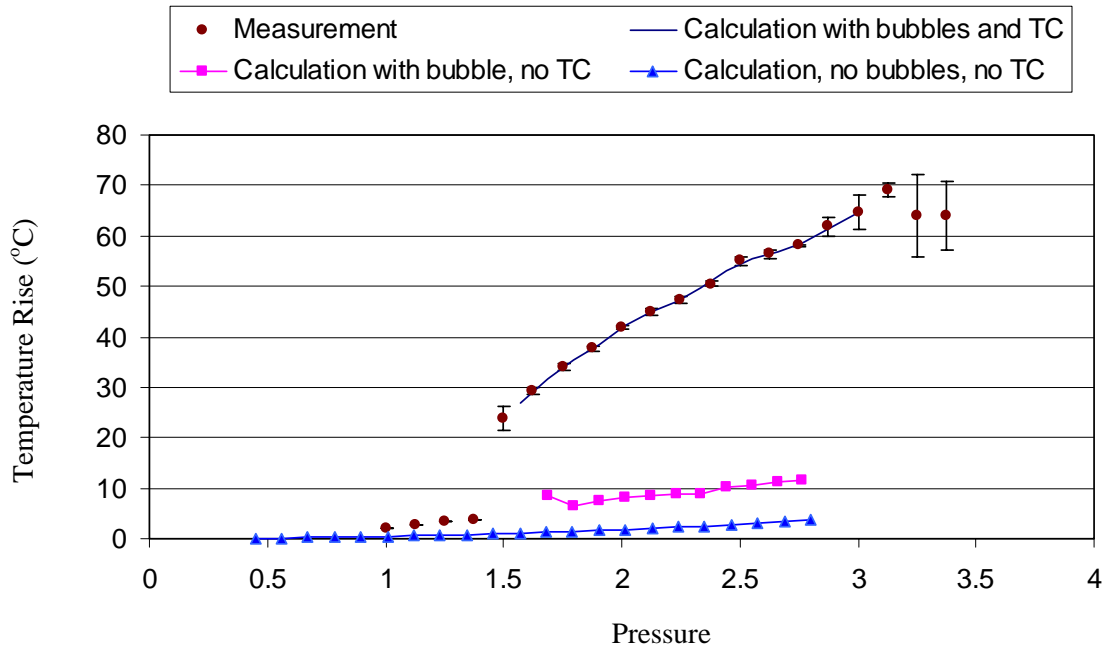
Figure 5.10 The comparisons between temperature measurement and simulations. There are measurement results for a 100% gas concentration samples and three simulation results. First temperature rises are simulated with thermocouple artifact correction and the required bubble densities are obtained, which is the matching result of the FDTD simulation. Then temperature rises are simulated assuming no thermocouple but with cavitation, which can be compared to the temperature simulation results without cavitation. The viscosity is $0.05 N.s/m^2$ in simulations.
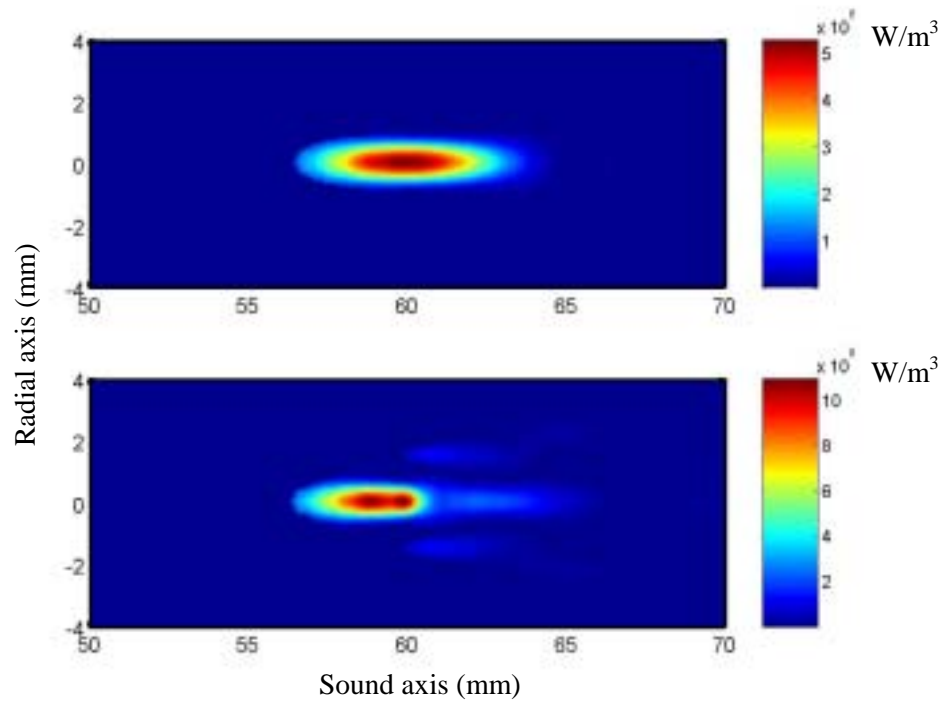
Figure 5.11 Intensity depositions distribution for different bubble densities, 20 bubbles/μL (top plot) and 40 bubbles/μL (bottom plot). $R_0=2$ μm. The peak negative pressure is 3.1 MPa without cavitation. Viscosity 0.05 N.s/m^2.
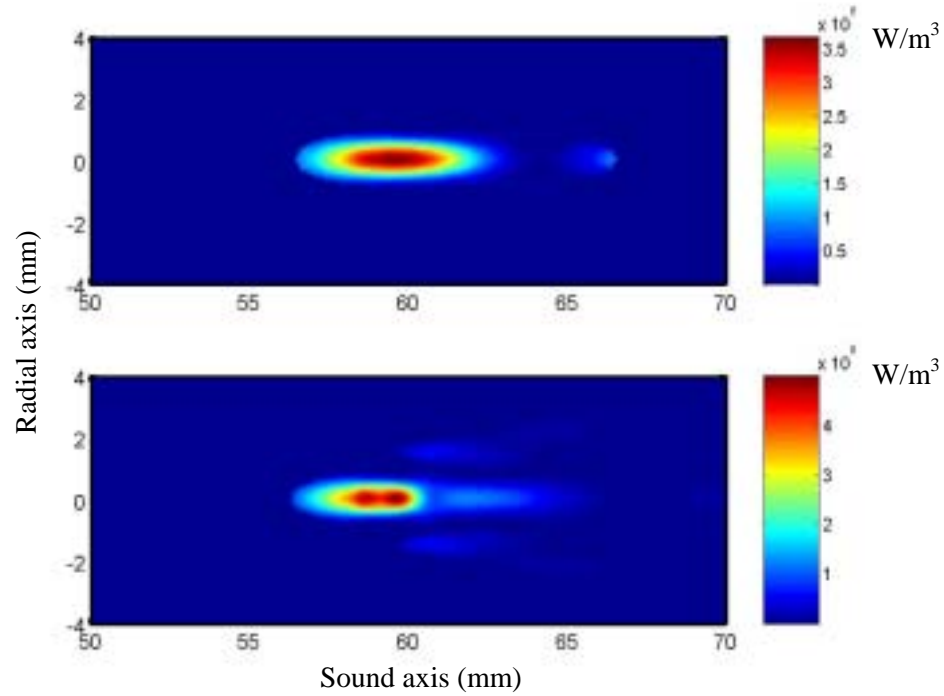
Figure 5.12 Heating source term Q distributions at a bubble density of 10 bubbles/μL. Bubble size are 0.1 μm (top plot) and 0.2 μm (bottom plot). The peak negative pressure is around 3.1 MPa is without cavitation. Viscosity 0.005 N.s/m^2.

Chapter 6

Summary and discussion

In this work, we have shown theoretical and experimental work related to bubble-enhanced heating in a tissue-mimicking material. Our results included analysis of the bubble dynamics in a parameter space of bubble equilibrium radius and viscosity; a clear scenario about bubble motion in high intensity focused ultrasound is given, which will help us understand cavitation behavior in a tissue. In addition, results for heating due to bubbles are presented. Theoretical and experimental work are combined in order to search for appropriate parameters to control cavitation-related heating and improve predictability for ultrasound therapy in the future.

6.1 The summary of theoretical results

A primary contribution concerning bubble dynamics in HIFU in this dissertation is a qualitative understanding of the evolution of the bubble size distribution. In the regime of high intensity focused ultrasound, cavitation-related bubble oscillations become very complex due to strong nonlinearity and complex material properties of the tissue. We use a Newtonian bubble dynamics model to study bubble behavior in this region. A large range of viscosity used to capture all the likely bubble motions. Two important threshold values are investigated: the bubble shape instability threshold and the rectified diffusion threshold.

When cavitation occurs in HIFU, the first issue we are concerned with is the stability of the micro-bubbles, or whether these micro-bubbles can survive at all in the ultrasound field. Certainly, how long these micro-bubbles can survive is related directly to the sound field. If no

bubbles can survive in the sound field, then cavitation is not going to affect the sound field or it will have a negligible effect at most. The rectified diffusion threshold is another important boundary for the bubble oscillation. The bubble equilibrium radius is a primary parameter which can determine the characteristics of bubble oscillations. The rectified diffusion threshold tells us the eventual fate of any possible bubble equilibrium radius, whether it will grow or dissolve in the sound field. These two threshold values bound the possible bubble size distributions in the HIFU regime. Only shape stable and non-dissolving bubbles can contribute to the heating.

Another contribution made in this work is the calculation of the growth rate of HIFU bubbles. As we just discussed, the determination of the bubble equilibrium radius is important. Different bubble sizes have different dynamic behavior and thus will have different effects on the primary sound field and heating results. In HIFU, all the bubbles are created from some tiny nuclei. As we showed in Chapter 2, when bubbles are first created, they grow extremely fast but slowly grow more when they get bigger. Besides the determination of the bubble equilibrium radius, the growth rate results may also answer the question of the cavitation nucleation threshold. For nuclei to grow to become free bubbles, a positive growth rate is necessary. Then the positive slope of the rectified diffusion threshold or "the unstable equilibrium" part of the rectified diffusion threshold may indicate the cavitation threshold. When nuclei are at that size, cavitation is going to be possible.

Based on the bubble dynamic results, a theoretical heating model is built. The energy deposition is calculated for the HIFU parameter space. Only radiation heating and viscous heating are taken account of in this work. The radiation heating and viscous heating are dominant in different regions of the parameter space. Radiation heating is dominant when bubble size is small and viscosity is low; however, for big bubbles and large viscosity, viscous heating is dominant. The maximum values of these two heating mechanisms are of the same order. By using this

result, along with the time-dependent bubble size and the boundaries predicted by the shape instability threshold and the rectified diffusion threshold, the bioheat transfer equation was solved and compared to the experimental results.

The bubble density which can match the experimental result was predicted by assuming there was no interaction between bubbles. The predicted bubble densities decrease as the driving pressure increases. This result seems counter-infinitive: as driving pressure increases, there should be more bubbles in the same region since more and smaller nuclei will cavitate. The reason for this anomaly is not clearly. However, the shielding effect of multiple bubbles could explain the result by keeping the focal pressure low. We proposed a simple bubbly liquid model to explain the shielding effect, incorporating both the shift in sound speed and additional attenuation. The results suggested the shielding effect could happen for a relatively low void fraction (<1e-4). Treating the presence of cavitation as the increase of the attenuation alone, other researchers [47] found that the shielding effect may only occur at very high pressure. But here we found once the change of the sound speed is taken into account, the shielding effect can occur at relative low pressure and bubble densities.

6.2 Summary of experimental results

Three experimental results are presented in this dissertation. The first is a measurement of the harmonic emission from the tissue phantom. We observed the subharmonic, second harmonic and other higher harmonics and ultraharmonics, which are correlated with the peak temperature jump. Since the subharmonic signal is believed to be a unique feature of inertial cavitation, this result is another piece of evidence relating the heating to the bubbles. Moreover, since we can observe a subharmonic signal only by lowering the viscosity of the tissue phantom, the tissue phantoms we used in most of the experiments would seem to have a very high viscosity.

The second experimental result we showed is the peak temperature rise as a function of dissolved gas concentration. The amount of dissolved gas in a tissue affects the nuclei size and number, and the growth rate of bubbles. From our result, an increase in dissolved gas concentration has two notable effects: a) to decrease the observed cavitation threshold; b) to cause the bubble-enhanced heating to become much more repeatable. Bubble oscillations are deterministic (except at nucleation and break-up), and bubble-enhanced heating should exhibit this intrinsic order and allow us to explain and finally control this heating behavior. Since there are enough nuclei inside the tissue phantom at high dissolved gas concentrations, we may nucleate the same amount of bubbles in the ultrasound field when repeating the same insonation conditions, and thus obtain roughly the same peak temperature rise. In the case of low gas concentrations, there are not enough nuclei and not enough dissolved gas to grow many bubbles, so cavitation activity will be more sporadic and less repeatable from run to run. Thus the peak temperature rises will also vary.

Finally we showed the result of heating enhanced by micro-bubble based contrast agents. One way to control the heating is to control the bubble size and density in the tissue phantom. Contrast agents are micro-bubbles which are in clinical use and may be the only possible way to introduce preexisting bubbles into the human body. The purpose of this experiment is to investigate the possibility of heating using contrast agents. We do observe enhanced heating when contrast agents are used. In the case when contrast agents are used, we observed two temperature jumps, and only one temperature jump when contrast agents are not used. When the driving pressures are higher than the inertial cavitation threshold of the contrast agents, the first temperature jump is observed. And when the driving pressures continue to increase and exceed the inertial cavitation threshold of the tissue phantom, a second peak temperature jump is observed. The enhanced heating between the first and second peak temperature is solely the

151

inertial oscillating contribution of the contrast agents. When the driving pressures are higher than the inertial cavitation threshold of the tissue phantom, the peak temperature rises when contrast agents are used are always higher than the peak temperature rises without contrast agents until the saturation region is reached. With the two sample concentration we used, we did not observe any obvious differences. This is not unexpected since the input total energy is constant in one insonation, there must be a limit for temperature rises.

6.3 Suggestions for future work

We have yet to achieve a complete understanding of bubble-enhanced heating in HIFU. Theoretically, the effect of viscosity needs to be fully investigated. We used a Newtonian model to investigate the bubble dynamics. We know however those real tissue materials are viscoelastic. We investigated a large range of viscosity to try to cover all the possibilities. However, how good (or bad) this approach is needs to determined, and this requires a new non-Newtonian bubble model [121][122]. Another difficulty related to this problem is that the viscoelastic material properties of the tissue phantom we used, and tissue in general, are not easy to obtain.

Another theoretical task is to further develop the bubbly liquid model we presented in the last section of Chapter 5. Our results shown that introduced the single bubble model is not sufficient to simulate the bubble oscillations in the HIFU regime, since shielding may occur during the insonation even at low driving pressures. The model we presented in Chapter 5 is a low-frequency linear approximation, and we used the average void fraction during the nonlinear oscillations. In the future, one must employ a bubbly liquid model which can take of account the strong nonlinearity of bubbles. Of course, the viscoelastic problem is coupled to this bubbly liquid model too.

Other suggestions for theoretical work include taking account of the nonlinearity of the thermal conduction. Also, the model we used for bubble dynamics assumes the clean bubble, and no surfactant transport problem was considered. In really tissue, bubble surface may be dirty and that will affect the bubble dynamics results since dirty bubble in general intend to be more stable. This may be useful to be investigated in the future.

Experimentally, we have made a prediction about bubble numbers, and some form of bubble imaging experiment would be very useful result to compare with our simulation results. If it were possible to image the bubbles in a clear tissue phantom during the insonation, we could directly observe the bubble distributions. High speed imaging could further determine the time evolution of the bubble size. All these results could be used to compare with simulations directly, and that would certainly improve our understanding of cavitation in HIFU.

In all our experiments, the driving frequency and insonation time are constants. In the future, one may vary the insonation time and driving frequency to find the best acoustic parameters in HIFU. Contrast agent-enhanced heating is also worth further investigation since this is an easy way to control the initial bubble size in human tissue, and it is easy to coordinate with contrast imaging techniques.

Appendix A The difference among different radial equations

The first dynamic bubble model dates back to 1917; Lord Rayleigh [58] derived the first simple bubble equation, which was modified thereafter and now is known as the Rayleigh-Plesset (RP) equation [15] The first model by Rayleigh is a very simple model and only holds in incompressible, inviscid fluids, and neglects surface tension. Nowadays, the RP equation has been incorporated with viscous force and surface tension, and also can account for compressibility of the host medium. Other authors have developed similar equations to model bubble dynamics, such as the Keller-Miksis Equation, Herring Equation, Gilmore Equation and Flynn's derivation[60][123][124][125][126] etc. All these are second order temporal equations. For small amplitude oscillations, all the models will give the same results. Differences between the models, however, will be seen in the case of large amplitude oscillation. This Appendix presents a brief discussion of the problem in our case.

In this context, a comparison of Rayleigh-Plesset's, Herring's, Keller-Miksis' and Gilmore's models will be presented.

The "modern form" of the Rayleigh-Plesset equation reads,

$$R\ddot{R} + \frac{3}{2}\dot{R}^2 = \frac{1}{\rho}\left(1 + \frac{R}{c}\frac{d}{dt}\right)\left(p - p_\infty - p_d(t)\right) - \frac{4\mu\dot{R}}{\rho R} - \frac{2\sigma}{\rho R} \tag{A1}$$

where ρ is the density of surrounding media, and p is the internal pressure of the bubble and p_d is driving pressure.

Herring's equation has the form of

$$\left(1 - 2\frac{\dot{R}}{c}\right)R\ddot{R} + \frac{3}{2}\left(1 - \frac{4\dot{R}}{3c}\right)\dot{R}^2 = \frac{1}{\rho}\left(p_B - p_\infty - p_d(t)\right) + \frac{R}{\rho c}\frac{d}{dt}\left(p_B - p_d(t)\right) \tag{A2}$$

where p_B is the pressure on the liquid side of the bubble surface.

We rewrite the Keller-Miksis equation we used throughout this dissertation here,

$$\left(1-\frac{\dot{R}}{c}\right)R\ddot{R}+\frac{3}{2}\left(1-\frac{1}{3}\frac{\dot{R}}{c}\right)\dot{R}^2=\frac{1}{\rho_L}\left(1+\frac{\dot{R}}{c}+\frac{R}{c}\frac{d}{dt}\right)p_B-\frac{1}{\rho}\left(1+\frac{\dot{R}}{c}\right)\left(p_\infty-p_d\left(t+\frac{R}{c}\right)\right)$$

(A3)

These three models are derived for small Mach number.

Another radial equation is the Gilmore equation, which uses the Kirkwood-Bethe approximation. The speed of sound the liquid is a function of the motion in the Gilmore model. The approximation states that for spherical waves of finite amplitude, the quantity $r\phi$ (the product of the radial coordinate and the velocity potential in the liquid) propagates with a velocity equal the sum of the fluid velocity and the local velocity of sound. The Gilmore equation has the form,

$$\left(1-\frac{\dot{R}}{c}\right)R\ddot{R}+\frac{3}{2}\left(1-\frac{\dot{R}}{3c}\right)\dot{R}^2=\left(1+\frac{\dot{R}}{c}\right)H+\frac{R}{c}\frac{dH}{dt}\left(1-\frac{\dot{R}}{c}\right)$$

(A4)

where

$$P=A\left(\rho/\rho_0\right)^m-B,$$

$$H=\int_{P_\infty}^{P(R)}\frac{dP}{\rho},$$

$$c=\left[c_L^2+(m-1)H\right]^{1/2},$$

$$P(R)=P_g-2\sigma/R-(4\mu/R)\dot{R}$$

Here we use $m=7$ and $A=3001\times P_\infty$ and $B=A-P_\infty$, c_L is the small signal sound speed and P_g is the gas pressure inside the bubble. We are going to incorporate these radial equations and Prosperetti's formulation for the internal pressure, which we have used throughout this dissertation, to analyze the differences among these models.

All these models can account for compressibility to the first order in Mach number, and we expect that at low driving pressure and low amplitude oscillation, where the bubble motion is mainly linear, there will not be any significant differences among these models. Discrepancies, if any, should only occur at high driving pressures and large oscillations. High driving pressure and large oscillation are both necessary since in some parameter regions, the bubble motion could be still linear though the driving pressure is high. In the area of single bubble sonoluminescence, researchers have adopted many radial equations to understand the collapse phase of SL, and no significant differences have been reported for these radial equations. We are going to show here first the shape instability threshold predicted by the above four equations.

Figure A1 shows the shape instability thresholds calculated from the four radial equations in the parameter space of SBSL. Here, we just compare the shape instability threshold for mode 2. In the smaller driving pressure region, all the four thresholds agree very well, in the larger driving pressure region, however, we can see some discrepancies. The Gilmore model gives us the lowest threshold, and the Keller-Miksis model predicts a higher threshold, but the Herring's and Rayleigh-Plesset equations predict the highest threshold. On the theoretical grounds, the Gilmore model and Keller-Miksis model are better than Herring's and Rayleigh-Plesset model for large amplitude bubble oscillations [125]. If we compare these thresholds with Holt and Gaitain's shape instability data [65][78], they actually all give us good agreement within the experimental uncertainty. However, these results suggest to us the discrepancies between these models could be getting larger and larger if we drive bubbles very hard, which actually pushes the limits of all these models.

Now let's investigate the bubble dynamics in the high intensity focused ultrasound regime. The shape instability threshold from the Keller-Miksis equation in the viscosity-radius parameter space has been shown in Chapter 3. Here we compare that threshold with one

calculated from the Gilmore equation with bubble radius R_0 from 0.1-1.0 μm. At a driving pressure of 3 MPa, a disagreement between the two thresholds is observed. The discrepancy is even larger for small bubbles than big bubbles. This discrepancy affects our theoretical prediction of heating since it would shift the bubble distribution area for high diving pressure and low viscosity. It is however hard to say which one is better here. Figure A3 shows the $R(t)$ curve and $\dot{R}(t)$ from the Gilmore equation and Keller-Miksis equation for a bubble with R_0=0.5 μm at viscosity 0.001 N.s/m$^{2.}$ If we look at the bubble wall velocity, it already exceeds 10^4 m/s, and this definitely is so large that the assumptions of both theories could not hold. Then it is hard to say which one gives the better result though there are differences.

The bubble shape instability threshold in general can be divided into two kinds: one is the Rayleigh-Taylor (R-T) instability and the other is the parametric instability. Every time the bubble decelerates at the end of a collapse, the R-T instability occurs. An R-T unstable bubble, however, may still survive, as long as the shape perturbation does not break the bubble. A common criterion to determine this is to compare the ratio of the perturbation amplitude due to the R-T instability to the bubble radius; once the ratio is larger than 1, the bubble will break. As we showed in Figure 2.7, during every acoustic cycle, once the bubble collapses, we observe a spike in a_2, and this is caused by the R-T instability.

Another instability phenomenon is the parametric instability which builds up over many cycles. Given a small perturbation at the beginning, it will be enlarged from cycle to cycle and finally break up the bubble. This instability gets its name from the simplest model, in which the linear second order equation for the shape perturbation amplitude possesses time-dependent, periodic coefficients, but is otherwise homogenous. It is thus parametrically excited.

In our current parameter space, most instability behaviors we observed are a combination of R-T instability and parametric instability. As shown in Figure 2.7, the R-T instability occurs in

the first cycle, but the resulting perturbation is not large enough to break up the bubble. After several cycles, however, the perturbation gets larger and larger, and this is characteristic of the parametric instability. Under the coupling action of these two instability behaviors, the initial, small perturbation grows and will finally break up the bubble.

The differences among these radial equations are a function of the bubble wall velocity. They are all derived for small Mach number and only show discrepancies for very strongly nonlinear cases. Different radial equations certainly affect our shape instability results. However, more experimental data are needed to verify which, if any, of these models is quantitatively correct for the violent collapses occurring here.
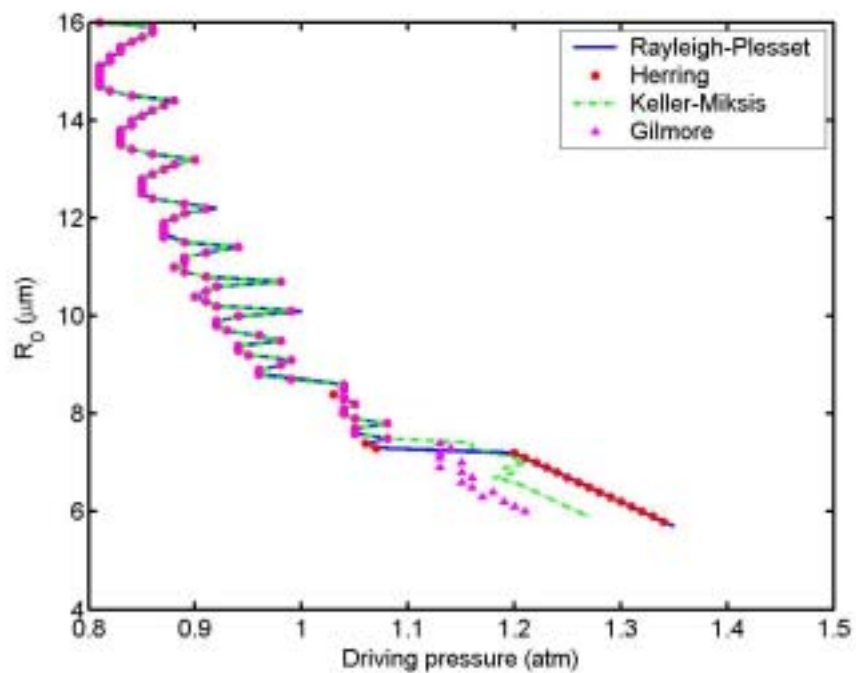
Figure A1 Mode 2 shape instability threshold for four models. For air bubbles in water, driving frequency 20.6 kHz.
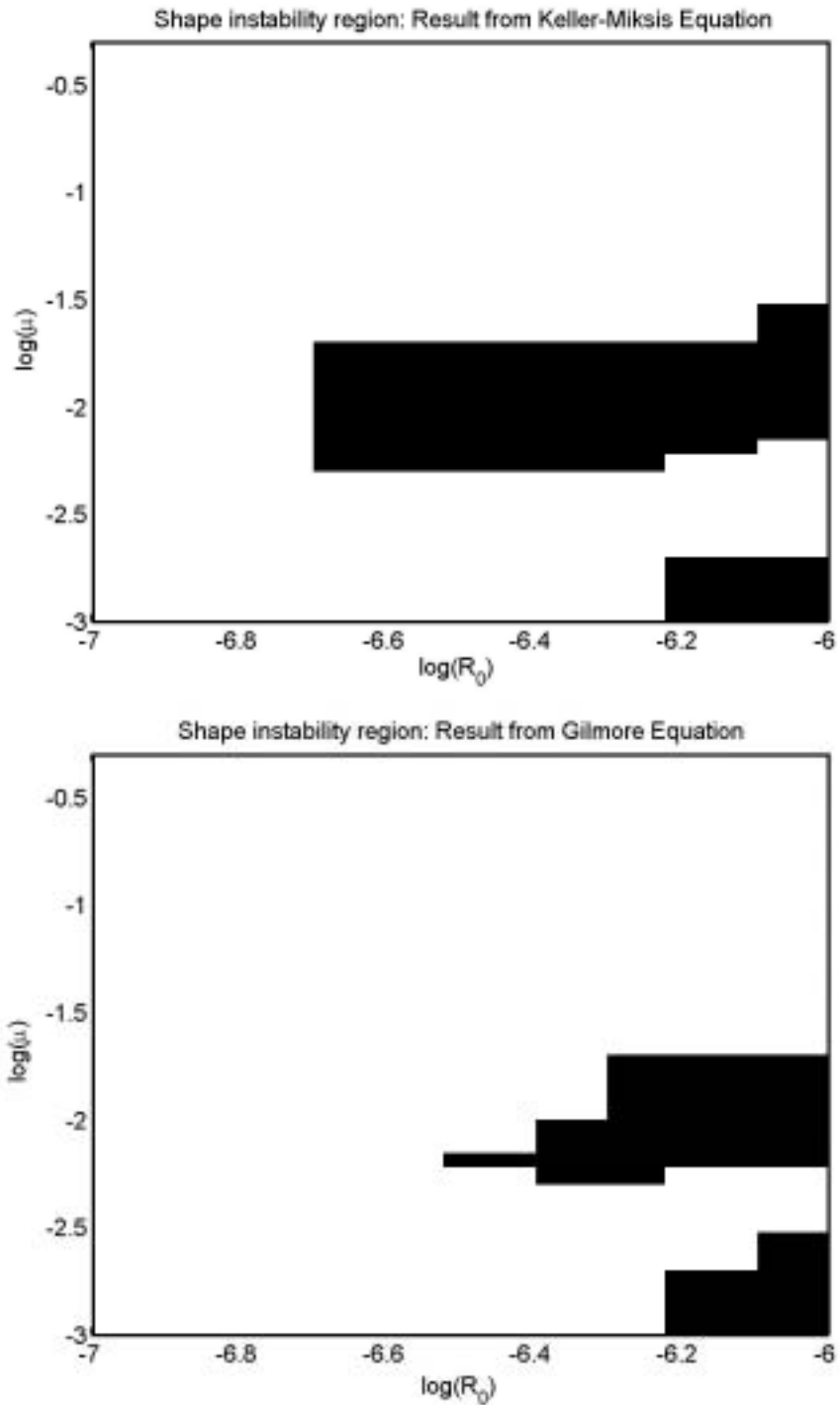
Figure A2 Mode 2 shape instability region from Keller-Miksis equation and Gilmore equation. The dark area is unstable region. Unit of μ is N.s/m^2 and unit of R_0 is m.
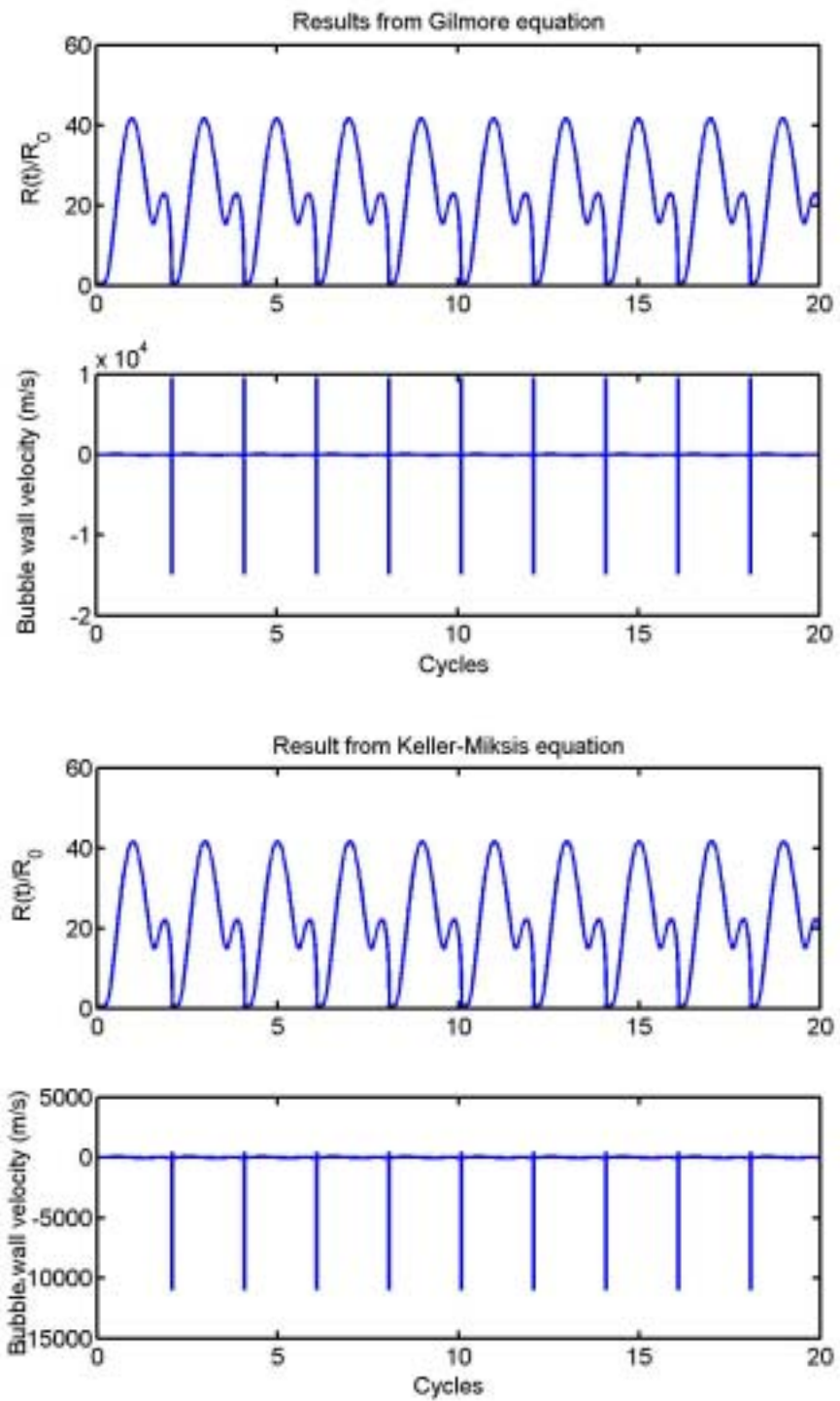
Figure A3 R(t) and bubble wall velocity curve for Keller-Miksis equation and Gilmore equation

Appendix B The nonlinearity of the primary pressure field

There are two motivations for us to investigate the nonlinearity of the primary pressure field in this work: a) In the calibration for the pressure field, we used a linear relation for the transducer and the simulation result of the FDTD code. If the nonlinearity is very strong, then this calibration may cause a large systematic error in the pressure amplitude; b) The FDTD code we used in this work can only account for thermoviscous damping, which has f^2 dependence, here f is the frequency. The attenuation of the tissue phantom we used, however, has $f^{1.1}$ dependence. Only in the weakly nonlinear case, the difference between these two can be ignored.

In this appendix, we will show experimental results of nonlinearity measurements. The same setup was used as that which we described in Chapter 4. We made a cylindrical tissue phantom, which is 40 mm in radius and 22 mm in thickness (In the experiments in Chapter 4, the distance from the tissue phantom surface to the thermocouple probe is about 23 mm). A calibrated PVDF membrane hydrophone (Model 804, Perceptron, Hatboro) is placed at the focus of the sound field, and the tissue phantom is placed before the hydrophone; the distance between the hydrophone and the phantom is 2 mm. A 10-cycle pulse is used to drive the transducer. The output of the hydrophone is directed into the spectrum analyzer, and the peak value of each frequency component is obtained. The results are shown in Figure B1. The measurement indicates the higher harmonic components are much weaker than the fundamental signal. Up to 3.2 MPa, the sound level of the second harmonic component is at least 20 dB lower than the fundamental frequency. Higher harmonic components are even weaker. Thus the energy carried by the higher harmonic components is of the order of 1% of that of the fundamental frequency.

Figure B2 shows the comparison between the pressures measured by the standard hydrophone and the simulation results by the FDTD code. The calibration relation in Chapter 4 is used here. Clearly, as the pressure increases, the discrepancy between measurement and simulation increases. This result qualitatively agrees with the expectation that the f^2 attenuation law in the FDTD code will overestimate the damping of higher harmonics and thus underestimate the total pressure. But in the present range, we still have agreement within 10% at the largest pressure value used in the study.

In the Westervelt equation we used in this work, we omitted the term $-\dfrac{1}{\rho}\nabla p \bullet \nabla \rho$ on the right hand side of the equation, which can account for the effect of density change at the water-phantom interface. The effect on pressure of this omission is shown in Figure B3. We can see this only induces a small correction to the results. In the same plot, we showed the pressure results using a smaller spatial step of 0.05 mm. The use of a smaller step can better account for the generation of the higher harmonic, but only a small effect is seen in the range we are interested in.
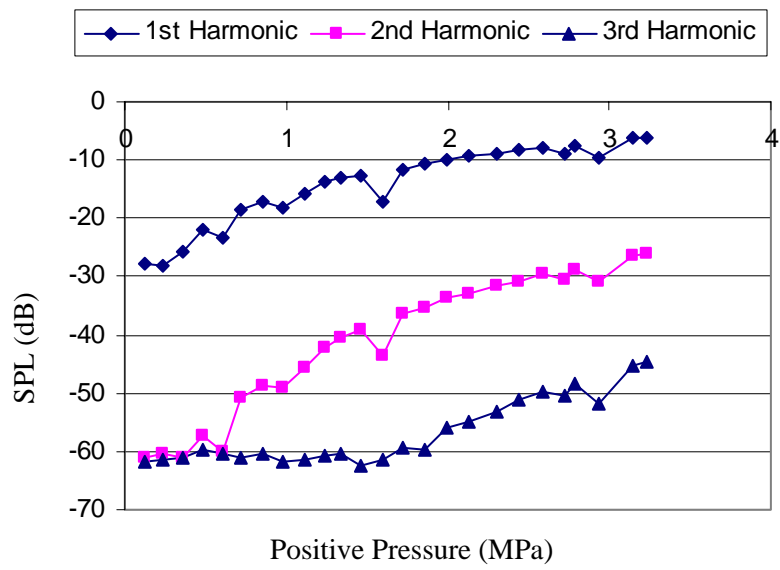
Figure B1 The measured harmonic components after sound passes through a 22-mm thick tissue phantom.
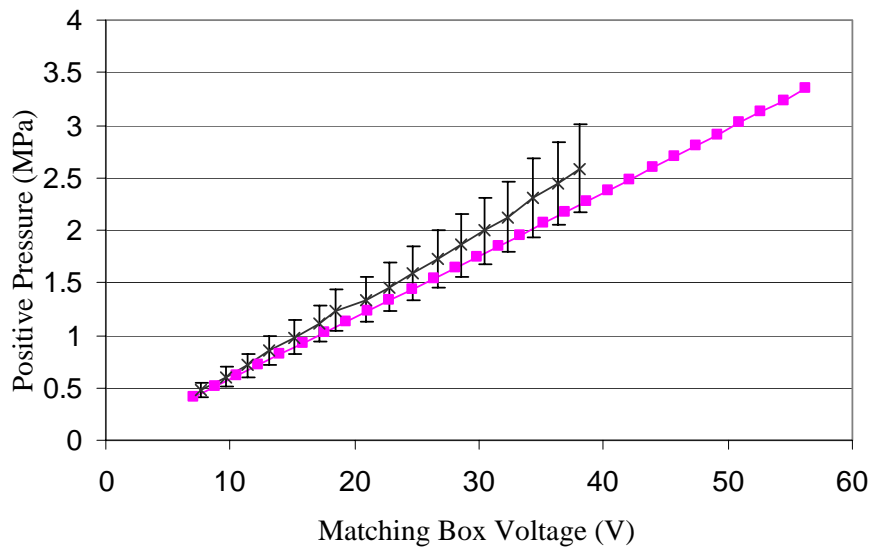
Figure B2 The comparison between the measured pressure and the simulation results. The solid line with error bars are the measurement results. For the simulation results, the matching box voltage is converted from p_0 by equation (4.3).
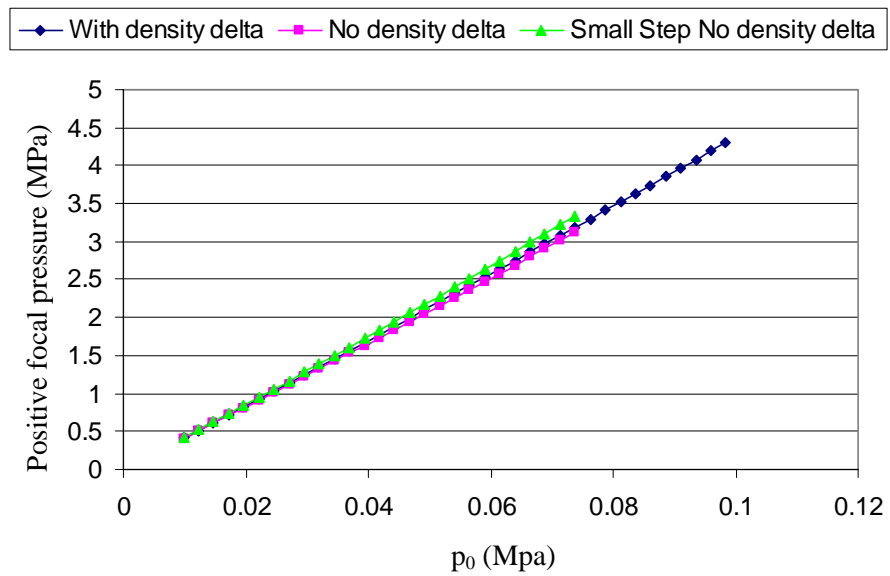
Figure B3 The comparison between the positive focal pressures. These calculations are done with (density delta) and without (No density delta) density change term and by using smaller spatial step (Small step No density delta).

Appendix C Estimate of some physical parameters for *in vivo* systems

The viscosity in human tissues

We used a Newtonian fluid model in this work. Many biological fluids and tissues exhibit non-Newtonian behavior and the viscosity is a function of the shear strain rate. We choose a viscosity range of 0.001 N.s/m^2 to 0.5 N.s/m^2. This range covers the viscosities of human body fluids [127]. Human soft tissues typically are modeled as a viscoelastic solid. Their mechanical properties show a strong dependent on the stain rate. Therefore the effective viscosity varies as a function of frequency. At low strain rate, the viscosity of soft tissues is reported to be around 10^4 N.s/m^2. As the strain rate increases, the viscosity reduces significantly due to shear thinning [128][129][130][131][132][133]. For example, a viscosity value 15 N.s/m^2 sometimes is used in literature for soft tissue when frequencies are less than 100 kHz [134]. At our case, the driving frequency is 1 MHz and during the inertial collapse, the strain rate could be even higher. We estimate the viscosity could be small and covered by the viscosity range we chose. Figure C1 shows the viscosity of pig kidney. The original data are only given for low frequency (<=15Hz) [130]. We used 15 N.s/m^2 at 100 Hz and then extrapolated the viscosity to 1 MHz. We can see at the range of 1 MHz, the viscosity is around 0.02 N.s/m^2. As far as the viscosity in our tissue phantom, since the attenuation in the graphite-free phantom is very low, the viscosity should be small. Our ultimate justification for this estimate is the fact that we observed inertial cavitation, thus we can set a rough upper bound for the viscosity of 0.1 N.s/m^2 in our tissue phantom.

The dissolved gas concentration in human body

The air we breathe contain 21% O_2, 78% N_2, and 1% Argon and other components. Those gases come into blood through a diffusion process in our lungs. The blood exiting the lung is saturated with all the components of air, which mostly are N_2 and O_2. N_2 is biologically inert under normal conditions and does not undergo any net exchange across the lung wall. The existence of O_2 in blood has two forms, 98.5% of the O_2 is bound to hemoglobin and only 1.5% of O_2 is physically dissolved in the blood [135][136]. The 1.5% O_2 physically dissolved in the blood is the saturation value for the O_2. Therefore, the O_2 is actually over-saturated in the arterial blood. Metabolic reactions occurring within cells are constantly consuming oxygen and producing carbon dioxide. Therefore, there is a net diffusion of oxygen from blood into cells and net diffusion of carbon dioxide from cells into blood. When CO_2 is carried back to the lung by blood, 10% of it is physically dissolved since CO_2 is about 20 times more soluble than O_2, and the other 90% react with hemoglobin or be converted to ions. In general, blood is saturated with gases, and in tissue, the dissolved gas concentration may decrease due to the consuming of the O_2 and the change of the internal pressure [137]. But since the N_2 should be saturated everywhere, we estimate the dissolved gas concentration in human tissue is likely to be in the range of 70%-100% saturated with air.
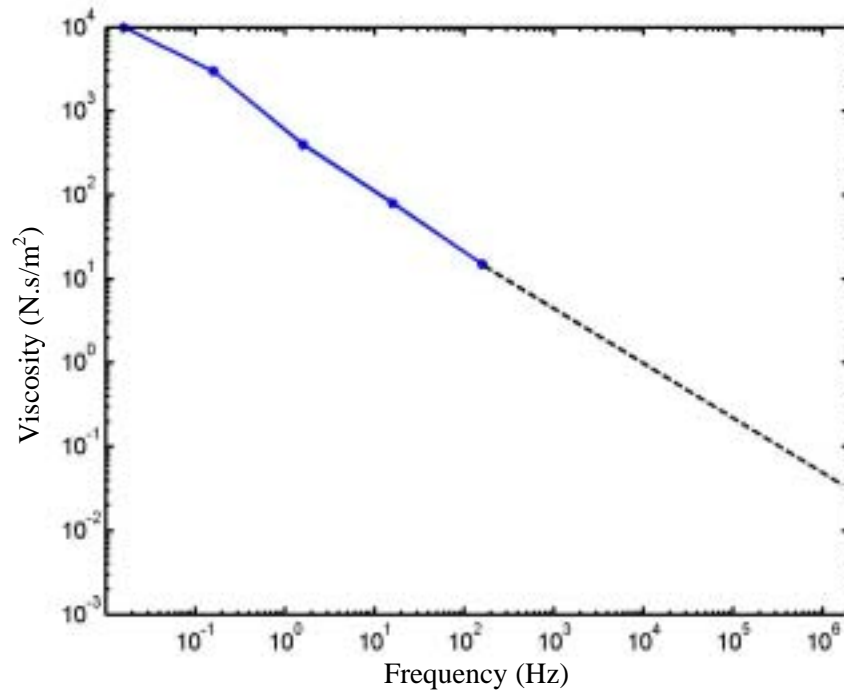
Figure C1 Viscosity of pig kidney from reference [130]. Solid line represents real data and dash line represents the extrapolated result.

Bibliography

[1] Pierce AD. *Acoustics-An introduction to its physical principles and applications*. 1994, *Acoustical Society of America*.

[2] Deng CX and Lizzi FL. A review of physical phenomena associated with ultrasonic contrast agents and illustrative clinical applications. *Ultrasound in Medicine and Biology*, 2002, 28, 277-286.

[3] Darkazanli A, Hynynen K, Unger E, and Schenck JF. On-line monitoring of ultrasound surgery with MRI. *Journal of Magnetic Resonance Imaging*, 1993, 3, 509-514.

[4] Damianou CA, Hynynen K, and Fan X. Evaluation of accuracy of a theoretical model for predicting the necrosed tissue volume during focused ultrasound surgery. *IEEE Transactions on Ultrasonics, Ferroelectrics, and Frequency Control*, 1995, 42, 182-187.

[5] Hynynen K, Darkazanli A, Unger E, and Schenck JF. MRI-guided noninvasive ultrasound surgery. *Medical Physics*, 1993, 20, 107-115.

[6] ter Haar GR. Ultrasound focal beam surgery. *Ultrasound in Medicine and Biology*. 1995, 21, 1089-1100.

[7] Pond JB. The role of heat in the production of ultrasonic focal lesions. *The Journal of the Acoustical Society of America*, 1970, 47, 1607-1611.

[8] Wu J and Du G. Temperature rise in a tissue-mimicking material generated by unfocused and focused ultrasound transducers. *Ultrasound in Medicine and Biology*, 1992, 18, 495-512.

[9] Curley MG. Soft tissue temperature rise caused by scanned, diagnostic ultrasound. *IEEE Transactions on Ultrasonics, Ferroelectrics, and Frequency Control*, 1993, 40, 59-66.

[10] Lynn JG, Zwemer RL, Chick AJ, and Miller AE. A new method for the generation and use of focused ultrasound in experimental biology. *The Journal of General Physiology*, 1942, 26, 179-193.

[11] Lynn JG and Putnam TJ. Histology of cerebral lesions produced by focused ultrasound. *The American Journal of Pathology*, 1944, 20, 637-643.

[12] Pennes HH. Analysis of tissue and arterial blood temperatures in the resting human forearm. *Journal of Applied Physiology*, 1, 1948, 93-122.

[13] Huang J. Heating in vascular tissue and flow-through tissue phantoms induced by focused ultrasound. *Ph. D dissertation*, Boston University, 2002.

[14]   Apfel RE and Holland CK. Gauging the likelihood of cavitation from short-pulse, low-duty cycle diagnostic ultrasound. *Ultrasound in Medicine and Biology,* 1991, 17, 197-185.

[15]   Leighton TG. *The Acoustic Bubble*, Academic Press, 1994.

[16]   Bacon DR and Carstensen EL. Increased heating by diagnostic ultrasound due to nonlinear propagation. *The Journal of the Acoustical Society of America,* 1990, 80, 26-34.

[17]   Christopher T and Carstensen EL. Finite amplitude distortion and its relationship to linear derating formulae for diagnostic ultrasound system. *Ultrasound in Medicine and Biology,* 1996, 22, 1103-1116.

[18]   Dalecki D, Carstensen EL, and Parker KJ. Absorption of finite amplitude focused ultrasound. *The Journal of the Acoustical Society of America,* 1991, 89, 2435-2447.

[19]   Bush NL, Rivens I, ter Haar GR, and Bamber JC. Acoustic properties of lesions generated with an ultrasound therapy system. *Ultrasound in Medicine and Biology*, 1993, 19, 789-801.

[20]   Chapelon JY, Dupenloup F, Cohen H, and Lenz P. Reduction of cavitation using pseudo-random signals. *IEEE Transactions on Ultrasonics, Ferroelectrics, and Frequency Control*, 1996, 43, 623-625.

[21]   Colemam AJ Choi MJ, and Saunders JE. Detection of acoustic emission from cavitation in tissue during clinical extracorpeal lithotripsy. *Ultrasound in Medicine and Biology*, 1996, 22, 1097

[22]   Fry FJ, Sanghvi NT, Foster RS, Bihrle R, and Hennige C. Ultrasound and microbubbles: their generation, detection and potential utilization in tissue and organ therapy-experimental. *Ultrasound in Medicine and Biology*, 1995, Vol. 21, No. 9, 1227-1237

[23]   Wood RW and Loomis AL. The physical and biological effects of high frequency sound waves of great intensity. *The London, Edinburgh, and Dublin Philosophical Magazine and Journal of Science*, 1927, 4, 417-436.

[24]   Schmitt FO, Johnson CH, and Olson AR. Oxidations promoted by ultrasonic radiation. *Journal of the American Chemical Society*, 1929, 51, 370-375.

[25]   Johnson CH. The lethal effects of ultrasonic radiation. *The Journal of Physiology*, 1929, 67, 356-359.

[26]   Harvey EN. Biological aspects of ultrasonic waves, a general survey. *The Biological Bulletin*, 1930, 59, 306-325.

[27]   Hueter TF, Ballantine HT, and Cotter WC. Production of lesions in the central nervous system with focused ultrasound: A study of dosage factors. *The Journal of the Acoustical Society of America* 1956, 28, 192-201.

[28]   Fry FJ, Heimburger RF, Gibbons LV, and Eggleton RC. Ultrasound for visualization and modification of brain tissue. *IEEE Transactions on Sonics Ultrasonics*, 1970, SU-17,165-169.

[29]   Fry FJ, Kossoff G, Eggleton RC, and Dunn F. Threshold ultrasound dosages for structural changes in the mammalian brain. *The Journal of the Acoustical Society of America,* 1970, 48, 1413-1417.

[30]   Fry WJ, Wulff VJ Tucher D, and Fry FJ. Physical factors involved in ultrasonically induced changes in living systems: I. Identification of non-temperature effects. *The Journal of the Acoustical Society of America*, 1950, 22, 867-876.

[31]   Fry WJ, Mosberg WH, Barnard WJ, and Fry FJ. Production of focal destructive lesions in the central nervous system with ultrasound. *Journal of Neurosurgery*, 1954, 11, 471-478.

[32]   Fry WJ, Barnard WJ, Fry FJ, Krumins RF, and Brennan JF. Ultrasonic lesions in the mammalian central nervous system. *Science*, 1955, 122, 517-518.

[33]   Lele PP. Effects of ultrasound on solid mammalian tissues and tumors in vivo. *Ultrasound: Medical applications, biological effects and hazard potential*. New York: Plenum, 1987, 275-306.

[34]   Hynynen K. The threshold for thermally significant cavitation in dog's thigh muscle in vivo. *Ultrasound in Medicine and Biology*, 1991, 17, 157-169.

[35]   Clarke RL and ter Haar GR. Temperature rise recorded during lesion formation by high-intensity focused ultrasound. *Ultrasound in Medicine and Biology*, 1997, 23, 299-306.

[36]   Miller DL and Gies RA. The interaction of ultrasonic heating and cavitation in vascular bioeffects on mouse intestine. *Ultrasound in Medicine and Biology*, 1998, 24, 123-128.

[37]   Watkin NA, ter Haar GR, Morris SB, and Woodhouse CR. The urological applications of focused ultrasound surgery. *British Journal of Urology*, 1995, 75(suppl. 1), 1-8.

[38]   Vaezy S, Shi X, Martin RW, Martin RW, Chi E, Nelson PI, Bailey MR, and Crum LA. Real time visualization of focused ultrasound therapy. *Ultrasound in Medicine and Biology*, 2001, 27.

[39]   Vykhodtseva NI, Hynynen K, and Damianou C. Histologic effects of high intensity pulsed ultrasound exposure with subharmonic emission in rabbit brain in vivo. *Ultrasound in Medicine and Biology,* 1995, 21, 969-979.

[40]   Watmough DJ, Lakshmi R, Ghezzi F, Quan KM, Watmough JA, Khizhnyak E, Pashovkin TN, and Sarvazyan AP. The effect of gas bubbles on the production of ultrasound hyperthermia at 0.75MHz: A phantom study. *Ultrasound in Medicine and Biology*, 1993, 19, 231-241.

[41]   Sanghvi NT, Fry FJ, Bihrle R, Forster RS, Phillips MH, Syrus J, Zaitsev AV, and Hennige CW. Noninvasive surgery of prostate tissue by high-intensity focused ultrasound. *IEEE Transactions on Ultrasonics, Ferroelectrics, and Frequency Control*, Symposium 1996, 43, 1099-1109.

[42]   ter Haar GR and Daniels S, Evidence for ultrasonically induced cavitation *in vivo*, *Physics of Medicine and Biology*, 1981, 26, 1145-1149.

[43]   Bailey MR., Couret LN., Spaozhnikov OA, Khokhlova VA., ter Haar G., Vaezy S., Shi X., Martin R., and Crum LA. Use of overpressure to assess the role of bubbles in focused ultrasound lesion shape in vitro. *Ultrasound in Medicine and Biology*, 2001, 27, 695-708.

[44]   Holt RG and Roy RA. Measurements of bubble-enhanced heating from focused, MHz-frequency ultrasound in a tissue-mimicking material. *Ultrasound in Medicine and Biology*, 2001, 27, 1399-1412.

[45]   Hilgenfeldt S, Lohse D, and Zomack M. Sound scattering and localized heat deposition of pulse-driven microbubbles. *The Journal of the Acoustical Society of America*, 2000, 107, 3530-3539.

[46]   Hilgenfeldt S, Lohse D, and Zomack M. Response of bubbles to diagnostic Ultrasound: a unifying theoretical approach. *European Physics Journal B*, 1998, 4, 247-255.

[47]   Chavrier F, Chapelon JY, Gelet A, and Cathignol D. Modeling of high-intensity focued ultrasound-induced lesions in the presence of cavitation bubbles. *The Journal of the Acoustical Society of America*, 2000, 108, 432-440.

[48]   Edson PL. The role of acoustic cavitation in enhanced ultrasound-induced heating in a tissue-mimicking phantom. *Ph.D. dissertation*, Boston University, 2001

[49]   Brayman AA, Azadniv M, Cox C, and Miller MW. Hemolysis of albunex-supplemented, 40% hematocrit human erythrocytes in vitro by 1 MHz pulsed ultrasound: acoustic pressure and pulse length dependence. *Ultrasound in Medicine and Biology*, 1996, 22, 927-938.

[50]   Poliachik SL, Chandler WL, Mourad PD, Bailey MR, Bloch S, Cleveland RO, Kaczkowski P, Keilman G, Porter T, and Crum LA. Effect of high-intensity focused ultrasound on whole blood with and without microbubble contrast agent. *Ultrasound in Medicine and Biology*, 1999, 25, 991-998.

[51]   Miller DL and Gies RA. Enhancement of ultrasonically-induced hemolysis by perfluorocarbon-based compared to air-based echo-contrast agents. *Ultrasound in Medicine and Biology*, 1998, 24, 285-292.

[52]   Miller MW, Everbach EC, Cox C, Knapp RR, Brayman AA, and Sherman TA. A comparison of the hemolytic potential of Optison and Albunex in whole human blood in vitro: acoustic pressure, ultrasound frequency, donor and passive cavitation detection considerations. *Ultrasound in Medicine and Biology*, 2001, 27, 709-721.

[53]   Wu J. Temperature rise generated by ultrasound in the presence of contrast agent. *Ultrasound in Medicine and Biology*, 1998, 24, 267-274.

[54]   Fujishiro S, Mitsumori M, Nishimura Y, Okuno Y, Nagata Y, Hiraoka M, Sano T, Marume T, and Takayam N. Increased heating efficiency of hyperthermia using ultrasound contrast agent: a phantom study. *International Journal of Hyperthermia*, 1998, 14(5), 495-502.

[55]   Vaezy S, Martin R, Schmiedl U, Caps M, Taylor S, Beach K, Carter S, Kaczkowski P, Keilman G, Helton S, Chandler W, Mourad P, Rice M, Roy RA, and Crum LA.

Liver hemostasis using high-intensity focused ultrasound. *Ultrasound in Medicine and Biology,* 1997, 23, 1413-1420.

[56]   Poliachik SL, Chandler WL, Mourad PD, Ollos RJ, and Crum LA. Activation, aggregation and adhesion of platelets exposed to high-intensity focused ultrasound. *Ultrasound in Medicine and Biology*, 2001, 27, 1567-1576.

[57]   Noble ML, Vaezy S, Keshavarzi A, Paun M, Prokop AF, Chi EY, Cornejo C, Sharar SR, Jurkovich GJ, Martin RW, and Crum LA. Spleen hemostasis using high-intensity ultrasound: survival and healing. *Journal of Trauma*, 2002, 53, 1115-1120.

[58]   Lord Rayleigh. On the pressure developed in a liquid during the collapse of a spherical cavity. *Philosophical Magazine*, 1917, 34, 94-98.

[59]   Plesset MS. The dynamics of cavitation bubbles. *Journal of Applied Mechanics*, 1949, 16, 277-282.

[60]   Keller JB and Miksis MJ. Bubble oscillations of large amplitude. *The Journal of the Acoustical Society of America*, 1980, 68, 628-633.

[61]   Prosperetti A and Lezzi A. Bubble dynamics in a compressible liquid. Part 1. First order theory. *Journal of Fluid Mechanics*, 1986, 168, 457-478.

[62]   Plesset MS. On the stability of fluid flows with spherical symmetry. *Journal of Applied Physics,* 1954, 96-98.

[63]   Prosperetti A. Viscous effects on perturbed spherical flows. *Quarterly of Applied Mathematics,* 1977b 34, 339-352.

[64]   Prosperetti A. On the stability of spherically symmetric flows. *Atti Accad. Naz. Lincei, Rend. Cl. Sci. Fis. Mat. Nat.* 62, 1977c, 196-203.

[65]   Hao Y and Prosperetti A. The effect of viscosity on the spherical stability of oscillating gas bubbles. *Physics of Fluids,* 1999, Vol. 11, (6) 1309-1317.

[66]   Hilgenfeldt S, Lohse D, and Brenner MP. Phase diagrams for sonoluminescing bubbles. *Physics of Fluids*, 1996, 8, 2808-2826

[67]   Eller A and Flynn HG. Rectified diffusion during nonlinear pulsations of cavitation bubbles. *The Journal of the Acoustical Society of America*, 37, 1965, 493-503.

[68]   Epstein PS and Plesset MS. On the stability of gas bubbles in liquid-gas solutions. *Journal of Chemical Physics*, 1950, 18, 1505-1509.

[69]   Fyrillas MM and Szeri AJ. Dissolution or growth of soluble spherical oscillating bubbles. *Journal of Fluid Mechanics*, 277, 1994, 381-407.

[70]   Crum LA, and Law W. The relative roles of thermal and nonthermal effects in the use of high intensity focused ultrasound for the treatment of benign prostatic hyperplasia. *Proceedings of the 15th International Congress on Acoustics*, Trondheim, Norway, 1995.

[71]   Flynn HG. *Physics of acoustic cavitation in liquids. In: physical Acoustics*, Vol. 1, Part B (Mason WP, ed.). Academic Press, New York, 1964.

[72] Prosperetti A. Thermal effects and damping mechanisms in the forced radial oscillations of gas bubbles in liquids. *The Journal of the Acoustical Society of America*. 61, 1977a, 17-27.

[73] Prosperetti A. The thermal-behavior of oscillating gas-bubble. *Journal of Fluid Mechanics*, 1991, 222, 587-616.

[74] Allen JS, Roy RA, and Church CC. On the role of shear viscosity in mediating inertial cavitation from short-pulse, megahertz-frequency ultrasound. *IEEE Transactions on Ultrasonics, Ferroelectrics, and Frequency Control,* 44, 743-751, 1997.

[75] Prosperetti A, Crum LA, and Commander KW. Nonlinear bubble dynamics. *The Journal of the Acoustical Society of America*, 1988, 83, 502-514.

[76] Gaitan DF. An experimental investigation of acoustic cavitation in gaseous liquid. *PhD dissertation*, 1990, University of Mississippi.

[77] Gaitan DF, Crum LA, Church CC, and Roy RA. Sonoluminescence and bubble dynamics for a single, stable, cavitation bubble. *The Journal of the Acoustical Society of America*, 1992, 91, 3166-3183.

[78] Prosperetti A and Hao Y. Modeling of spherical gas bubble oscillations and sonoluminescence. *Philosophical Transactions of The Royal Society of London Series A*, 1999, 357, 203-223.

[79] Kamath V and Prosperetti A. Numerical integration methods in gas-bubble dynamics. *The Journal of the Acoustical Society of America*, 1989, 85, 1538-1548.

[80] Isaacson E and Keller HB. *Analysis of numerical methods*. Dover Publications, Inc., 1966, New York.

[81] Eller A and Crum LA. Instability of the motion of a pulsating bubble in a sound field. *The Journal of the Acoustical Society of America*, 1970, 47, 762-767.

[82] Holt RG and Gaitan DF. Observation of stability boundaries in the parameter space of single bubble sonoluminescence. *Physical Review Letter*, 1996, 77 (18) 3791-3794.

[83] Gaitan DF and Holt RG. Experimental observations of bubble response and light intensity near the threshold for single bubble sonoluminescence in an air-water system. *Physical Review E*, 1999, 59, 5495-5502.

[84] Brenner MP, Lohse D, and Dupont TF. Bubble shape oscillations and the onset of sonoluminescence. *Physical Review Letter*, Vol. 75, No. 5, 954-957.

[85] Nayfeh AH and Mook DT. *Nonlinear Oscillations*. Wiley, John & Sons, 1995.

[86] Lauterborn W. Numerical investigation of nonlinear oscillation of gas bubbles in liquids. *The Journal of the Acoustical Society of America*, 1976, 59, 283-293.

[87] Parlitz U, Englisch V, Scheffczyk C, and Lauterborn W. Bifurcation structure of bubble oscillations. *The Journal of the Acoustical Society of America*, 1990, 88, 1061-1077.

[88]   Crum LA. Measurements of the growth of air bubbles by rectified diffusion. *The Journal of the Acoustical Society of America,* 1980, 68, 203-211.

[89]   Kamath V and Prosperetti A. Mass transfer during bubble oscillations. In Frontiers of Nonlinear Acoustics: *Proceedings of the Twelfth International Symposium*, *On Nonlinear Acoustics* (ed. M. F. Hamolton & D. T. Blackstock), 1990, 503-508. Elsevier.

[90]   Eller A. Growth of bubbles by rectified diffusion. *The Journal of the Acoustical Society of America*, 1969, 46, 1246-1250.

[91]   Faraday M. On the forms and states assumed by fluids in contact with vibrating elastic surfaces. *Philosophical Transactions A of The Royal Society*, 1831, 121, 319-340.

[92]   Benjamin TB and Ursell F. The stability of the plane free surface of a liquid in vertical periodic motion. *Proceedings of The Royal Society*, 1954, A225, 505-515.

[93]   Lamb H. *Hydrodynamics*. Dover Publications, Inc., 1945, New York.

[94]   Akhatov I, Gumerov N, Ohl CD, Parlitz U, and Lauterborn W. The role of surface tension in stable single-bubble sonoluminescence. *Physical Review Letter*, 78(2), 1997, 227-230.

[95]   Lauterborn W and Holzfuss J. Acoustic Chaos. *International Journal of Bifurcation and Chaos,* Vol. 1, No. 1, 1991, 13-26.

[96]   Fry WJ and Fry RB. Determination of absolute sound levels and acoustic absorption coefficients by thermocouple probes – theory. *The Journal of the Acoustical Society of America*, 1954, 26, 294-310.

[97]   Fry WJ and Fry RB. Determination of absolute sound levels and acoustic absorption coefficients by thermocouple probes – experiment. *The Journal of the Acoustical Society of America*, 1954, 26, 311-317.

[98]   Lele PP. A simple method for the production of trackless focal lesions with focused ultrasound: Physical factors. *The Journal of Physiology*, 1962, 160, 494-512.

[99]   Parker KJ. The thermal pulse decay technique for measuring ultrasonic absorption coefficients. *The Journal of the Acoustical Society of America*, 1983, 74, 1356-1361.

[100]   Parker KJ. Effects of heat conduction and sample size on ultrasonic absorption measurements. *The Journal of the Acoustical Society of America*, 1985, 77, 719-725.

[101]   Hamilton MF and Morfey CL. Model equations. *Nonlinear Acoustics*, Chapter 3, Hamilton and Blackstock editors, Academic Press, 1998.

[102]   Westervelt PJ. Parametric acoustic array. *The Journal of the Acoustical Society of America*, 1963, 35, 535-537.

[103]   Hallaj IM. Nonlinear acoustics in underwater and biomedical applications: array performance degradation and time reversal invariance. 1999, *PhD dissertation*, University of Washington.

[104]   Beyer RT. The Parameter B/A. *Nonlinear Acoustics*, Chapter 2, Hamilton and Blackstock editors, Academic Press, 1998.

[105] Devin C. Survey of thermal, radiation, and viscous damping of pulsating air bubbles in water. *The Journal of the Acoustical Society of America*, 1959, 31, 1654-1667.

[106] Kamath V, Oguz HN, and Prosperetti A. Bubble oscillations in the nearly adiabatic limit. *The Journal of the Acoustical Society of America*, 1992, 92, 2916-2023.

[107] Kornfeld M and Suvorov L. On the destructive action of cavitation. *Journal of Applied Physics*, 1944, 15 495-506.

[108] Hynynen K and Edwards DK. Temperature measurements during ultrasound hyperthermia. *Medical Physics*, 1989, 16, 618-626.

[109] Hynynen K, Martin CJ, Watmough DJ, and Mallard JR. Errors in temperature measurement by thermocouple probes during ultrasound induced hyperthermia. *The British Journal of Radiology*, 1983, 56, 968.

[110] Wu EX, Goodsitt MM, and Madsen EL. Microscopic mechanism of attenuation of compressional ultrasonic waves in tissue-mimicking phantom materials. *Ultrasonic Imaging*, 1992, 14, 121-133.

[111] Allegra JR and Hawley SA. Attenuation of sound in suspensions and emulsions: Theory and Experiments *The Journal of the Acoustical Society of America*, 1972, 51, 1545-1564.

[112] Roy RA, Madanshetty SI, and Apfel RE. An acoustic backscattering technique for the detection of transient cavitation produced microsecond pulses of ultrasound. *The Journal of the Acoustical Society of America*, 1990, 87, 2451-2458.

[113] Eller A and Flynn HG. Generation of subharmonics of order one-half by bubbles in a sound field. *The Journal of the Acoustical Society of America*, 1969, 46(3), 722-727.

[114] Apfel RE. The role of impurities in cavitation-threshold determination. *The Journal of the Acoustical Society of America*, 1970, 48, 1179-1186.

[115] Young DE. Skins of variable permeability: a stabilization mechanism for gas cavitation nuclei. *The Journal of the Acoustical Society of America*, 1979, 65, 1429-1439.

[116] Young DE. On the evolution, generation, and regeneration of gas cavitation nuclei. *The Journal of the Acoustical Society of America*, 1982, 71, 1473-1481.

[117] Young DE. Gillary EW and Hoffman DC, A microscopic investigation of bubble formation nuclei. *The Journal of the Acoustical Society of America*, 1984, 76, 1511-1521.

[118] Fox FE and Herafeld KF. Gas bubbles with organic skin as cavitation nuclei. *The Journal of the Acoustical Society of America*, 1954, 26, 984-989.

[119] Wood AB. *A Textbook of Sound*. MacMillan, New York, 1st edition, 1930.

[120] Wilson PS. Sound propagation and scattering in bubbly liquids. *PhD dissertation*, Boston University, 2002.

[121] Allen JS and Roy RA. Dynamics of gas bubbles in viscoelastic fluids. I. Linear viscoelasticity. *The Journal of the Acoustical Society of America*, 2000, 107, 3167-3178.

[122] Allen JS and Roy RA. Dynamics of gas bubbles in viscoelastic fluids, II. Nonlinear viscoelasticity. *The Journal of the Acoustical Society of America*, 2000, 108, 1640-1650.

[123] Gilmore FR. *Hydrodynamics Laboratory Report* 26-4, 1952, California Institute of Technology.

[124] Flynn FG. Cavitation dynamics. I. A mathematical formulation. *The Journal of the Acoustical Society of America*, 1975, 57, 1379-1396.

[125] Prosperetti A. Bubble phenomena in sound fields: part one. *Ultrasonics,* 1984, 22, 69-77.

[126] Prosperetti A. Bubble phenomena in sound fields: part two. *Ultrasonics*, 1984, 22, 115-124.

[127] Duck FA. *Physical properties of tis*sue. Academic Press, 1990.

[128] Fung YC. *Biomechanics: Mechanical Properties of Living Tissues*. 2nd ed., Springer-Verlag, 1993

[129] Ragsdale GK, Phelps J, and Luby-Phelps K. Viscoelastic response of fibroblasts to tension transmitted through adherents junctions. *Biophysical Journal*, 1997, 73, 2798-2808.

[130] Nasseri S, Bilston LE, and Phan-Thien N. Viscoelastic properties of pig kidney in shear, experimental results and modeling. *Rheologica Acta*, 2002, 41 180-192.

[131] Hochmuth RM, Ting-Bean HP, Beaty BB, Needham D, and Tran-Son-Tay R. Viscosity of passive human neutrophils undergoing small deformations. *Biophysical Journal*, 1993, 64, 1596-1601.

[132] Donnelly BR and Medige J. Shear properties of human brain tissue. *Journal of Biomechanical, ASME*, 1997, 119, 423-432.

[133] Forgacs G, Foty RA, Shafrir Y, and Steinberg MS. Viscoelastic properties of living embryonic tissues: a quantitative study. *Biophysical Journal*, 1998, 74, 2227-2234.

[134] von Gierke HE. Effects of vibration and shock on people. *Encyclopedia of Acoustics*, Chapter 145, edited by Crocker, 1997, John Wiley & Sons, Inc.

[135] Vander AJ, Sherman JH, and Luciano DS. *Human physiology, the mechanism of body function*. Sixth edition, 1994, McGRAW-HILL, INC.

[136] Guyton AC. *Textbook of medical physiology*. Seventh edition, W. B. Saunders Company, 1986.

[137] Guyton AC, Taylor AE, and Granger HJ. *Circulatory physiology II: Dynamics and Control of the Body Fluid*. W. B. Saunders Company, 1975.

Vita

Xinmai Yang was born in 1974, in Xi'an, Shaanxi province, People's Republic of China, a city which has been the capital of China for over 2000 years in the past. He finished the elementary school in his hometown. The family moved to Shijiazhuang, the capital of Hebei province in August, 1988 when Xinmai Yang was in middle school. He graduated from middle school and high school in Shijiazhuang. In 1993, he came back to his hometown, joining Xi'an Jiaotong University as an undergraduate student. His undergraduate major was Engineering Mechanics (a fancy name for Applied Mechanics). He received his Bachelor's degree in 1997, ranking first in his class, and entered the graduate school in Xi'an Jiaotong University. Under the instruction of Professor Yapeng Shen, he got his Master's degree in Solid Mechanics in 2000. In the same year he came to Boston University to study acoustics, which he found much more interesting than he had thought. After spending the first five months with Professor Robin O Cleveland, he started his research on HIFU under the supervision of Professor R. Glynn Holt and Professor Ronald A Roy. After these busy, but joyful years, he earned his Ph. D degree. Next he will work as a postdoctoral research associate at the National Center for Physical Acoustic in Oxford, MS, and continue the research on HIFU and bubbles.

Permanent Address: 4-3-103 East Campus

Hebei University of Medical Science

Shijiazhuang, Hebei 050031

People's Republic China